Time Resolved Single Molecule Fluorescence Spectroscopy on Surface Tethered and Freely Diffusing Proteins

Inaugural-Dissertation

Zur
Erlangung des Doktorgraes der
Mathematisch-Naturwissenschaftlichen Fakultät
Der Heinrich-Heine-Universität Düsseldorf

Vorgelegt von
Diaa Atta
aus Kairo (Ägypten)

Jülich
November 2011

Gutachter: Prof. Dr. Georg Büldt
Prof. Dr. Jan K.G. Dhont
PD Dr. Jörg Fitter

To the soul of my Mother

To the soul of my Mother of low

To My great Father

To the most beautiful, sincere, and lovely woman over all the mankind my wife

Abbreviations and symbols

3D	Three dimension
Å	Angstrom
AFM	Atomic force microscope
AOTF	Acousto-optic tunable filter
B	Molecular brightness
BLA	α-Amylase from *Bacillus Licheniformis*
CCD	Charge coupled device
CYS	Cysteine
D	Donor molecule
DLS	Dynamic light scattering
DNA	Desoxyribo-Nucleic Acid
DOPE	l-α-di-oleoy lphosphatidylethanolamine
EDTA	Ethylene-Diamine-Tetra-Acetic acid
FCS	Fluorescence correlation spectroscopy
FFT	Fast fourier transform
fl	Femto-liter
FRET	Förster resonance energy transfer
GFP	Green fluorescence protein
I_H	Horizontal polarized beam
I_V	Vertical polarized beam
k_{FRET}	Transfer rate of FRET process
LYS	Lysine
MOPS	3-(N-morpholino) propanesulfonic acid
mPEG	Methoxy poly ethylene glycol
N.A.	Numerical aperture
PEG	Poly ethylene glycol
PEG-SAV	Poly ethylene glycol succinimidyl valerate
PEO	Poly ethylene oxide
PET	Photoinduced electron transfer
PGK	Phosphoglycerate kinase

PPA	Porcine pancreatic alpha-amylase
r_∞	Limited anisotropy
RNA	Ribo-nucleic acid
R_o	Förster radius
S	Singlet state
SERS	Surface enhanced Raman scattering
SPAD	Single-photon avalanche diodes
STM	Scanning tunneling microscope
T	Triplet state
TAKA	α-Amylase from *Aspergillus oryzae*
TCSPC	Time-correlated single-photon counting
TRP	Tryptophan
ZDC	Z-drift compensation
ε	Molar absorption coefficient
η	Medium viscosity
Φ	Quantum yield
τ_c	Rotational correlation time
τ_D	Donor life time/ the pure diffusion time of the diffusing particle
τ_{fluor}	Fluorescence lifetime
τ_s	Singlet state life time
τ_{PET}	The reciprocal of the PET rate
τ_{trp}	Triplet state life time

1 Introduction

Spectroscopic analysis of single molecule is a kind of scientific challenge. There are many spectroscopic efforts to develop techniques for detecting single molecules. Fluorescence is one of these promising techniques in particular in life since, but it is not the only one. There are other strong techniques, like optical tweezers (*4*) , magnetic traps, and single particle tracking, which work with samples in solution (*6,13*). For studies on surfaces there are other techniques, like the atomic force microscopy (AFM). AFM is based on a development of the scanning tunneling microscope (STM) introduced by Gerd Binnig, Calvin Quate and Christopher Gerber in 1986. AFM allows to image not only conducting materials like in STM, but also non conducting materials. Hence AFM gives an opportunity to image biological samples (*11*). Electron microscopy is another powerful tool for imaging, particles and macromolecules at the nanometer scale (*10*). A further technique investigating molecules on the surface with single molecule sensitivity is surface enhanced Raman scattering (SERS), for more detail see references (*6,13*).

The first, successful direct optical detection of a single multiple labeled molecule appeared in the middle of the 1970's by Hirschfeld (*25,26*). In 1989 Mörner and Kador performed single molecule measurements at low temperatures (*28*). Finally, by 1996, the group of Richard A. Keller at the Los Alamos National Laboratory was first able to detect individual rhodamine molecules in a fluid flow (*9*). Later single-molecules, optically detected from single fluorophores at room temperature, became a topic of intensive research work (*22*).

For the single molecule fluorescence techniques the following aspects are of importance:

1. Low background and high signal to noise ratio: Since we look for single emitters, the signal will be weak compared to ensemble measurements, so the background has to be as low as possible.
2. Good fluorophores should have high quantum yields Φ (in between 0.5 and 1) and high absorption coefficients ε ($\sim 10^4$ and 10^5 $cm^{-1}M^{-1}$). Both increase the detection efficiency and thereby increase the signal to noise ratio.

3. The excitation source should be intense, monochromatic, and should deliver a well collimated beam. These properties are typically provided by a laser.
4. High quality of the optical elements are needed, including high numerical aperture objectives, which give small detection volumes, open the measuring angle, and increase the lateral resolution. Also the developments of dichroic mirrors and filter coating reduce the background caused by scattering and by the light from unwanted sources.
5. High sensitive detectors, like single-photon avalanche diodes (SPAD) or charge coupled devices (CCD) cameras, which became available in the last two decades. They provide detecting efficiencies up to 80% or even more, as shown in Figure 1-1.1.

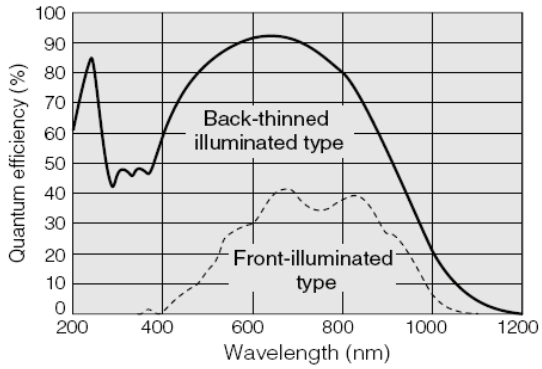

Figure 1-1.1: Quantum efficiency of back-thinned illuminated CCD cameras (1). The quantum efficiency QE is defined as the percentage of the generated electronic charges with respect to the incoming photons (2)(3).

Over the past years laser induced fluorescence detection became a major technique in studying topics in chemistry, in biology, in medicine, and even in material science. In this study the probes, such as biological macromolecules, are either naturally fluorescent (for example green fluorescence protein (GFP)), or are labeled with fluorescent dyes (*17*).

Proteins are the most abundant molecules in the cell and carry out virtually every chemical transformation in the cell. A protein is a kind of natural polymer which is built up from a sequence of 20 different amino acids. These amino acids are linked together to form a polypeptide chain, the sequence of this chain is called the primary structure of a protein. The polypeptide chain is forming loops, helices and/or beta sheets, which are called secondary structure elements. Helices and beta sheets form

domains which finally build up the tertiary structure. A final protein complex may consist of several polypeptide chains, which is called quaternary structure. This tertiary or quaternary structure gives the protein its three dimensional structure and forms functional regions or active sites. Functional regions or active sites give the protein its functional properties and characteristics (*5*).

Fluorescent dyes which are attached to the protein of interest can offer the possibility to study some of these properties. In addition to the detection of the location of fluorescent molecules at a given position (imaging), one can also use the fluorescence detection techniques to obtain the following information about the specimen:

1. A time trace of intensity. One can use time traces to study the blinking or bleaching of an immobilized fluorophore which provides in some cases a good characterization of the fluorophore (*15,20*).
2. Fluorescence correlation spectroscopy (FCS) provides valuable information about the molecule diffusion. Hence one can calculate from the diffusion the hydrodynamic radius of the molecule, which gives information about the spatial extension of the molecule. Also it can give information about molecule binding events which eventually takes place during the molecule diffusion (*21*).
3. Förster Resonance Energy Transfer (FRET) provides information on the proximity of specific labeled sites in the order of a few nanometers apart. FRET gives information about the protein structure and conformations (*7,12,24*). Fluorescence Photoinduced Electron Transfer (PET) can also be measured with diffusing or with tethered molecules (*19,23,29*). PET gives invaluable information about structural conformations of the investigated molecule. Both, FRET and PET, are a kind of quenching of the fluorophore transferring the energy to another molecule. While FRET is dipole-dipole interaction it requires two fluorophores separated by a distance in the order of the Förster radius of the FRET pair, typically 20 to 70 Å. In contrast to FRET, PET is caused by collisional interactions. In PET due to this collision an electron is transferred from the acceptor to the donor (more details in Section 2-4). So, PET is typically detecting short distances while FRET is sensitive for longer distances.

4. The fluorophore is a planar structure which is oriented in three dimension space. The orientation of the fluorophore can provide interesting information about the molecule to which the fluorophore is attached. In this respect anisotropy measurements and defocused wide-field imaging (*27*) are the methods of choice to obtain information about the orientation of the fluorophore. Employing anisotropy decay measurements one can detect the rotational motion of the fluorophore which occur in times shorter than the fluorophore life time (*8,14*). In addition more common steady state anisotropy measurements give valuable information about the rotational freedom of fluorophores attached to biomolecules (*16*).

Single molecule measurements give unequaled information about the heterogeneity of an ensemble of molecules. They provide a complete distribution of observables and allows us to discriminate between static and dynamic heterogeneity of properties of molecules (*18*). This detection technique makes the undetectable, rare, and hidden events in the ensemble accessible. An example is given by the protein folding problem. In spite of the fact that protein folding studies began early in the middle of the last century, the tools which analyze the protein folding at the single molecule level have been recently developed.

The motivation of this work is to study protein folding/unfolding transitions and protein synthesis, using single molecule fluorescence techniques, in particular by using wide field microscopy and fluorescence correlation spectroscopy.

This thesis is organized according to the following scheme:

After this introduction (Chapter 1) it is Chapter 2 which is describing the methods and materials which were used during this work. In this chapter fluorescence phenomena and some related basic physical principles are discussed. The optical setups will be introduced to the reader, namely a detailed description of the wide-field microscope and the confocal microscope. Furthermore, the fluorescence techniques we applied during this work will be explained in more detail (FCS, PET and anisotropy measurements). Finally, I will describe the sample preparations.

Chapter 3 is presenting the obtained results and a discussion of our attempts to observe the proteins as single molecules encapsulated in surface tethered polymeric nanocontainer and to monitor protein synthesis of the green fluorescence protein (GFP).

Also in this chapter I will present results of our attempts to study dynamics and structural conformations of α-amylases and Phosphoglycerate kinase (PGK) using the FCS technique.

In Chapter 4 the obtained results are reviewed in a final conclusion and an outlook on upcoming studies are outlined briefly.

References

1. http://jp.hamamatsu.com/resources/products/sys/pdf/eng/e_dctn1.pdf
2. http://www.jatobservatory.org/CCDPrimer.pdf
3. http://jp.hamamatsu.com/resources/products/sys/pdf/eng/e_dctn1.pdf
4. A.Ashkin (1970) Acceleration and Trapping of Particles by Radiation Pressure, *Phys. Rev. Lett. 24*, 156-159.
5. Carl Branden and John Tooze (1991) *Introduction to Protein Structure* Garland Puplishing,Inc. New York and London.
6. Ch.Zander, J.Enderlein, and R.A.Keller (2002) *Single Molecule Detection in Solution Methods and Applications*.
7. Deniz, A. A., Laurence, T. A., Beligere, G. S., Dahan, M., Martin, A. B., Chemla, D. S., Dawson, P. E., Schultz, P. G., and Weiss, S. (2000) Single-Molecule Protein Folding: Diffusion Fluorescence Resonance Energy Transfer Studies of the Denaturation of Chymotrypsin Inhibitor 2, *Proceedings of the National Academy of Sciences of the United States of America 97*, 5179-5184.
8. E M Phizicky and S Fields. Protein-Protein Interactions: Methods for Detection and Analysis. Microbiol Rev. 59, 94-123. 1995.
9. E.Brooks Shera, Newton K.Seitzinger, Lloyd M.Davis, Richard A.Keller, and Steven A.Soper (1990) Detection of Single Fluorescent Molecules , *Chemical Physics Letters 174*, 553-557.
10. Florian Banhart (2011) in *In-situ Electron Microscopy at High Resolution* pp 1-14, World Scientific, Singapore.
11. Franz J.Giessibl (2003) Advances in Atomic Force Microscopy, *Reviews of Modern Physiscs 75*, 949-983.
12. G.F.Schröder and H.Grubmüller. FRET: Biomolecular Structure Model Building from Multiple FRET Experiments. Computer Physics Communications 158, 150-157. 2004.
13. Ha, T. and Selvin, P. R. (2008) *Single-Molecule Techniques* Cold Spring Harbor Laboratory Press, New York.
14. J.Schafer, A.Volkmer, C.Subramaniam, G.Striker, and C.A.M.Seidel (1999) Identification of Single Molecule in Aqueous Solution by Time Resolved Fluorescence Anisotropy, *Journal of Physical Chemistry A 103*, 331-336.

15. Katranidis, A., Atta, D., Schlesinger, R., Nierhaus, K. H., Choli-Papadopoulou, T., Gregor, I., Gerrits, M., Buldt, G., and Fitter, J. (2009) Fast Biosynthesis of GFP Molecules: A Single-Molecule Fluorescence Study, *Angew. Chem. Int. Ed Engl. 48*, 1758-1761.

16. Lakowicz, J. R. (1999) *Principles of Fluorescence Spectroscopy* Kluwer Academic / Plenum Press, New York.

17. M Eigen and R Rigler. Sorting Single Molecules: Applications to Diagnostics and Evolutionary Biotechnology. PNAS 91, 5740-5747. 1994.

18. Michalet, X., Weiss, S., and Jäger, M. (2006) Single-Molecule Fluorescence Studies of Protein Folding and Conformational Dynamics, *Chem. Rev. 106*, 1785-1813.

19. Piestert, O., Barsch, H., Buschmann, V., Heinlein, T., Knemeyer, J. P., Weston, K. D., and Sauer, M. (2003) A Single-Molecule Sensitive DNA Hairpin System Based on Intramolecular Electron Transfer, *Nano Letters 3*, 979-982.

20. Rasnik, I., McKinney, S. A., and Ha, T. (2006) Nonblinking and long-lasting single-molecule fluorescence imaging, *Nat Meth 3*, 891-893.

21. Rigler, R., Pramanik, A., Jonasson, P., Kratz, G., Jansson, O. T., Nygren, P. A., Stahl, S., Ekberg, K., Johansson, B. L., Uhlen, S., Uhlen, M., Jornvall, H., and Wahren, J. (1999) Specific Binding of Proinsulin C-peptide to Human Cell Membranes, *Proceedings of the National Academy of Sciences of the United States of America 96*, 13318-13323.

22. S.Weiss. (1999) Fluorescence Spectroscopy of Single Biomolecules. *Science* 283, 1676-1683.

23. Sauer, M., Drexhage, K. H., Lieberwirth, U., M_ller, R., Nord, S., and Zander, C. (1998) Dynamics of the Electron Transfer Reaction Between an Oxazine Dye and DNA Oligonucleotides Monitored on the Single-Molecule Level, *Chemical Physics Letters 284*, 153-163.

24. Schuler, B., Lipman, E. A., and Eaton, W. A. (2002) Probing the Free-Energy Surface for Protein Folding with Single-Molecule Fluorescence Spectroscopy, *Nature 419*, 743-747.

25. T.Hirschfeld (1976) Optical Microscopic Observation of Single Small Molecules, *Appl. Opt. 15*, 2965-2966.

26. T.Hirschfeld (1976) Quantum Efficiency Independence of the Time Integrated Emission from a Fluorescent Molecule, *Appl. Opt. 15*, 3135-3139.

27. Uji-i, H., Melnikov, S. M., Deres, A., Bergamini, G., De Schryver, F., Herrmann, A., Müllen, K., Enderlein, J., and Hofkens, J. (2006) Visualizing Spatial and Temporal Heterogeneity of Single Molecule Rotational Diffusion in a Glassy Polymer by Defocused Wide-Field Imaging, *Polymer 47*, 2511-2518.

28. W.E.Moerner and L.Kador. Optical Detection and Spectroscopy of Single Molecules in a Solid. Physical Review Letters 62, 2535-2538. 1989.

29. Ward, M. D. (1997) Photo-Induced Electron and Energy Transfer in Non-Covalently Bonded Supramolecular Assemblies, *Chem. Soc. Rev. 26*, 365-375.

2 Methods and materials

2-1 Fluorescence

Through the last three decades there has been a noticeable increase in the use of fluorescence techniques in biological and chemical research (more than 440,000 publications (*8*)). Fluorescence spectroscopy and time-resolved fluorescence techniques are considered to be primarily research tools in biochemistry and biophysics (*3*). When a sample absorbs and subsequently re-radiates light the process is described as photoluminescence. If the emission of light takes place within a time course between a few milliseconds and seconds after the excitation, the phenomenon is called phosphorescence. Fluorescence, on the other hand, describes light emission that takes place very fast after the excitation process. The time interval between the absorption of the excitation light and the emission of the re-radiated light in fluorescence is usually in order of few nanoseconds.

Some of the first scientific reports about photoluminescence appeared in the middle of the 19th century. In 1845 Sir J.F.W. Herschel (*12*) reports on an experiment he did twenty years earlier, in which he observed that an almost colorless solution of quinine in water emitted a blue color under certain conditions.

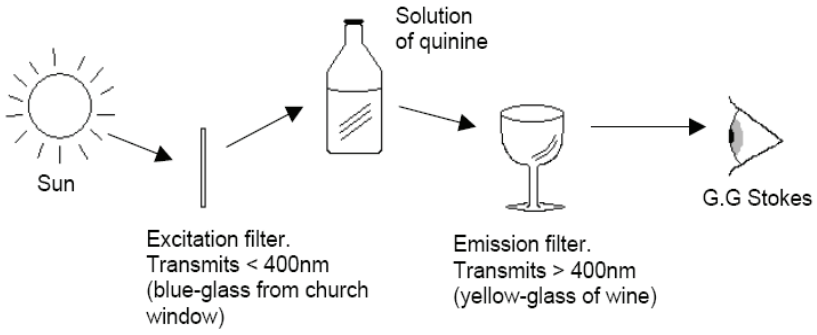

Figure 2-1.1: Experimental set-up used by G.G. Stokes (6).

In a paper that appeared in 1852 Sir G.G. Stokes studied the same compound. He found that the emitted light has a longer wavelength than the absorbed light (the experiment is shown in Figure 2-1.1), which was called later the Stokes' shift. Jabłoński and others developed a modern theoretical understanding of Stokes observation 70 years later. In the 1920s and 1930s Jabłoński investigated polarized light and fluorescence. He

was able to show that the orientation of the transition dipole moments in absorption and in emission are not the same (*3*). Thus the foundation for the concept of anisotropy was established. For that and other accomplishments Jabłoński has been referred to as the father of fluorescence. Jabłoński's work has had a major impact on the theoretical understanding of photophysics.

2-1.1 Basic concepts

a) Excited electronic states

Each electron has a unique set of quantum numbers (Pauli´s "exclusion principle"): *n* (*1s, 3p*...) the principal quantum number, *l* the angular momentum quantum number, *s* the total spin quantum number and *m* the magnetic quantum number. Any two electrons in the same orbital having the same quantum numbers (*n, l, and m*) must have different spins

$$s = + \tfrac{1}{2} \text{ or } -\tfrac{1}{2}$$

So the total spin will be:

$$S = \sum_i s_i \qquad \text{2-1.1}$$

Multiplicity is the quantification of the amount of unpaired electron spins. It is a result of Hund's rule, which favors the single filling of degenerate (same energy) orbitals. The result is the filling of multiple orbitals with electrons or multiplicity. Multiplicity is calculated with the equation: $2\,S + 1$. So the spin multiplicity can be either 0*, 1, 2, etc.* In case of $S = 0$ the multiplicity will be *1*, so this electronic state will be called singlet and denoted by *S.* In case of $S=1/2$ the multiplicity will be *2* and the electronic state will be called doublet state and denoted by *D*. In case of $S=1$ the multiplicity will be *3* and the electronic state will called triplet state and denoted by *T*, and so on (*14*).

b) Absorption and emission

The interaction between an electromagnetic (EM) wave and matter is the basis of the subject of spectroscopy. The EM wave interaction with matter is based on resonant coupling of an incoming EM wave, producing oscillations in the target molecule. According to the nature of the target system and the energy of the incident EM wave, we can obtain excitation of the electronic, the vibrational, or of the rotational states of

the coupled system. The amount of energy required to move an electron, from one state to another is depending on the frequency condition (introduced by Nils Bohr), which relates the EM wave frequency υ to the transition energy ΔE according to the following relation (*15*):

$$\Delta E = E_1 - E_o = h\,\upsilon \qquad 2\text{-}1.2$$

Here h is Planck's constant. If the resonance condition is satisfied, the energy of the incoming EM wave is sufficient to convert the molecule from the lower energy level E_o to a higher energy level E_1. Then after some time (called the life time of the excited state), the molecule emits a photon with a wave length shifted to the red direction on the solar spectrum. This shift is called Stokes' shift, as shown in Figure 2-1.2.

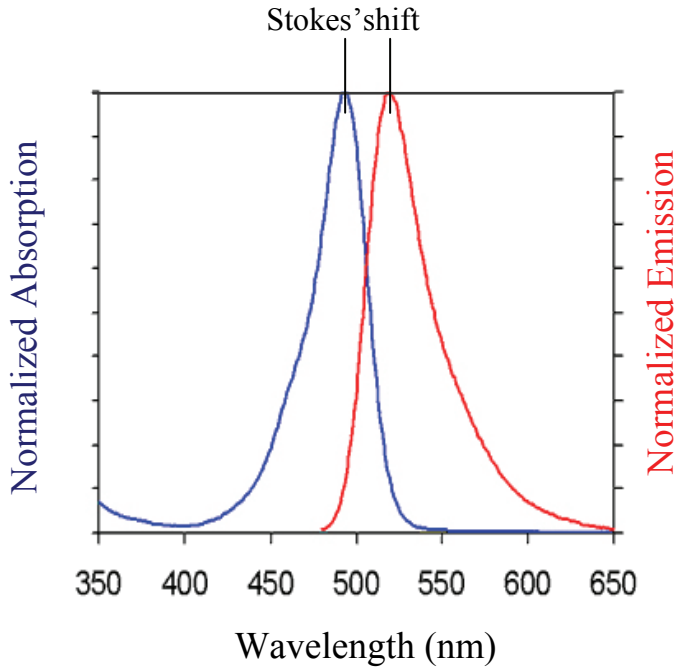

Figure 2-1.2: Absorption-emission spectra of a fluorescent dye called Alexa488.

One can explain the Stokes' shift in more detail as shown in Figure 2-1.3. As we see in this figure, when the electron absorbs the incident wave, it will be transferred from the singlet ground state to the first excited state. From quantum physics we know that the state is not characterized by "a sharp line", but any electronic level is built up from sublevels, called the vibrational levels, furthermore any vibrational level is built up from sublevels called rotational levels, and finally any

rotational level is built up from two spin levels (orbitals). In most cases the excited electron will populate one of these vibrational states. The transition from a particular vibrational state to the "head" of the first excited singlet (S_1) state is fast and radiationless (vibrational and rotational levels). This relaxation dissipates energy in the infrared regime, as shown in Figure 2-1.3 and Figure 2-1.4. Hence the wavelength of the emitted fluorescence photons will be longer, as compared with the absorbed one. It will be shifted to the red direction on the solar spectrum.

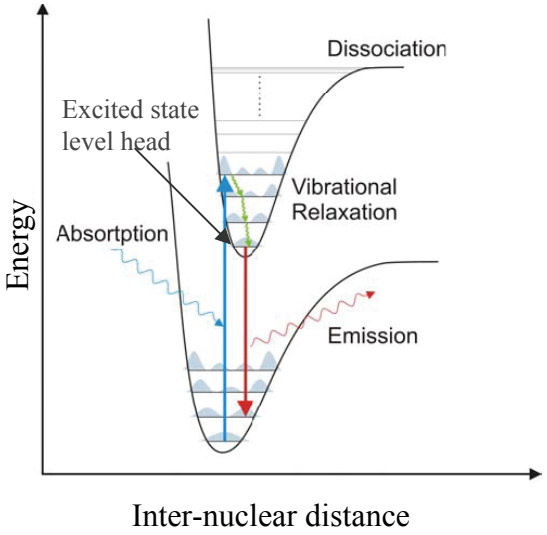

Figure 2-1.3: Frank-Condon principle. Excitation of electronic transitions is fast with respect to nuclei movement, which leads to horizontal transitions into excited vibrational states (7).

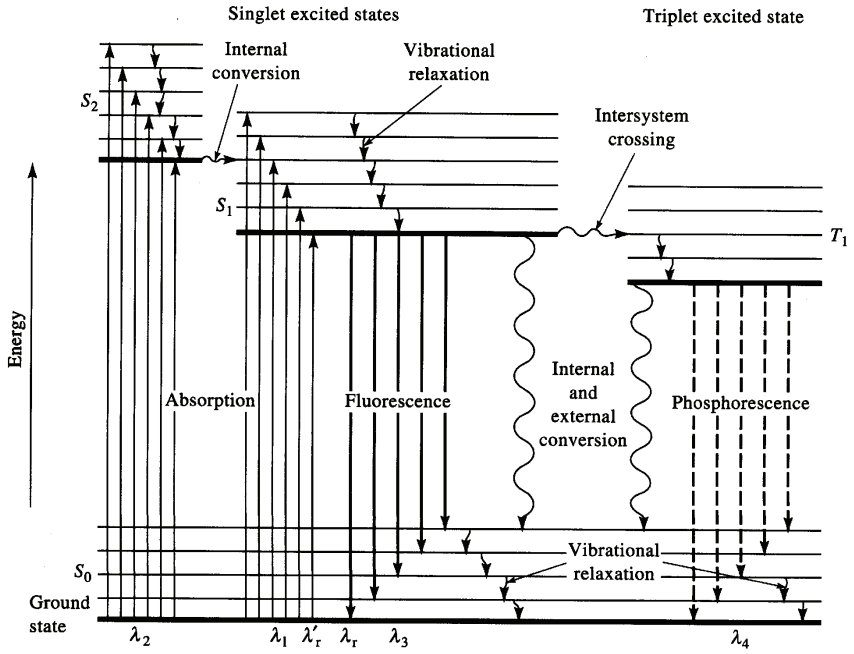

Figure 2-1.4: Jabłoński diagram.

The transition from the ground to the excited state occurs in about a few femtoseconds. This time is too short for significant displacements of the nuclei. This principle was stated semi classically by Franck-Condon in end of 1920's. According to the spin selection rules the transition will be allowed only if ΔS=0 (*16*).

Transition	Description	Rate	Decay life time (s)
$S_o \rightarrow S_1 ... S_n$	Absorption (Excitation)	k_{exc}	10^{-15}
$S_n \rightarrow S_1$	Internal Conversion	K_{ic}	10^{-14}-10^{-10}
$S_1 \rightarrow S_1$	Vibrational Relaxation	K_{vr}	10^{-12}-10^{-10}
$S_1 \rightarrow S_o$	Fluorescence	K_f	10^{-9}-10^{-7}
$S_1 \rightarrow T_1$	Intersystem Crossing	K_{isc}	10^{-10}-10^{-8}
$S_1 \rightarrow S_o$	Non-radiative Relaxation or Quenching	k_{nr}, k_q	10^{-7}-10^{-6}
$T_1 \rightarrow S_o$	Phosphorescence	k_P	10^{-3}-10^{2}
$T_1 \rightarrow S_o$	Non-radiative Relaxation or Quenching	k_{nr}, k_T	10^{-3}-10^{2}

Table 2-1.1: Overview of timescale ranges of all transitions of the first excited singlet state (5).

So, it is improbable that a transition takes place from a singlet state to a triplet state. However, in the fluorescent molecule it could be that intersystem crossing takes place, and phosphorescence happens. According to the Jabłoński diagram there are other deactivation pathways for excited electrons. Some of these pathways take place according to intra-molecular processes like (see Figure 2-1.4):

- ***Internal Conversion***: radiationless transition to lower states when a vibrational energy level matches.
- ***Intersystem Crossing***: transition with a spin change (e.g. $S_i \longrightarrow T_i$).
- ***Fluorescence***: emission not involving a spin change (e.g. $S_i \longrightarrow S_o$), often efficient.
- ***Phosphorescence***: emission involving a spin change ($T_i \longrightarrow S_o$), often improbable, long-lived. Another reason for the deactivation are inter-molecular processes like:
- ***External Conversion***: radiationless transition (*quenching*) to lower state by collisional deactivation

• ***FRET***: radiationless transition to a lower state according to the transfer of the donor energy to another fluorophore (acceptor) in the vicinity (more detail will be discussed in Section 2-1.1d).

• ***PET***: radiationless transition to a lower state according to collisions of the excited fluorophore with another fluorophore (more detail in Section 2-4).

An overview of timescales of all transitions mentioned in the Jabłoński diagram is given in Table 2-1.1

c) Fluorescence lifetime and quantum yield

The molar absorption coefficient ε **(**in biochemical studies given in $M^{-1}cm^{-1}$) quantifies "how strongly" a molecule in solution absorbs light at a given wavelength. Besides the molar absorption coefficient and the fluorophor stability (essentially the maximal number of excitation-emission cycles before the flourophor is photo-destructed) both, the fluorescence lifetime (τ_{fluor}) and the quantum yield (Φ_{fluor}), may affect the fluorophore brightness (emitted photons per molecule per time interval). These parameters depend strongly on the chemical structure and on the environment of a fluorescent molecule. The fluorescence quantum yield is defined by the following equation:

$$\Phi_{fluor} = \frac{number\ \ of\ \ photons\ \ emmitted}{number\ \ of\ \ photons\ \ absorbed} \qquad \left(0 \le \Phi_{fluor} \le 1\right)$$

$$\Phi_{fluor} = \frac{k_{fluor}}{k_{fluor} + k_{nonflou}} \qquad 2\text{-}1.3$$

Here k_{fluor} is the rate constant of fluorescence and $k_{nonfluor}$ is the rate constant of non-fluorescent processes. The fluorescence lifetime τ_{fluor}, refers to the average time that the molecule stays in its excited state before emitting a photon:

$$\tau_{fluor} = \frac{1}{k_{fluor} + k_{nonflou}} \qquad 2\text{-}1.4$$

d) Fluorescence quenching

As shown before in Figure 2-1.4 in the Jabłoński diagram, it could be that intersystem crossing takes place and that the excited electron transfers from a singlet excited state to a triplet state. All triplet states have longer life times than the singlet states. This means

that triplet states work as traps keeping electrons in the excited states for longer time (see Table 2-1.1). A subsequent decay from T_1 to S_o by sending out a photon is called Phosphorescence. A radiationless decay from excited states can take place in the presence of heavy atoms or paramagnetic molecules, due to intersystem crossing enhanced by spin-orbit coupling (*3,17-19*). The latter case can be called quenching. As consequence quenching may affect the excited state lifetime and the fluorescence quantum yield (*20*). This means quenching is always related to a reduction of the fluorescence intensity. There are other inter-molecular processes which lead to an intensity reduction. For example Förster Resonance Energy transfer (FRET) where the transfer rate is given by (*21,22*):

$$k_{FRET} = \frac{1}{\tau_D}\left(\frac{R_o}{r}\right)^6 \qquad 2\text{-}1.5$$

Here r is the distance between the donor (quenched fluorophore) and the acceptor (the quencher molecule) (*3*). τ_D is the fluorescence life time of the donor molecule in absence of the acceptor. R_o is the Förster radius (in Å) and which can be calculated from the spectral properties of the donor and the acceptor by (*23*):

$$R_o = [8.8\times10^{23}\cdot\kappa^2\cdot\Phi_D\cdot J(\lambda)\cdot n^{-4}]^{\frac{1}{6}} \qquad 2\text{-}1.6$$

In this equation κ^2 is the dipole orientation factor, Φ_D is fluorescence quantum yield of the donor in the absence of the acceptor, n is the refractive index of the medium, and $J(\lambda)$ (in $M^{-1}cm^3$) is the spectral overlap integral, as shown in Figure 2-1.5.

Another kind of quenching is given by a collisional process of a quencher with the fluorophore, which is called collisional quenching. This collision can facilitate the non-radiative transition to the ground state of the excited fluorophore. In this case the intensity reduction is given by the Stern-Volmer equation:

$$F = \frac{F_o}{1 + k_{sv}[Q]} \qquad 2\text{-}1.7$$

In this equation F_o is the intensity without collisions, F is the reduced intensity, k_{SV} is the Stern-Volmer quenching constant, and $[Q]$ is the quencher concentration.

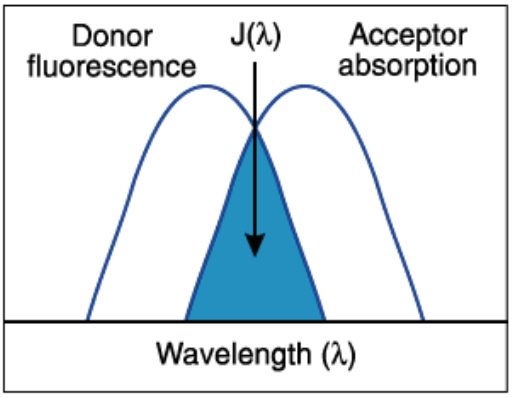

Figure 2-1.5: Schematic representation of the spectral overlap between the donor fluorescence and the acceptor absorption (2)

If this kind of quenching leads to a non-fluorescent complex with a lifetime longer than the fluorescence lifetime, this process is called static quenching. The intensity reduction can be calculated as:

$$F = \frac{F_o}{1 + k_a[Q]} \qquad 2\text{-}1.8$$

Here F_o is the fluorescence intensity before the complex formation, F is the reduced intensity, k_a is the association constant of the complex, and *[Q]* is the quencher concentration. If the lifetime of the fluorophore-quencher complex is shorter than the fluorescent lifetime, this is called dynamic quenching. Dynamic quenching takes place when a collision happens between the excited fluorophore, and another molecule (*e.g.*, O_2). Since dynamic quenching is typically a fast process that depopulates the excited state, the fluorescence lifetime will be affected by this kind of quenching. The fluorescence lifetimes in the presence of the quencher (τ) is given by (*3*)

$$\tau = \left(\tau_o^{-1} + k_q[Q]\right)^{-1} \qquad 2\text{-}1.9$$

Here τ_o^{-1} is the decay rate in the absence of the quencher and k_q is the bimolecular quenching constant. Then one can rewrite Equation 2-1.9 as the following

$$\tau = \frac{\tau_o}{1 + k_q \tau_o [Q]} \qquad 2\text{-}1.10$$

Equation 2-1.7, 2-1.10, and the relation $k_{sv} = \tau_o k_q$, illustrate an important characteristic of dynamic quenching: an equivalent decrease in fluorescence intensity and lifetime (*24*).

$$\frac{F_o}{F} = \frac{\tau_o}{\tau} \qquad 2\text{-}1.11$$

In cases where the association and the dissociation rates of the complex are smaller than the fluorescence life time, one can obtain the life time changes by measuring respective intensities. In this particular case the previous equation is a good test to check whether quenching is static or dynamic.

2-2 High resolution fluorescence microscopy

Fluorescence microscopy has numerous clear advantages for the investigation of the biological samples. These advantages are valuable in particular for high sensitivity detection which enables ones to reach even single molecule level. In this respect the past decade experienced tremendous progress in the field of high resolution optical microscopy applications. On the other hand the vast improvement in fluorescent dyes accelerates progress in the field.

Spectroscopy pioneers suffered from various problems, like image blurring and optical aberration. In 1824 the aberration problem was simultaneously solved in England, by Joseph Jackson Lister and in Italy by Giovanni Battista Amici. They introduce independently achromatic objectives (*25,26*) and they were the first who stated the importance of the immersing medium. In addition, they also improved the numerical apertures to about 0.65 for dry objectives (air immersed objectives) up to 1.25 for the homogenous immersion objectives (*27*). In 1886 Ernst Abbe and Carl Zeiss in co-operation with the chemist Otto Schott produced apo-chromatic objectives (*28*). These advanced objectives provided images with reduced spherical aberration, free of color distortions (chromatic aberration), and with high numerical apertures (*29-31*). The illumination techniques gave also rise to serious problems. In the past microscopists were using the critical illumination technique. In critical illumination the major limitation is that the image of the light source falls in the same plane as the image of the specimen. This means that over the sample image there is also the image from the illumination source (the filament, the dust or fingerprints). Critical illumination

therefore gives a heterogeneous sample illumination. Also it is undesirable as it can introduce artifacts, such as glare shadowing in the image. Various methods can be used to diffuse the filament image like a glass diffuser between the source and the sample. These methods are helpful, to some extent to reduce the heterogeneity of the illumination. However, they all reduce the intensity of illumination and alter the range of wavelengths of light which reach the sample. Later efforts were exerted on the illumination method by August Köhler in 1893. The Köhler illumination is still applied in the recent optical microscopes. This method gives the opportunity to take the full advantage of the resolving power described by Abbe. As shown in Figure 2-2.1 the main idea of Köhler illumination depends on producing what is called conjugate planes, in the image forming pathway or in the sample illumination pathway (*32*). The illumination or the image forming pathway optical setup produces a focused image of the lamp filament at these planes.

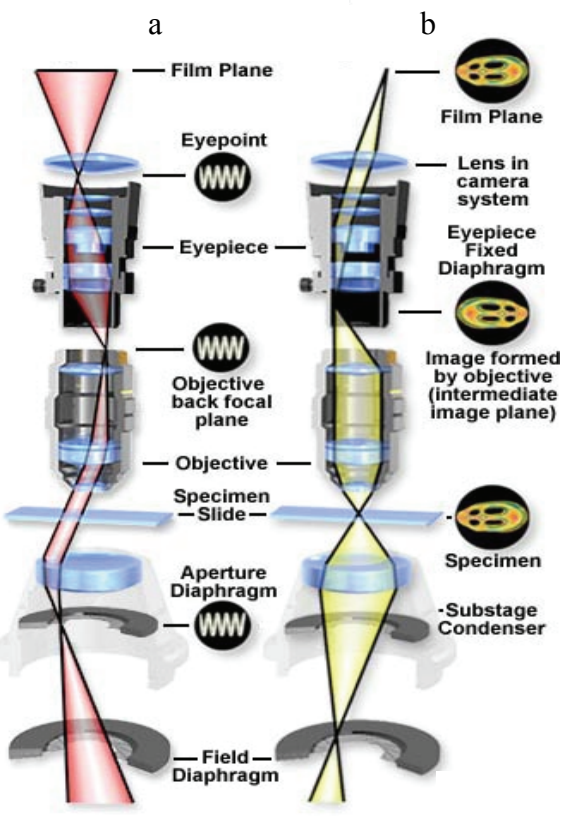

Figure 2-2.1: Köhler illumination in both pathways a) sample illumination and b) image forming (1).

In both light pathways, we have four separate planes in every pathway, which together create a set of conjugate planes. In the illumination pathway the set of conjugate planes consists of the lamp filament, the condenser aperture diaphragm, the rear focal plane of the objective, and the eyepoint of the eyepiece. The eyepoint is located directly above the top lens of the eyepiece, at the point where the observer places the front of his eye during observation. In the image formation pathway we have also a set of conjugate planes, consisting of the field diaphragm, the focused specimen, the intermediate image plane, and the retina of the eye or the film plane of the camera. According to the Köhler illumination and Abbes improvements of the lenses design (*33*) we can make use of high numerical apertures for the objectives. But, why do we need higher numerical apertures (*N.A.*) for our objectives? The answer for this question is given by the Rayleigh equation which defines the resolution or the minimum distance between two just resolved objects *(d)* as shown in Figure 2-2.2 by:

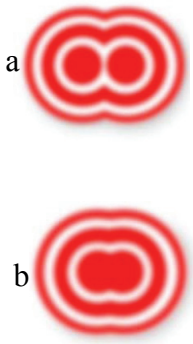

Figure 2-2.2: The effect of the numerical aperture on the resolution. For the same wavelength it is found that as larger the numerical aperture is, the smaller the radius of the resolution Airy discs will be. a) Well resolved objects. b) Just resolved objects (11).

$$d = 1.22 \cdot \left(\frac{\lambda}{2N.A.} \right) \qquad 2\text{-}2.1$$

Here λ is the wavelength of the illuminating beam. Depending on the specific requirements either trans-illumination or epi-illumination of the sample is applied. Trans-illumination involves transmitting the excitation beam through the sample towards the detector. In contrast to trans-illumination one can use the epi-illumination, which involves reflecting the excitation beam from the sample (*34*). Epi-illumination is typically used in fluorescence microscopy and gives the opportunity to use only one objective. The excitation and emission (image forming) pathways are shown in Figure 2-2.5, see next subsection.

Today mainly two different types of high resolution optical microscopes are employed in fluorescence microscopy. One is the wide-field microscope imaging an extended area

directly and the other one is the confocal laser scanning microscope (CLSM) which forms an image by raster scanning.

2-2.1 Wide-field microscope

Wide-field microscopes are powerful tools for time resolved imaging. Also in some cases wide field technique causes lower photobleaching than laser scanning techniques. As Wolfgang Becker et al. said" *Since the increase of photobleaching with the power is nonlinear it should be expected that wide field imaging is less affected by photobleaching than scanning techniques*" (*35*). In our particular case we used the wide field setup for imaging samples labeled with one dye or with two dyes of different colors. For this purpose we used an argon ion gas laser (*from Coherent, Inc., Santa Clara, CA, USA*) which provides us different lines in the range of blue and green light (475-477- 488- 496- 501- 514- 528 nm). These lines were divided by a 50/50 beam splitter and one part was directed into a dye laser (*from Radiant Dyes Laser Acc. GmbH, Wermelskirchen, NRW,Germany*). For obtaining excitation light at 635 nm we used the dye *DCM-Pyran CH_3CN* which gives red laser light with a broad spectrum. The desired wavelengths (488 or 528 and 635 nm) were cleaned with laser clean filters (*from Omega Optical, Inc. Brattleboro, VT, USA*). As shown in Figure 2-2.3 these laser beams were guided and combined for simultaneous or alternating two color excitation.

For epi-illumination we used two different multiband dichroic mirrors according to the dyes used sample and the respective excitation lines, to deflect the laser beams towards the microscope. We used a microscope (IX-81 from Olympus) with an auto-focus option, which is equipped with an IR laser to detect the Z-position of the glass slide surface and to move the objective to focus on this surface, see Figure 2-2.4. In this focus drift compensation the IR laser is half blocked and directed towards the objective. If the glass slide is in the focus the part from the focused beam reflected towards a detector through the objective, hence we get a small point-like image of the focus (Fig. 2-2.4b,e). If the glass slide is positioned above or below the objective focus we observe the respective half of the typical circular interference fringes forming an image on the left side (Figures 2-2.4a,d), for a reflection plane below the focus or on the right side (Figures 2-2.4c,f) for a reflection plane above the focus, of the detection plane.

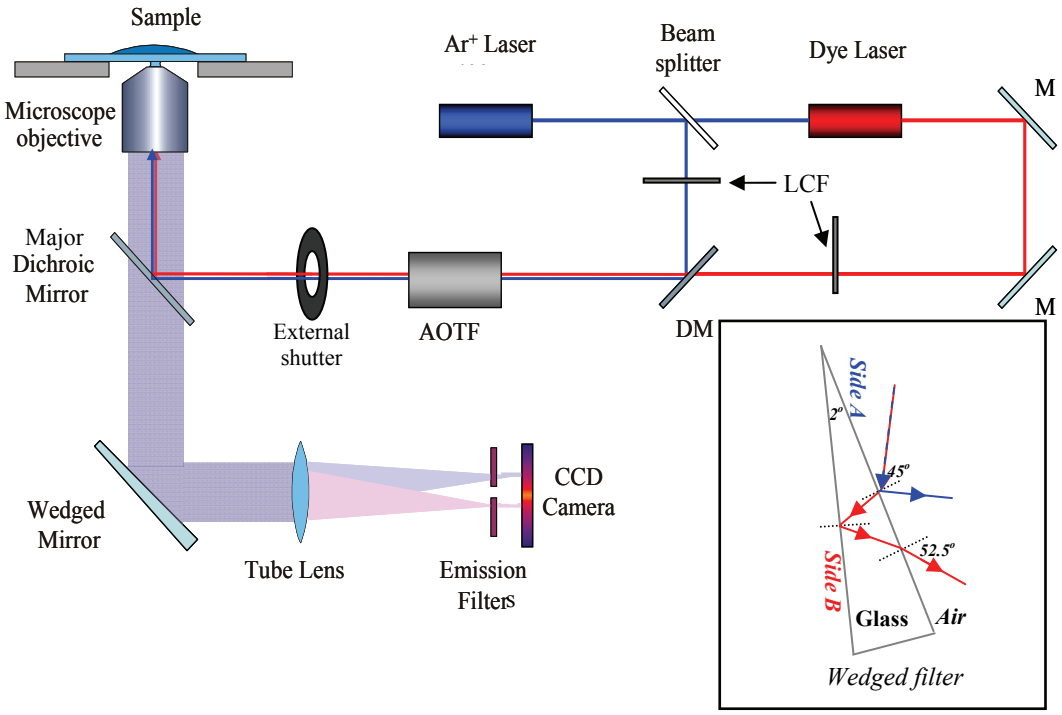

Figure 2-2.3: Schematic draw of our wide field setup. On the lower right corner we can see a schematic draw for the wedged filter and how it splits two different incoming wavelengths. M is a 100% mirror, LCF is a laser cleaning filter, and DM is a dichroic mirror.

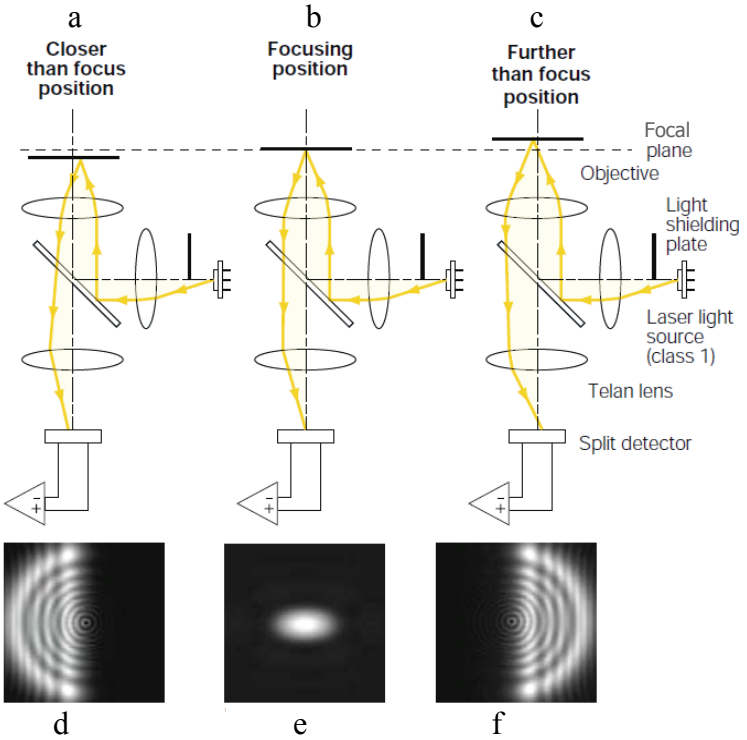

Figure 2-2.4: A schematic draw of the auto-focusing Z-drift compensation (ZDC) unit inside the motorized microscope IX81. When the IR laser beam is reflected through an additional dichroic mirror towards the glass slide, we observe a back-reflection due to changes of refractive index between the glass slide and the immersing medium in the detector plane (9).

To achieve a good wide field illumination we set the optical elements as shown in Figure 2-2.5 and focused the beam on the back focal plan of the objective by using a long focal length lens (not shown in Figure 2-2.5). In our wide field microscope we used an oil immersed UPlansApo objective (*from Olympus Europa Holding, GmbH, Hamburg, Germany*), with 60X magnification power and a N.A. of 1.35. This objective, due to its large numerical aperture, collects a large amount of the fluorescence and guides the fluorescence light to the multiband dichroic mirror. The selected dichroic mirror (see Section 3-1) deflects the excitation beam and transmits the fluorescence light coming from the objective. To this point the fluorescence emission light from different colors is overlapping in space. To separate the overlapped beams we used a wedged mirror (custom order from Omega Optical) as shown in Figure 2-2.3.

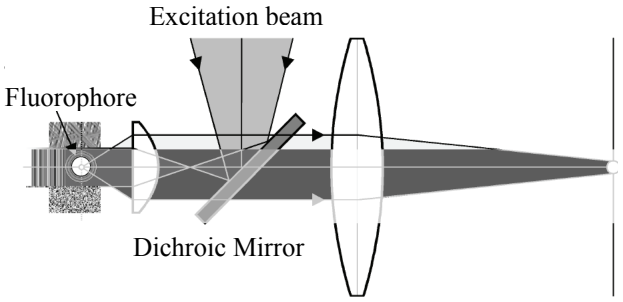

Figure 2-2.5: A schematic draw of a wide field sample illumination.

The wavelength separated beams pass through a tube length and are finally focused through the respective emission filters (*from Omega optical*) on separated areas of a back illuminated CCD camera (*iXon DK-855 from Andor- Technology, South Windsor, CT, USA*). For various applications we needed a fast switch between different laser lines, which was accomplished by the use of an acoustic optical tunable filter (*AOTF from AA Opto-Electronic, Orsay Cedex, France*). The AOTF allows very precise selection of the desired wavelength and regulation of the excitation intensity. A simple program was written using LabVIEW (*software from National Instruments, München, Germany*) to control the acoustic optical tunable filter with the Cell M software (*the microscope software from Olympus*). Also an external shutter (*VCM-D1 from Vincent Associates Uniblitz Corporate Headquarters, NY, USA*) was implemented in the illumination pathway to prevent continues illumination of the fluorophores. The

measured images were treated and analyzed using Image J (*from the National Institute for Health, Maryland, USA*) and custom written matlab routines.

2-2.2 Confocal microscope

In contrast to the conventional wide field imaging the confocal imaging is a raster scanning technique. The scanning method is realized either by moving the laser beam against the position fixed sample or by moving the sample against the position fixed laser. This technique has several advantages with respect to conventional microscopes (*36,37*). A very essential difference between the confocal microscope and the conventional wide field microscope is the presence of a pinhole (called confocal pinhole) (*38*) in one of the conjugate planes of the image forming pathway.

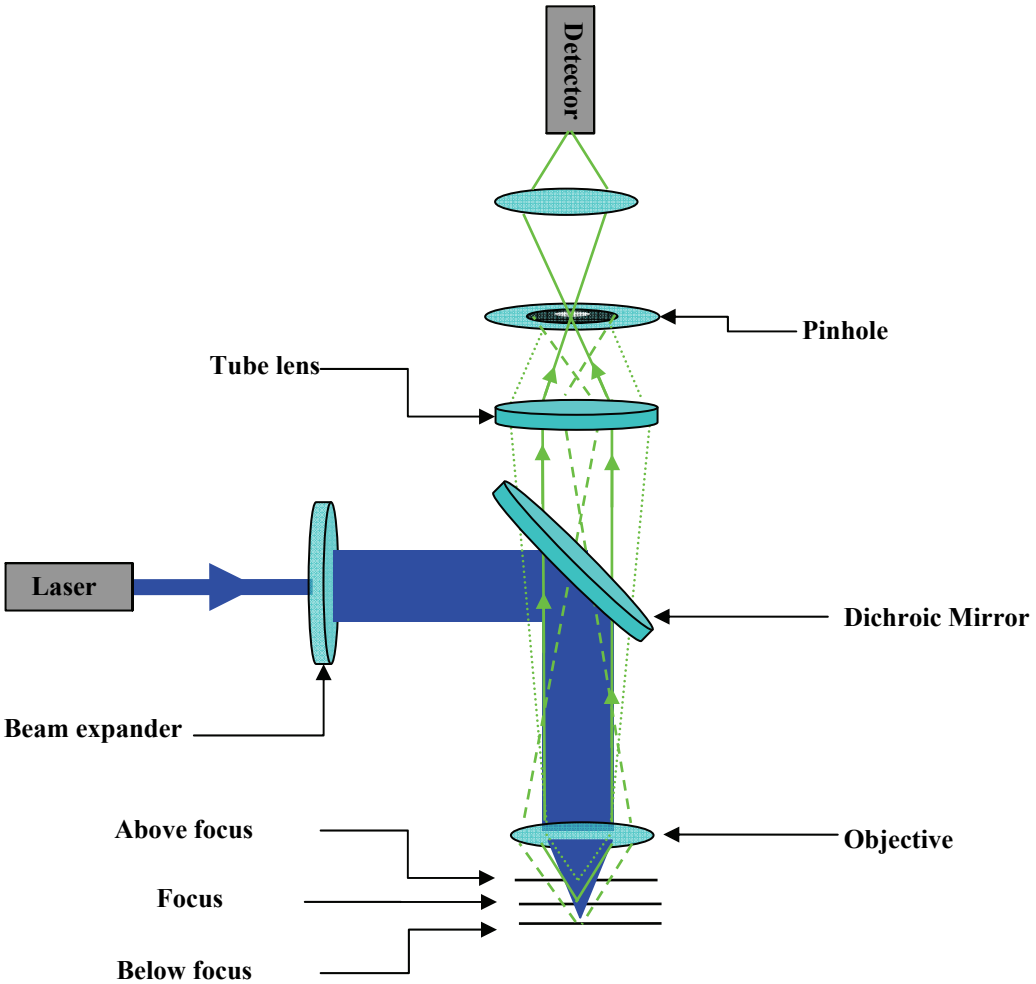

Figure 2-2.6: Schematic drawing for the confocal microscope setup. In the figure we can see the emitted fluorescence coming from different planes above (dotted line) and below (dashed line) the focus blocked by the pinhole.

This pinhole lets pass only fluorescence light coming from the focus and blocks out of focus light. In other words the confocal microscope detects only “in-focus” objects and discards “out of focus” objects (Figure 2-2.6). This property causes reduction in the back ground and enhances the signal to noise ratio significantly. Another important advantage is its ability to detect serially thin optical sections (from 0.5 to 1.5 micrometer) through the fluorescent samples with extended thicknesses (~50 μm) (*39*).

Here we used the confocal microscope MicroTime 200 (*from PicoQuant GmbH, Berlin, Germany*) for FCS measurements (see Section 3-4) and anisotropy measurements (see Section 3-3). As shown in Figure 2-2.7 the excitation beam passes from the pulsed laser source (640 nm and 470 nm diode lasers) through a polarization maintaining single mode fiber to a laser clean filter and is reflected by the so called major dichroic mirror (MDM). The major dichroic mirror deflects the excitation beam to the microscope IX81 (from Olympus) through a beam displacer. The role of the beam displacer is only to compensate for minor misalignment between the microscope and the main optical unit (MOU). The microscope is equipped with a precise 2D piezo scanner to move the sample in the X-Y plane and a PIFOC to move the sample in Z direction. The parallel excitation beam is focused in the sample using an UplanSApo 60X water immerse objective with numerical aperture of N.A=1.2 (*from Olympus*). The fluorescence beam goes back through the same objective and is passing the major dichroic mirror. By means of a convex lens the parallel beam is focused on the pinhole (50 micrometer). Depending on the application we typically split the light with respect to the color (with a dichroic mirror) or with respect to the polarization (with a polarization beam splitter cube). The resulting beams are guided finally to two separate detectors (Single photon avalanche diodes; *SPADs from Perkin–Elmer, Canada*). Respective emission filters are located according to the application either in front of the detector or in between the major dichroic mirror and the pinhole. The arrival time of each detected photon was recorded by a time-correlated single-photon counting (TCSPC) card (*Pico- Harp 300, PicoQuant Berlin, Germany*). Data handling and part of the analysis was performed with the SymphoTime software from PicoQuant. For the purpose of measuring the excitation beam intensity, there is another beam splitter in front of the major dichroic mirror. The beam splitter reflects approximately 10 to 20 percent from the main beam towards a photodiode which measures the beam intensity. A further important issue is to

determine the position of the glass surface. This is provided by a video camera monitoring the image of the back-scattered beam from the glass surface.

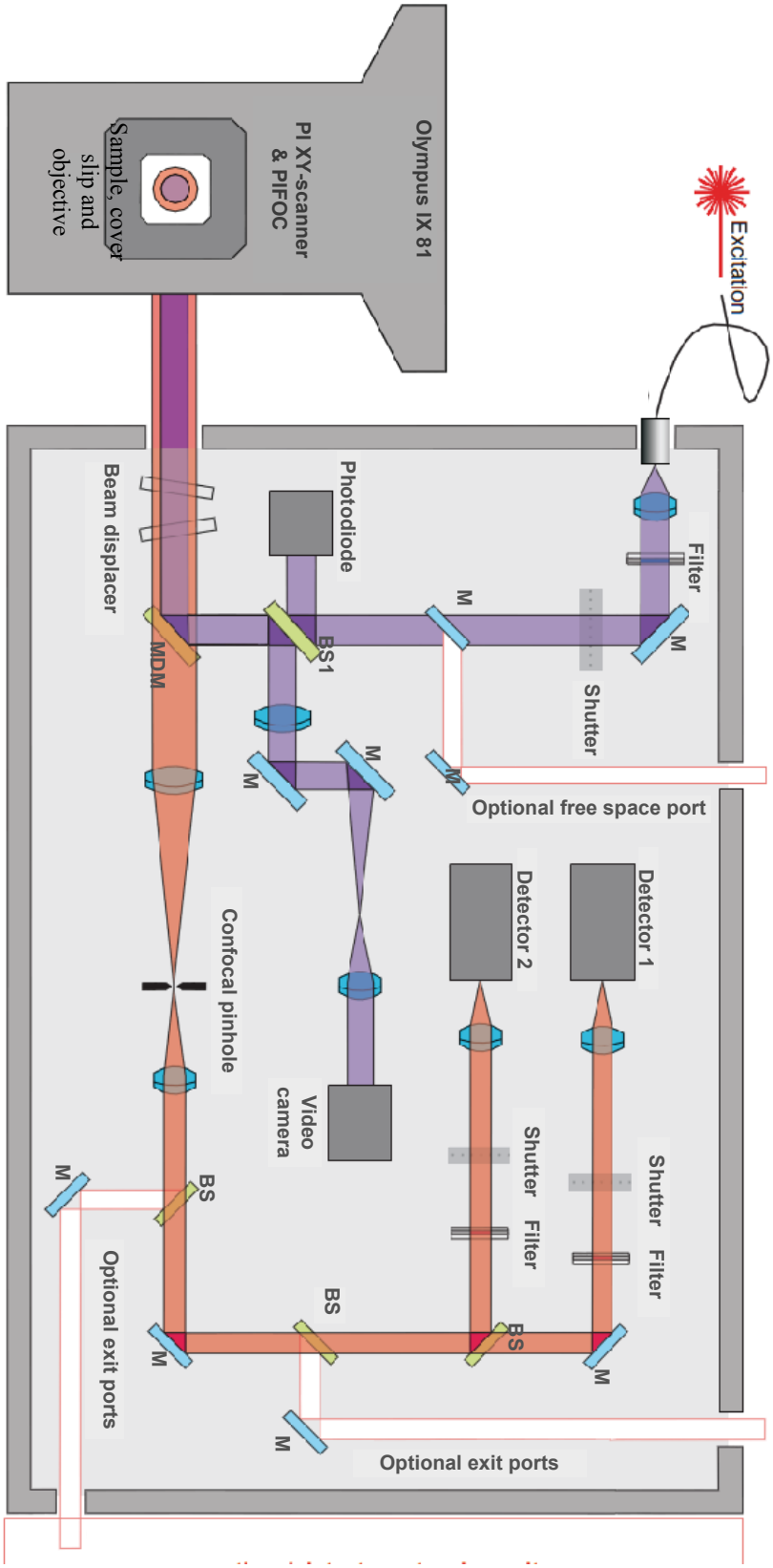

Figure 2-2.7: A schematic draw of the MicroTime 200 (4). M:100% mirror, DM: dichroic mirror, MDM: major dichroic mirror and BS: beam splitter it might be split according to the plane of polarization (cube polarizer beam splitter), to the wavelength (dichroic mirror), or only dividing the wave front (50/50 beam splitter).

2-3 Fluorescence correlation spectroscopy

Fluorescence correlation spectroscopy (FCS) is a powerful spectroscopic detection technique investigating diluted samples down to single-molecule concentration (*40,41*). FCS measures and correlates fluctuations of fluorescence intensity. This section introduces the theoretical background of FCS, which was first realized by D. Magde, E. Elson, and W.W. Webb, as published in 1972 (*42*). In the nineties, due to the introduction of reasonably priced laser sources, FCS became a popular technique as a spectroscopic tool for high resolution (spatial and temporal) studies on ultra-diluted samples (~ a few ten pM to a few nM) (*43,44*). FCS is based on the analysis of intensity time traces. In principle one can apply FCS for immobilized molecules as well, but I will discuss here only the case of diffusing molecules. The main idea in this case is to measure the fluctuating fluorescence intensity of the diffusing molecules through the confocal volume, the latter in the order of few femtoliters (*45*). Typically a small pinhole is used to avoid any fluorescence contributing from outside the confocal volume (see Section 2-2.2). This fluctuation is a result of dynamical processes, mainly the translational diffusion. In addition, conformational changes of the probe can be another source of intensity fluctuation, which makes the fluorophores to work as reporters. The FCS technique is sensitive to processes taking place on almost all time scales, namely from picoseconds to hundreds of milliseconds. The maximum time is practically limited by the fluorophore photostability. Figure 2-3.1 shows some of biomolecular processes and fluorescence relevant timescales. FCS theory describes dynamical processes and delivers information about the investigated molecule in terms of the rates and amplitudes of the intensity fluctuation.

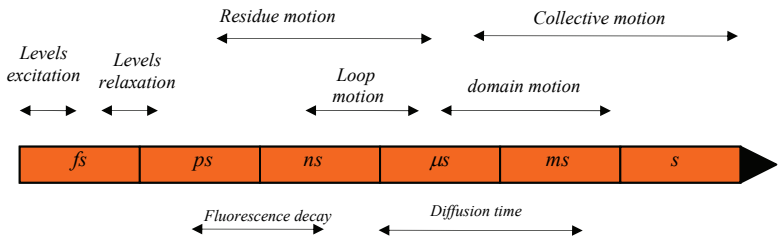

Figure 2-3.1: Biomolecular and fluorescence related time scales. For a diffusing protein, during the diffusion, one can detect the protein dynamics according to the related time scales of these motion. Adopted from Sisamakis, E. et.al (13).

A very important advantage of FCS with diffusing molecule is related to the fact that the molecules are permanently replaced in the confocal volume, and therefore photo-bleaching often is not a crucial limitation.

2-3.1 Theoretical concepts

Depending on the molecule concentration we will measure the corresponding number of molecules in the confocal volume. With an appropriate concentration one can get easily one or two fluorophores diffusing in and out of the detection volume. This diffusion causes an intensity fluctuation. Hence we can compare the intensity *I (t)* with the later one *I (t+τ)* and generate the autocorrelation function *G (τ)*. As will be shown below the amplitude *G(0)* is exactly the reciprocal particle number in the confocal volume, since the intensity fluctuation follows the Poisson statistics (*46*). From the autocorrelation function we can extract physical parameters, such as diffusion coefficients, diffusion times, furthermore we can obtain the molecule concentration. The autocorrelation function *G (τ)* is the time average of the product of the intensity *I(t)* at time (*t),* with the intensity *I(t+τ)* at later time (*t+τ*) *(47-49),*

$$G(t) = < I(t)\ I(t+\tau) > = \frac{1}{T}\int_0^T I(t)\ I(t+\tau)\ dt \qquad 2\text{-}3.1$$

where *T* is the data accumulation time. The factor $\frac{1}{T}$ is for normalization. If <*I*> is the mean value of the intensity *I (t)* then the quantity of interest will be $\delta I(t)$.

$$\delta I(t) = < I > - I(t) \qquad 2\text{-}3.2$$

The autocorrelation function can be normalized by the squared average intensity.

$$G'(\tau) = \frac{< I(t)\ I(t+\tau) >}{< I >^2} \qquad 2\text{-}3.3$$

In the previous equation $G'(\tau)$ is the normalized autocorrelation function, *t* is the initial time and τ is the time delay. If we do not correlate to the initial time, but to the previous intensity measurements, we will set *t* to *zero.* Hence τ will be always the time difference between the successive intensity measurements (*50*).

$$G(\tau) = \frac{< I(0)\ I(\tau) >}{< I >^2} \qquad 2\text{-}3.4$$

For interpreting the FCS data we need a model to describe the intensity fluctuation. For this purpose the molecular brightness (B) is a reasonable choice. One can define the brightness as the number of photons observed per second for a fluorophore (*3,51*).

$$B = q\ \varepsilon\ Q \qquad 2\text{-}3.5$$

Here q is the detection efficiency of the optical setup, ε is the molar absorption coefficient and Q is the quantum yield of the dye. We have to assume an intensity profile for the focused laser. A suitable profile is the three dimensional Gaussian profile (*52,53*) as shown in Figure 2-3.2.

$$p(r) = I_o e^{\frac{-2(X^2+Y^2)}{\omega_o^2}} e^{\frac{-2Z^2}{z_o^2}} \qquad 2\text{-}3.6$$

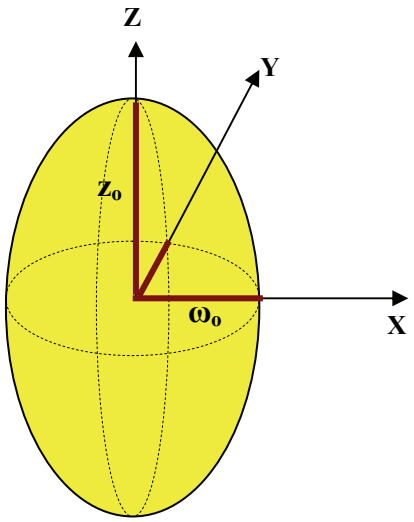

Figure 2-3.2: The detection volume shows the Gaussian profile of intensity distribution.

Hence if we state $\delta C(r,t)$ as the fluctuation in concentration during the diffusion, one can rewrite Equation 2-3.2 by the following (*48*):

$$\delta I(t) = \int_V B\ I_o\ p(r)\ \delta C(r,t)\ dV \qquad 2\text{-}3.7$$

Integrating Equation 2-3.7, dividing by I_o, and squaring the result will give:

$$< I >^2 = [B\ C \int_V p(r)\ dV]^2 \qquad 2\text{-}3.8$$

From Equations 2-3.7, 2-3.8 and 2-3.4 we can understand that the autocorrelation function G is depending only on the position distance if r is the distance at time $t=0$ and r' is the distance at time τ. Using Equations 2-3.7 and 2-3.8 one can rewrite the autocorrelation as follows (56, 57):

$$G(\tau) = \frac{B^2 \iint p(r)\ p(r')\ <\delta C(r,0)\ \delta C(r',\tau)>\ dV\, dV'}{[B\ C \int p(r)\ dV]^2} \qquad 2\text{-}3.9$$

In real experiments the molecules diffuse in three dimensions with a diffusion coefficient *D*. Now I will define the parameter called density autocorrelation. This term can be written as follows (*47*):

$$<\delta C(r,0)\ \delta C(r',\tau)> = \overline{C}\ \ (4\pi\ D\ \tau)^{\frac{3}{2}}\ e^{\frac{-|r-r'|^2}{4\ D\ \tau}} \qquad 2\text{-}3.10$$

Rewriting Equation 2-3.9 using Equations 2-3.10 and 2-3.6 one can get:

$$G(\tau) = G(0)\left(1+\frac{4D\ \tau}{\omega_o^2}\right)^{-1}\left(1+\frac{4D\ \tau}{z_o^2}\right)^{-\frac{1}{2}} \qquad 2\text{-}3.11$$

where *G(0)* is the amplitude at *t*=0 *(3)*. If the diffusion time is $\tau_D = \frac{\omega_o^2}{4D}$ (*50*) hence we can rewrite Equation 2-3.11 as:

$$G(\tau) = G(0)\left(1+\frac{\tau}{\tau_D}\right)^{-1}\left(1+\left(\frac{\omega_o}{z_o}\right)^2\frac{\tau}{\tau_D}\right)^{-\frac{1}{2}} \qquad 2\text{-}3.12$$

The confocal volume can be calculated using the following equation:

$$V = \pi^{\frac{3}{2}}\ \omega_o^2\ z_o \qquad 2\text{-}3.13$$

With the average number of molecules inside the volume:

$$\langle N \rangle = \frac{1}{G(0)} \qquad 2\text{-}3.14$$

A typical example of an autocorrelation curve is shown in Figure 3-2.3. From the curve one can determine the value of *G(0)* and the diffusion time τ_D. To extract the information from the autocorrelation curve one has to apply models, for example the

model given in Equation 2-3.10. Assuming that different types of particles are present in our sample, the autocorrelation function will be composed of a sum of various decays, each of them with an individual decay time τ_i.

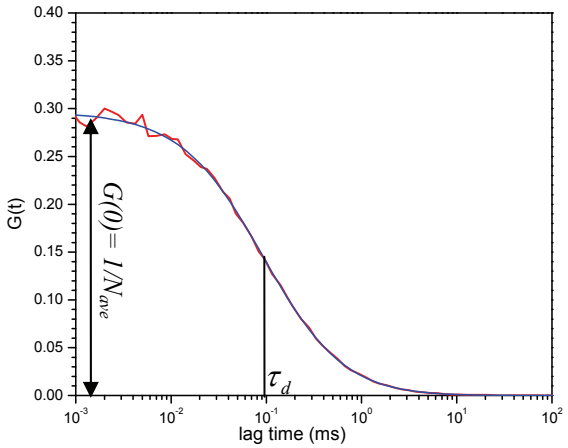

Figure 2-3.3: Autocorrelation curve shows the diffusion of free Alexa488. The red line is the autocorrelation and the blue line is the fitting according to a pure diffusion model (see Equation 2-3.18). From the fit we can determine the diffusion time and the average number (N_{ave}) of the diffusing particle in the respective confocal volume (and by this the molar concentration).

The first model we deal with is the pure translational diffusion. This model suggests a diffusing particle with a constant fluorophore intensity and is given by the following Equation (*54,55*):

$$G(\tau) = \sum_{i=1}^{n} G_i(0)\left(1+\frac{\tau}{\tau_i}\right)^{-1}\left(1+\frac{\tau}{\tau_i \kappa^2}\right)^{-\frac{1}{2}} \qquad 2\text{-}3.15$$

$$\kappa = \frac{z_o}{\omega_o},\ < C >= \frac{< N >}{V\, N_A} \qquad 2\text{-}3.16$$

here N_A is Avogadro's number, <*N*> is the temporal averaged mean number of particles in detection volume V and τ_i is the diffusion time of the ith species (for example due to different sizes). During the diffusion it may be probable, that further dynamical processes take place, such like conformational dynamics within the biomolecule. In this case we can use the following fitting model (*56,57*):

$$G(\tau)=\left(1+A_C e^{\left(\frac{-\tau}{\tau_c}\right)^{\beta_c}}\right)\frac{1}{<N>}\left(1+\frac{\tau}{\tau_D}\right)^{-1}\left(1+\frac{\tau}{\tau_D\ \kappa^2}\right)^{-\frac{1}{2}} \qquad 2\text{-}3.17$$

$$A_C=\frac{K(1-Q)^2}{(1+KQ)^2}\ \ and\ \ \kappa=\frac{z_o}{\omega_o} \qquad 2\text{-}3.18$$

where Q is the ratio between the quantum yields of state 1 and of state 2, β_C is a stretched exponent parameter and K is the equilibrium parameter. In addition intersystem crossing may take place which can lead to temporal dark states. In this particular case the model will be (*58,59*):

$$G(\tau)=\left(1-A_{trp}+A_{trp}e^{\left(-\frac{\tau}{\tau_{trp}}\right)}\right)\sum_{i=1}^{n}G_i(0)\left(1+\frac{\tau}{\tau_{D_i}}\right)^{-1}\left(1+\frac{\tau}{\tau_{D_i}\kappa^2}\right)^{-\frac{1}{2}} \qquad 2\text{-}3.19$$

Here A_{trp} is the amplitude of the dark (triplet) fraction of molecules, τ_{trp} is the life time of the triplet state, τ_{Di} is the diffusion time of the i^{th} species. In this case the average number of diffusing particles will be:

$$<N>=\frac{1}{G(0)(1-A_{trp})} \qquad 2\text{-}3.20$$

All the previous models are valid for particle diffusion in 3D. In the case of detection volumes with much larger Z- dimensions as compared to the X- and Y- dimensions (κ > 5) one can employ in a good approximation a 2D diffusion model. Hence one can write the previous models by eliminating the term $\left(1+\frac{\tau}{\tau_{D_i}\kappa^2}\right)^{-\frac{1}{2}}$, in this case for example Equation 2-3.19 will be (*58,59*):

$$G(\tau)=\left(1-A_{trp}+A_{trp}e^{\left(-\frac{\tau}{\tau_{trp}}\right)}\right)\sum_{i=1}^{n}G_i(0)\left(1+\frac{\tau}{\tau_i}\right)^{-1} \qquad 2\text{-}3.21$$

To obtain structural information from the diffusing particles (in our case proteins) we relate the diffusion coefficient to parameters characterizing the size and the structure of proteins. From the Stokes-Einstein equation we obtain this relation between the molecular size and the diffusion coefficient:

$$D = \frac{k_B T}{6\ \pi\ \eta\ R_h} \qquad 2\text{-}3.22$$

In this equation k_B is Boltzmann constant, T is the temperature in Kelvin, η is the viscosity of the medium, and R_h is the hydrodynamic radius of a spherical diffusing particle. From R_h we obtain the molecular mass M_w with the specific volume $\bar{v}$ as follows (*3*):

$$R_h = \left(\frac{3 M_w \bar{v}}{4\pi} \right)^{\frac{1}{3}} \qquad 2\text{-}3.23$$

From Equations 2-3.22 and 2-3.23 we get:

$$D = \frac{k_B T}{6\ \pi\ \eta} \sqrt[3]{\frac{4\pi}{3 M_w \bar{v}}} \qquad 2\text{-}3.24$$

Equation 2-3.24 gives the relation between the diffusion coefficient and the molecular mass. In some cases we have to study the chemical induced unfolding of proteins using guanidine hydrochloride (GdnHCl). In this particular case high concentrations (up to 6M) of such chemical substances will affect the viscosity and the refractive index of the buffer solution (*61*). So we have to consider these effects on the optical properties of the confocal detection volume. We can rewrite Equations 2-3.13 using the ratio κ as given in Equations 2-3.16 and 2-3.18 in the following way:

$$V = \pi^{\frac{3}{2}}\ \omega_o^3\ \kappa \qquad 2\text{-}3.25$$

While the relation between the lag time τ and the lateral diffusion coefficient D is given by (*60*):

$$\omega_o^2 = 4 D \tau \qquad 2\text{-}3.26$$

From Equations 2-3.28 and 2-3.29 we obtain:

$$V = \pi^{\frac{3}{2}} (4D\ \tau)^{\frac{3}{2}} \kappa \qquad 2\text{-}3.27$$

Using Equation 2-3.22 and Equation 2-3.27 the result will be:

$$V = \pi^{\frac{3}{2}} \left[\frac{4k_B T \tau}{6\ \pi\ \eta\ R_h} \right]^{\frac{3}{2}} \kappa \qquad 2\text{-}3.28$$

In Figure 2-3.4 we can see this dependence, namely the effect of changes in the refractive index and the corresponding diffusion coefficients.

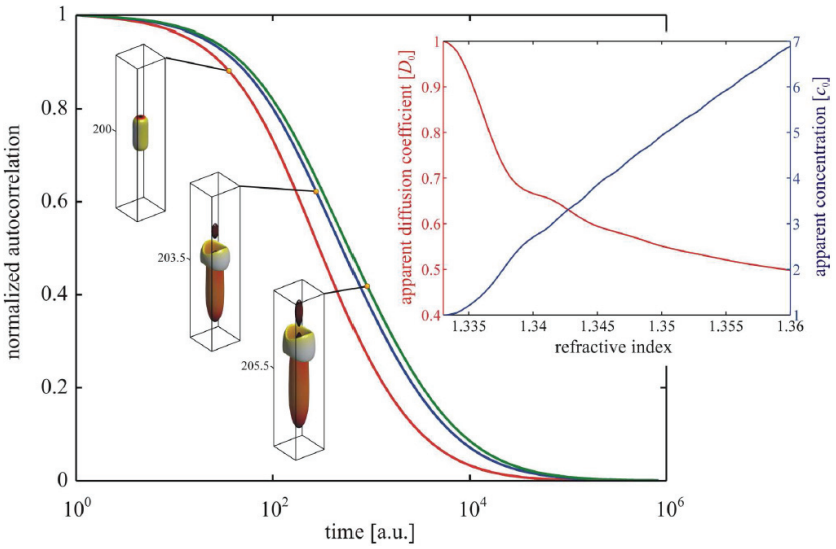

Figure 2-3.4: The dependence of the diffusion coefficient and the apparent concentration on the refractive index of the sample. It is clear that as the concentration increased the diffusion coefficient decreased. The auto-correlation curves show the changes in the confocal volume during the increase of the concentration (see corresponding auto-correlation curves from red to the green). This figure is adopted from Thomas Dertinger dissertation (10).

2-4 Photoinduced electron transfer (PET)

Photoinduced electron transfer is an important process in photosynthesis and in other organic reactions. It also plays a role as a reporter for detecting conformational

dynamics in biological molecules (*62,63*). Furthermore, PET is widely used in DNA studies and sequence analysis (*64*). Photoinduced electron transfer is a process which can occur in two different scenarios (*65,66*). First the fluorophore is excited by absorbing a photon. (a) In the case of an "electron-rich" donor the electron is transferred from an electron donating molecule (D, the quencher) to an electron accepting molecule (A, the fluorophore). This process called also reductive electron transfer (as shown in Figure 2-4.1 a). (b) If the quencher molecule is "electron-poor" then an electron is transferred from the donor to the acceptor ground state. This process called oxidative electron transfer (as shown in Figure 2-4.1 b).

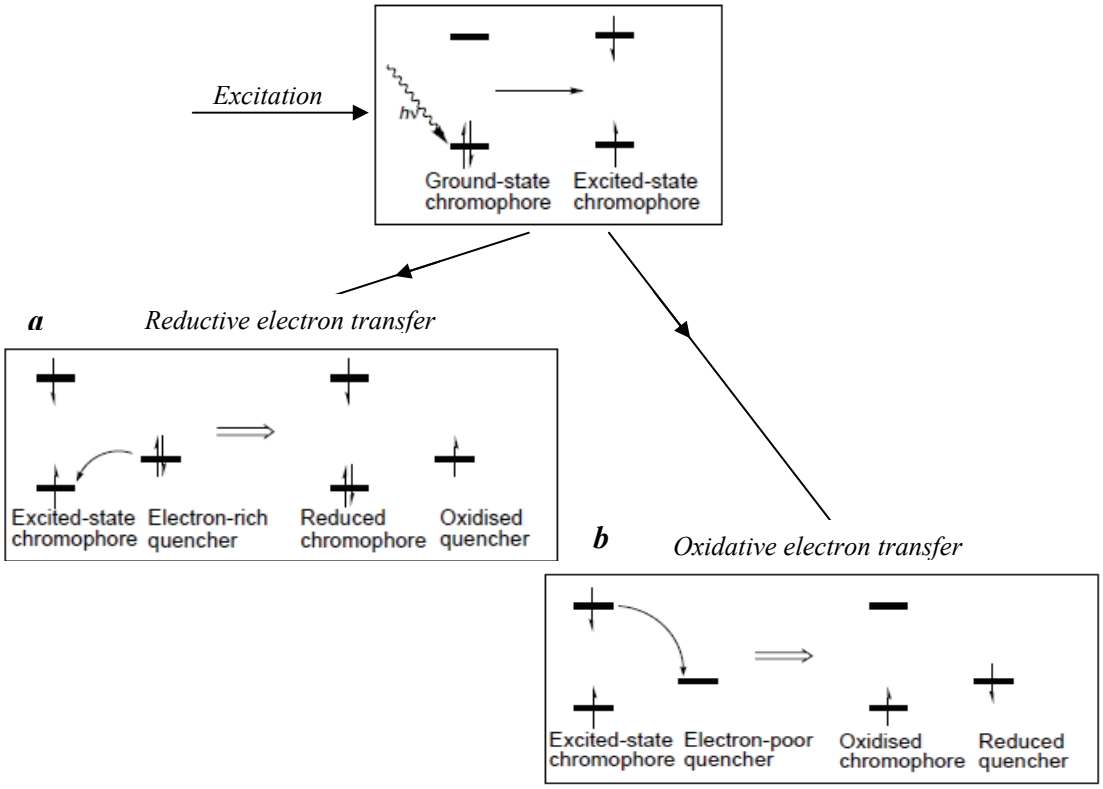

Figure 2-4.1: Schematic diagram illustrating the electron transfer in both mechanisms for acceptor excitation, a) reduction, b) oxidative.

In general one has not always to excite the electron acceptor, but in some molecule systems the fluorophore acts as an electron donor (*67*). Since in both cases the fluorescence is always discarded, PET is also regarded as quenching process (*68*). PET can happen transiently through intermolecular collisions (dynamical quenching) or can

occur during molecular complexes formation. This complex is often stable for multiple excitation-emission cycles (static quenching) (*69*). Fluorophore quenching due to PET can take place in solids or in liquids. Since our interest is in studying protein conformations, I will discuss the relevant mechanisms for liquid state samples only. As shown in Figure 2-4.2 at first due to the Brownian motion the acceptor could move towards the donor molecule, meanwhile it fluoresces. When the distance becomes very short (fractions of nanometer) a complex can be formed. In our case of an Atto655 labeled protein with tryptophan residues in the vicinity of the fluorophore, tryptophan quenches the Atto655 fluorescence and the complex formation of both is regarded as reductive electron transfer (*69-71*).

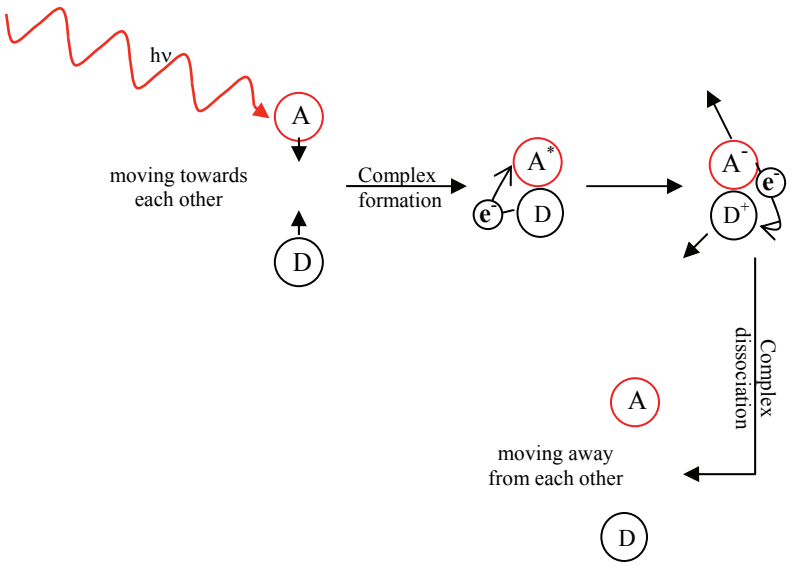

Figure 2-4.2: Schematic diagram illustrating the PET process the curved arrows include an electron transfer.

During the complex formation hybridization takes place between both the levels of molecules. As a result of this hybridization an electron is transferred from the donor to the acceptor ground state, forming a radical cation and an anion (*72,73*). After some time the complex is dissociating and an electron is transferred back to the donor. In some cases exciplex emission is observed. As a consequence of these processes the fluorescence intensity, and in the case of dynamic quenching also the fluorescence lifetimes, are decreases.

Förster resonance energy transfer (FRET) and PET are two methods measuring the change of the fluorescence intensity. The change in fluorescence intensity takes place due to the presence of another molecule according to inter-distance changing. Whereas FRET takes place between a donor (D) molecule to an acceptor (A) molecule (see section 2-1.1 part d). The working distance for FRET depends on the value of the Förster radius R_o which is normally in the range of a few nanometers. On the other hand PET requires contact formation for efficient quenching with a separation between D and A on the range of fractions of nanometer length scale. So, PET is a method to measure structural fluctuations with much small amplitudes of motion.

2-5 Anisotropy

When polarized light hits a fluorescent molecule the resulting emitted fluorescence will be also polarized. The rotation of the plane of polarization is a valuable reporter of the fluorophore rotation. If a fixed molecule is excited with polarized light we have a polarized emitted light. In case of a rotational diffusing molecule emitted photons will be in different planes, as shown in Figure 2-5.1.

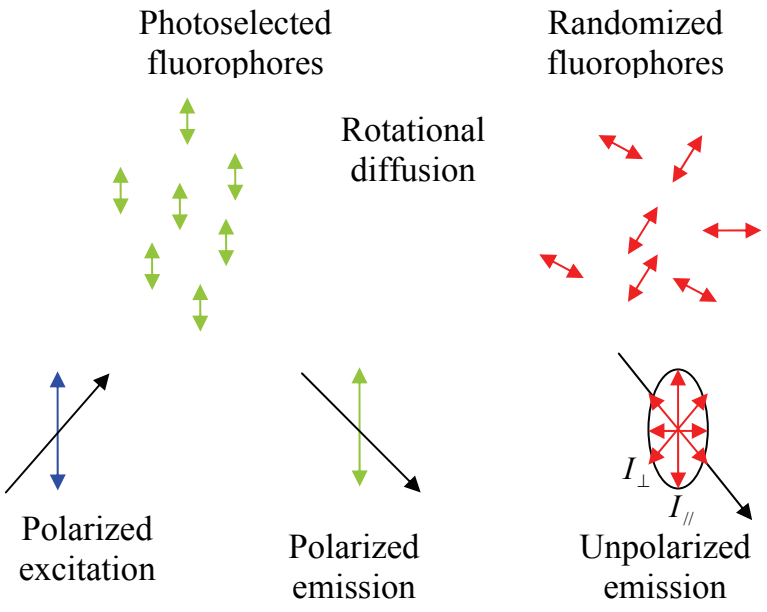

Figure 2-5.1: Effects of polarized excitation and of rotational diffusion on the polarization of the emitted light (3). The black line is the direction of the light propagation, while the red, the green, and the blue lines represent the oscillation direction of the electric field of the unpolarized wave, the polarized emitted wave, and the excitation wave, respectively.

Hence the term fluorescence anisotropy is defined in a way that it assigns the rotational diffusion of a molecule to the polarization of fluorescence photons.

Anisotropy measurements with fluorescently labeled proteins typically provide information on the size and on the shape of proteins (*3,74-76*). They can give the average angular displacement of the fluorophore which occurs in the time between the absorption and the fluorescence emission. The measured angular displacement is depending on the rate of the rotational diffusion during the excited state lifetime. The environment viscosity also affects the rotational diffusion.

2-5.1 How to measure the anisotropy

As shown in Figure 2-5.2, if we have a vertical polarized beam with intensity I_v, adopted with a polarizer which excites the fluorophores in the sample.

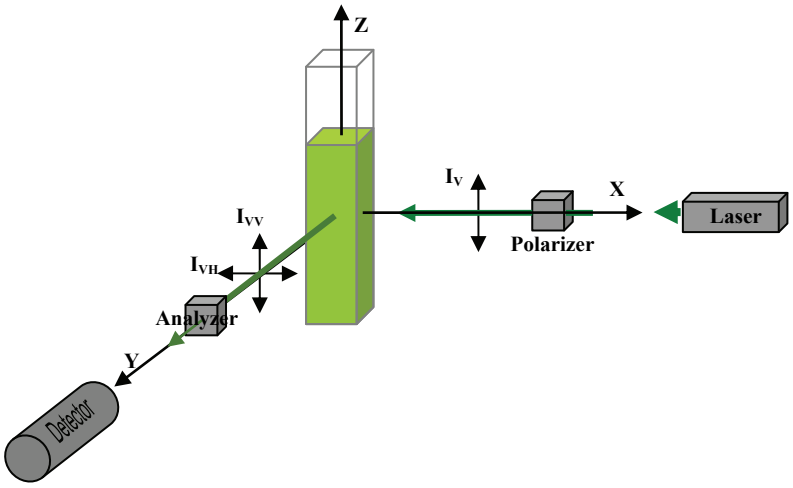

Figure 2-5.2: Schematic diagram for measurement of fluorescence.

The emitted light may have an altered polarization with respect to the excitation. The anisotropy *r* will be given by (*3*) :

$$r = \frac{I_{VV} - I_{VH}}{I_{VV} + 2I_{VH}} \qquad 2\text{-}5.1$$

One can rewrite the anisotropy in terms of the rotation angle between absorbed and emitted photon wave. Here (θ) is the angle of the emission dipole relative to the z-axis (we assumed that the excitation wave electric vector is parallel to the z-axis as in Figure

2-5.2). For freely rotating fluorophores and considering the photoselection we obtain for the fundamental anisotropy in the absence of any other depolarizing processes:

$$r_o = \frac{2}{5}\left(\frac{3\cos^2(\beta)-1}{2}\right) \qquad 2\text{-}5.2$$

Here β is the angle between the absorption and emission transitions. From this equation one can calculate the limits of the anisotropy. For freely rotating fluorophores we have a complete loss of anisotropy ($r = 0$) with a corresponding $\beta = 54.7°$ (*3*). Furthermore, r_o will have maximum value if $cos^2\beta$ is *1*. This occurs for fixed fluorophores i.e. $\beta = 0°$. Hence the fundamental anisotropy will be 0.4. Due to the fact that the detection efficiency is practically slightly different in both detection channels, we have to correct for this. In the case of vertically polarized excitation we will have I_{VV} (*parallel*) and I_{VH} (*perpendicular*) emitted intensity. These intensities will be corrected for different sensitivities of both channels S_V and $S_{H,}$ by:

$$\frac{I_{VV}}{I_{VH}} = \frac{S_V I_{//}}{S_H I_{\perp}} = G\frac{I_{//}}{I_{\perp}} \qquad 2\text{-}5.3$$

Here the G factor is easily measured using horizontally polarized excitation. With horizontally polarized excitation the excitation direction is perpendicular to both observation directions. When this is done both the horizontally and vertically polarized components must be equal. Hence the G factor can be calculated by:

$$G = \frac{I_{HV}}{I_{HH}} \qquad 2\text{-}5.4$$

and the anisotropy will be rewritten according to the previous relation as follow:

$$r = \frac{I_{VV} - G\, I_{VH}}{I_{VV} + 2G\, I_{VH}} \qquad 2\text{-}5.5$$

While the previous setup shown in Figure 2-5.2 is called L-format, there is another setup called T-format shown in Figure 2-5.3.

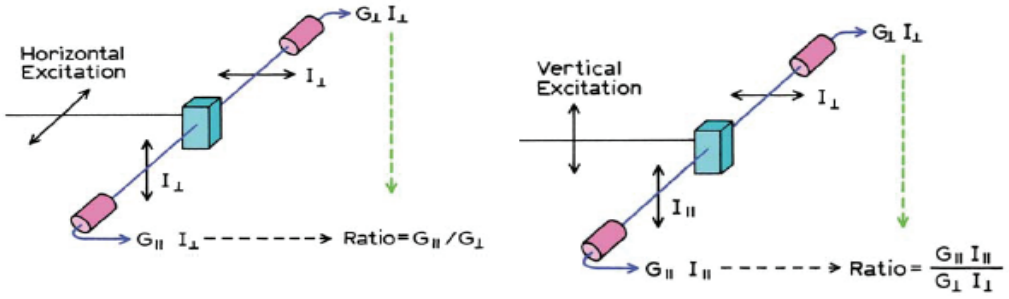

Figure 2-5.3:Schematic illustration of the T-format setup for anisotropy measurements (3).

In the T-format setup we do not have only one detection channel, but we have two detection channels. One channel detects the parallel beam and the second one is detecting the perpendicular beam. Because of the presence of these two channels every channel will have its own *G*-factor so we will have $G_{//}$ for the parallel channel and $G_{\perp}$ for the second channel. In this case we define a new factor, *R*-factor.

$$R_V = \frac{G_{//}\, I_{//}}{G_{\perp}\, I_{\perp}} \quad \text{and} \quad R_H = \frac{G_{//}}{G_{\perp}} \tag{2-5.6}$$

Hence we can divide both R_V and R_H producing the ratio *R*

$$R = \frac{R_V}{R_H} = \frac{I_{//}}{I_{\perp}} \tag{2-5.7}$$

Using Equations 2-5.3 and 2-5.4 one can get the following equation

$$r = \frac{I_{//}/I_{\perp} - 1}{I_{//}/I_{\perp} + 2} \tag{2-5.8}$$

2-5.2 Effects of rotational diffusion on the anisotropy

A major reason for the fluorescence depolarization is the rotational diffusion of the fluorophore. The anisotropy is not only due to the dye rotation but also a combination of dye rotation and part of the whole molecule rotation (dye attached to the molecule of interest). If the fundamental anisotropy of a dye is r_o and the measured

(apparent) anisotropy is $r_{a,}$ the depolarization by rotational diffusion of spherical rotors can be described by the Perrin equation (*3,77,78*):

$$r_o = r_a\left(1+\frac{\tau}{\tau_c}\right) \qquad 2\text{-}5.9$$

where τ is the decay life time of the fluorophore, and τ_c is the rotational correlation time of the molecule. Here τ_c is also a function of the medium viscosity η, the temperature T in Kelvin units, and the volume of the rotating unit *V (79)*:

$$\tau_c = \frac{\eta\, V}{R\, T} \qquad 2\text{-}5.10$$

where *R* is the gas constant.

2-5.3 Time dependent anisotropy

In the previous section I discussed mainly steady-state fluorescence anisotropy. Steady state anisotropy is measured during continuous illumination and reveals a time averaged value of the anisotropy decay (often called r_o). In addition to this value one can obtain more detailed information from the anisotropy decays. By comparing the measured decay with the decays calculated from different molecular models we get information about the size, the shape, and some times about the internal flexibility of the measured molecules (*80*). Time resolved anisotropy decays are typically measured with pulsed excitation. According to Equation 2-5.8 the time dependent anisotropy is given by:

$$r(t) = \frac{I_{//}(t) - I_{\perp}(t)}{I_{//}(t) + 2I_{\perp}(t)} \qquad 2\text{-}5.11$$

Depending on the molecule measured, the anisotropy decay can be more complex if the fluorophore is not spherical or if the fluorophore environment limits its mobility. In the case of non-spherical molecules we will have multiple correlation times and the decay will be described by a multi exponential decay. Hence the anisotropy decay for anisotropic rotors is be given by:

$$r(t) = \sum_{i=1}^{n} r_i(0) \; e^{-\frac{t}{\tau_{ci}}} \qquad 2\text{-}5.12$$

Here τ_{ci} is the ith component of the rotational correlation time and $r_i(0)$ is the ith component of the zero time anisotropy. "*There may be as many as five exponential terms for an asymmetric body, but in practice only three correlation times are expected to be distinguishable" (Joseph R.Lakowitz, (81)).* In the case of anisotropic media we will get also complex decays. For example in the case of fluorophores attached to proteins, the fluorophore will not be able to perform a complete free rotation. The rotation of this dye will be limited in three dimensions (i.e. spherical rotor). This kind of motion can be described as a motion inside a cone with head angle θ. The anisotropy in this case will be limited and the decay will not go exponentially to zero, (hindered rotor). It is described by:

$$r(t) = (r\,(0) - r_\infty)\; e^{-\frac{t}{\tau_c}} + r_\infty \qquad 2\text{-}5.13$$

where r_∞ is the limited anisotropy. To derive reasonable parameters from the anisotropy decays (see Equation 2-5.13) one has to consider the instrument response function (IRF). This can be done either by a deconvolution procedure or in the case of a rather narrow IRFs (see red line in Fig. 2-5.4), simply by applying a so-called tail fit. For our purposes it was sufficient to apply tail-fits, see Figure 2-5.4.

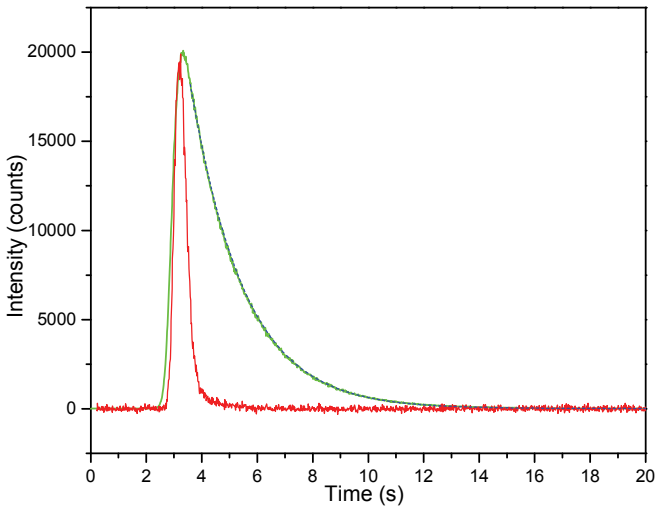

Figure 2-5.4: The instrument response function (measured with a solely scattering sample) for one of the detectors (the red curve) and the fluorescence life time decay of the Atto655 (green curve) is shown here. The tail fitting is represented by dashed blue line (hidden behind the green line). All data was measured with laser line at 640 nm.

2-6 Glass slide preparation for single molecule measurements

In principle we have two different kinds of samples, diffusing molecules and surface tethered molecules. In the case of diffusing molecules we have a droplet of buffer which contains a very low concentration (fractions of nM) of labeled protein. We typically measured diffusing molecules in a diffraction limited detection volume (see Section 2.3). In order to avoid unspecific binding for our molecules to the surface we needed a surface blocking. For this purpose we can use slides covered with mPEG as will be explained in the next section. In the literature (*82,83*) another method is mentioned, where a Tween 20 solution *(*Polyoxyethylene-20-sorbitan monolaurate from *Carl Roth GmbH + Co. KG, Karlsruhe, Germany)* is added to the buffer solution. It is sufficient to add a concentration of 0.001% w/v of Tween 20 to our buffers, which blocked the glass surface efficiently.

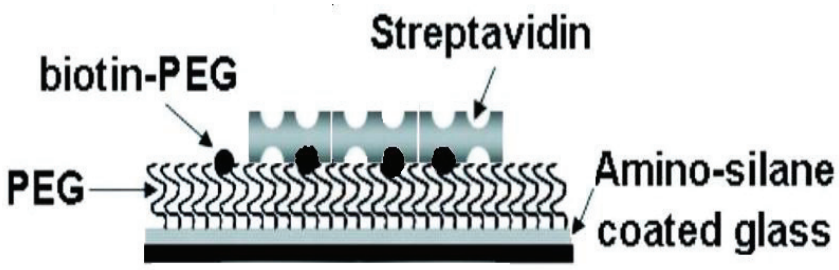

Figure 2-6.1: A schematic draw of a glass slide for protein tethering. The black line shows the glass surface coated with silane (the pale blue line). The mPEG layer is bound covalently to the silane coated surface. In addition to the mPEG we have biotin-PEG which is linked to the streptavidin molecule by a strong linker, through one out of four binding sites. This gives an opportunity to bind any biotinylated molecule to the glass surface.

During the whole measuring time we did not observe protein binding to the surface with samples in the nM concentration range.

In the case of surface tethered molecules, the goal is to image single molecules on the surface. For this purpose we have to suppress unspecific binding and to attach specifically our molecules of interest to the surface. A first step to achieve this is to cover the glass with an amino silane, and a blocking layer of mPEG (Figure 2-6.1). The mPEG layer ensures an efficient blocking of the surface against any unspecific binding. For the specific binding we employed streptavidin as a linker between the biotinylated surface and our biotinylated protein of interest.

2-6.1 Preparing the glass slide for imaging

In order to measure surface tethered molecules *in situ* we have to exchange the buffer during the measurements. One way to achieve this is employing a closed imaging chamber system. For this purpose we used two glass slides, a large one as base slide and a small one as a cover. The large one was covered with mPEG-SVA 50 mg/ml (Methoxy poly (ethylene glycol) succinimidyl valerate from *Laysan Bio, Inc., Al, USA*) and Biotin-PEG-SVA 5ng/ml (*Laysan Bio, Inc*.) for the specific binding. The small one was covered with mPEG-SAV only, for blocking the upper surface. Afterwards we assembled both glass slides into the imaging chamber *(RC-30HV from Harvard Apparatus, Holliston, MA, USA)* as shown in Figure 2-6.2.

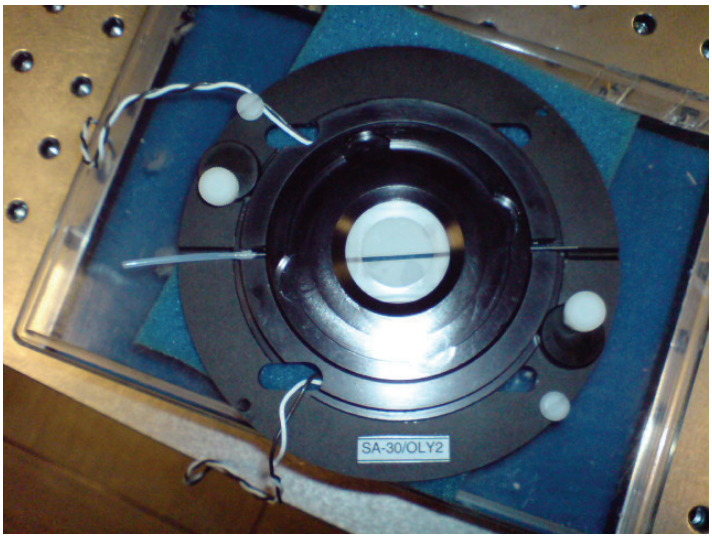

Figure 2-6.2: RC-30 chamber formed with a silicone gasket sandwiched between an upper and a lower cover slide. Pre-cut 250 µm thick slice gaskets forms a channel for solution exchange. The chamber base equipped with small tubes as inlet/outlet for exchanging the buffer.

2-6.2 Protocol for slide preparation and treatment

1- First of all we have to preselect the glass slides. By checking the slides for impurities in the glass caused by fluorescent rare earth elements, we selected only those glass slides which did not have these impurities.

2- We used either good quality pre-cleaned glass slides and arranged the glass slides in metal racks and washed the slides thoroughly in acetone.

3- We treated the glass slides in a plasma cleaner (*PDC-32G from Harrick Plasma, New York, USA*), hence Poly ethylene oxide (*PEO*) surfaces can be formed later (*84*). Afterwards we washed the slides another time in acetone.

4- We prepared the amino silane solution (*from Vector laboratories Inc., CA, USA*) by adding the complete content of a vectabond bottle (*7ml*) to 350 ml of acetone.

5- Immersing the slides in the vectabond solution for 5 minutes. Then washing with deionized water, afterwards the slides must be dried.

6- Preparation of mPEG-SVA solution with a concentration of 50mg/ml in Na_2CO_3 50 mM, pH 8, immerse the slides in the mPEG-SVA solution and incubate the slides with the solution for 3 hours.

7- Preparation of a mPEG-SAV (*50mg/ml*)-Biotin-PEG (*5ng/ml*) solution in Na_2CO_3 at pH 8. Immerse the slides in the solution and incubate the slides for 3 hours.

In both cases (*6*) and (*7*) we have to drain carefully the excess solution after 3 hours, and return the slides to the racks, washing them in deionized water, and put them in 37^{o}C to dry.

8- Mounting the chamber as shown in Figure 2-6.2, using a cover slide with mPEG only (the upper one) and with biotin-PEG for the lower one. For tethering the molecules to the glass we used the biotin-streptavidin binding assay. So we added streptavidin *(from Invitrogen GmbH, Darmstadt, Germany)* to the biotinylated glass slide by injecting a streptavidin solution (*with concentration 2μg/ml*) into the chamber through the tubes, using a syringe or special micro pipette tips.

2-7 Proteins and labeling

In most of our studies we investigated fluorescently labeled proteins. In particular the following enzymes were studied in the present work: PGK (*Phosphoglycerate kinase from baker yeast*), BLA (*α-Amylase from Bacillus licheniformis*), PPA (*α-Amylase from hog pancreas*), and TAKA (*α-Amylase from Aspergillus oryzae*). For our studies we purchased the proteins as powders (*from SIGMA ALDRICH, Steinheim, Germany*). These proteins were dissolved in a native buffer of *10mM MOPS + 50mM NaCl + 2mM EDTA* (*pH 7.4*). The proteins were purified by employing size exclusion chromatography using a PD10 column (Sephadex G-25 matrix from *GE Healthcare*

Bio-sciences, München, Germany). The protein concentrations were determined employing the Beer–Lambert–Bouguer law (*85*). According to this law, molecules in the solution will absorb photons of an incident beam with an intensity I_o at a wavelength λ . The transmitted photon beam intensity (*I*) will be:

$$I(\lambda) = I_{\circ} e^{-C \cdot d \cdot \varepsilon} \qquad 2\text{-}7.1$$

Here *d* is the cuvette thickness in cm, $\boldsymbol{\varepsilon}$ is the molar absorption coefficient of the absorbing molecule in $M^{-1}cm^{-1}$, and *C* is the molecule concentration in M. *ln* (I_o/I) is the absorbance (*A*) which is also called optical density (*OD*) with:

$$A = C \cdot d \cdot \varepsilon \qquad 2\text{-}7.2$$

We measured the absorption using a UV-VIS recording spectrophotometer (UV-2401PC from *SHIMADZU, Duisburg, Germany*). The molar absorption coefficients for our proteins are shown in Table 2-7.1. Afterwards we kept the proteins at -20 °C for short time storing, and at -80 °C for long time storing.

Protein	**PGK**	**BLA**	**TAKA**	**PPA**
Molar absorption coefficient at 280nm [M^{-1} cm^{-1}]	21,430	139,690	118,650	125,820

Table 2-7.1: Molar absorption coefficients of proteins under investigation.

Most proteins carry fluorescent amino acids, like tryptophans, tyrosines and phenylalanines. But the fluorescence from these residues is rather weak. For our purpose (single molecule detection) we have to attach fluorescent dyes to the proteins. In our case we bound the dyes to the proteins via lysine residues, which required NHS-ester functionalized dyes for labeling (Alexa 647-NHS *from Invitrogen, Darmstadt, Germany*, and Atto 655-NHS *from ATTO-TEC GmbH, Siegen, Germany*). For the labeling process we have to exchange the protein native buffer to a labeling buffer (100mM Na_2CO_3 + NaCl 500mM, pH8.3). Although our proteins exhibit many possible lysine residues accessible for binding the dye, the aim here was to obtain a majority of single labeled proteins. In a good approximation this labeling process follows Poisson

statistics (*86*). If μ is the ensemble labeling ratio (the average number of dyes per protein), the probability of finding a protein with N dyes is:

$$P(N,\mu) = \frac{\mu^N}{N!} e^{-\mu} \qquad 2\text{-}7.3$$

By calculating the Poisson probability for different values of label ratios between 1 and 0.1, we can determine which value will correspond, to give a predominantly single labeled protein fraction. The results of some of these calculations are shown in Figure 2-7.2. From this figure we can see that, in case of a label ratio 1 we have 18% of double labeled and 6% of triple labeled proteins. In the case of labeling ratio 0.8 we have about 14% of double labeled and about 4% of triple labeled proteins. But for 0.6 we have a probability of double labeled ones which is 9.9% and approximately 33% for single labeled proteins, this means from the labeled proteins we have more than 71% of single labeled proteins. In the case of lower ratios, as 0.4 and 0.2 we found (*data not shown*) that, the probability of more than one dye per protein is even less. But also the probability of no labels is very high; it went to 80% in the case of labeling ratio 0.2 dyes per protein. This might be a good result, but on the other hand during the diffusion measurements, there are a high number of proteins, which could not be detected (unlabeled). Possibly this will increase the chance of protein aggregation and this may affect the apparent diffusion coefficient. In order to get a dominant fraction of single labeled proteins we used conditions with 0.6 dyes per protein. To achieve this labeling ratio we varied the labeling conditions in terms of dye excess and of incubation time. The final and optimal conditions are listed in the Table 2-7.1. After the incubation time, we have to purify the protein from the free dye and to exchange the labeling buffer back to the native buffer. For this purpose we used again the PD10 column. From the FCS measurement results we know that this was not sufficient to purify the protein. Therefore we employed a longer column, which was prepared in the following way:

a) Incubate Sephadex 25 powder under vacuum in 150mM of NaCl solution for 4 hours. Hence the powder becomes a gel.

b) Put the gel into the long clean column until the gel fills up to 25cm of the column.

c) Exchange the salt buffer by pure water, and eliminate air bubbles. Now the column is ready for purification, after we have to exchange the water by the native buffer.

Protein	PGK	BLA	TAKA	PPA
Dye excess (times)	3	5	3	5
Incubation time (h)	1	3	3	1

Table 2-7.1: Labeling conditions for PGK, BLA, PPA and TAKA. The labeling process always took place in 25 °C.

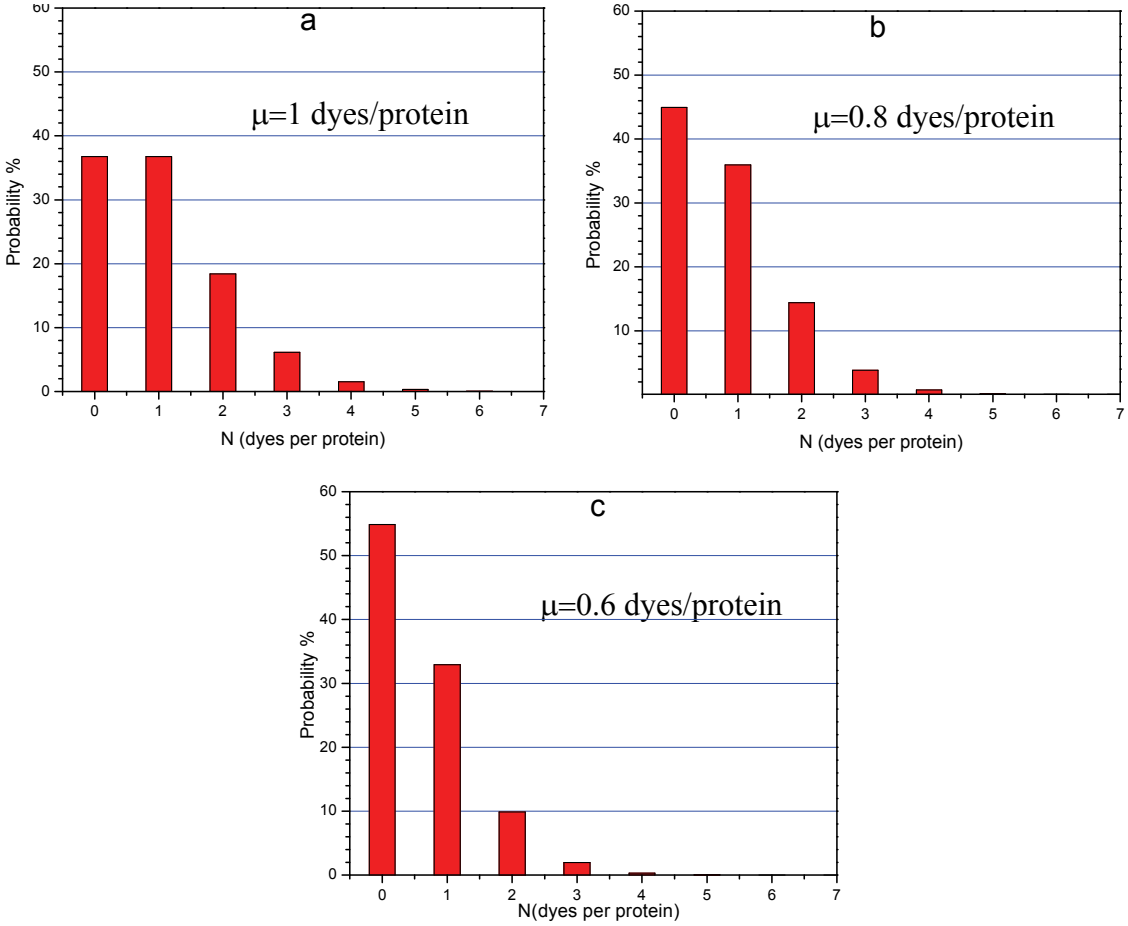

Figure 2-7.2: Poisson distribution of the number of dyes per protein in the case of different average label ratios.

Directly after the incubation time, the solution was applied to the column, and fractions of 1ml were eluted. One example of an elution profiles is shown in Figure 2-7.3.

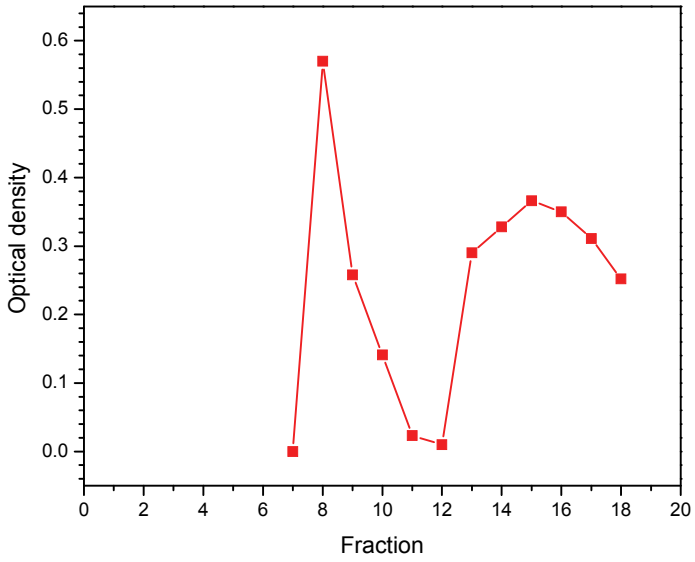

Figure 2-7.3: The elution profile of the BLA labeled with Atto655, absorption measured at λ= 650nm shows two peaks, the first is the protein fraction and the seconded is the free dye fraction. The considered values for O.D. >0.1 are related to fractions from 8 to 10 (protein). The fractions after 10 are contaminated with free dye or contain free dye only which is confirmed by autocorrelation measurements.

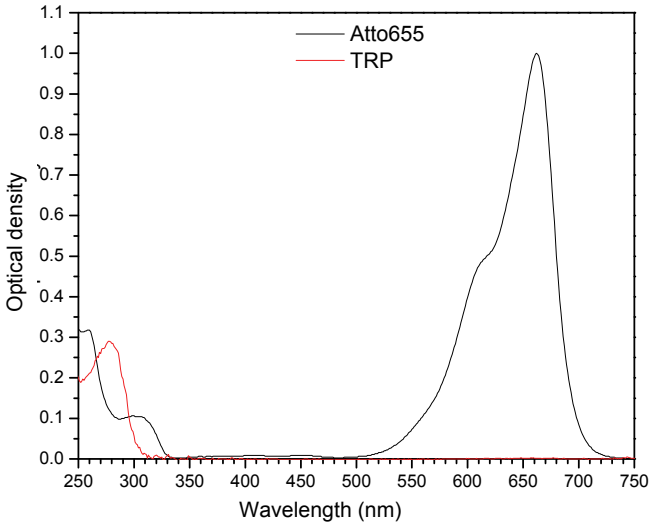

Figure 2-7.4: Absorption spectra of tryptophan in PGK protein (red curve) and of free Atto 655 (black curve). This spectral overlap below 300nm makes it difficult to determine the concentration of the protein if it is labeled with Atto 655.

We could not determine the tryptophan concentration with absorption measurements in the presence of the dye, since the tryptophan absorption peak overlapped with the

absorption peak of Atto655 as shown in Figure 2-7.4. The same holds for Alexa647 (data not shown). For this reason we measured the tryptophan fluorescence of the protein to calculate the protein concentration by using a RF-1501 fluoro-spectrophotometer (*from SHIMADZU*). To determine the protein concentration we employed calibration curves as shown in Figure 2-7.5, measured with known protein concentrations the required protein concentration of labeled protein can be determined by measuring its tryptophan fluorescence and by calculating the concentration by using the calibrations.

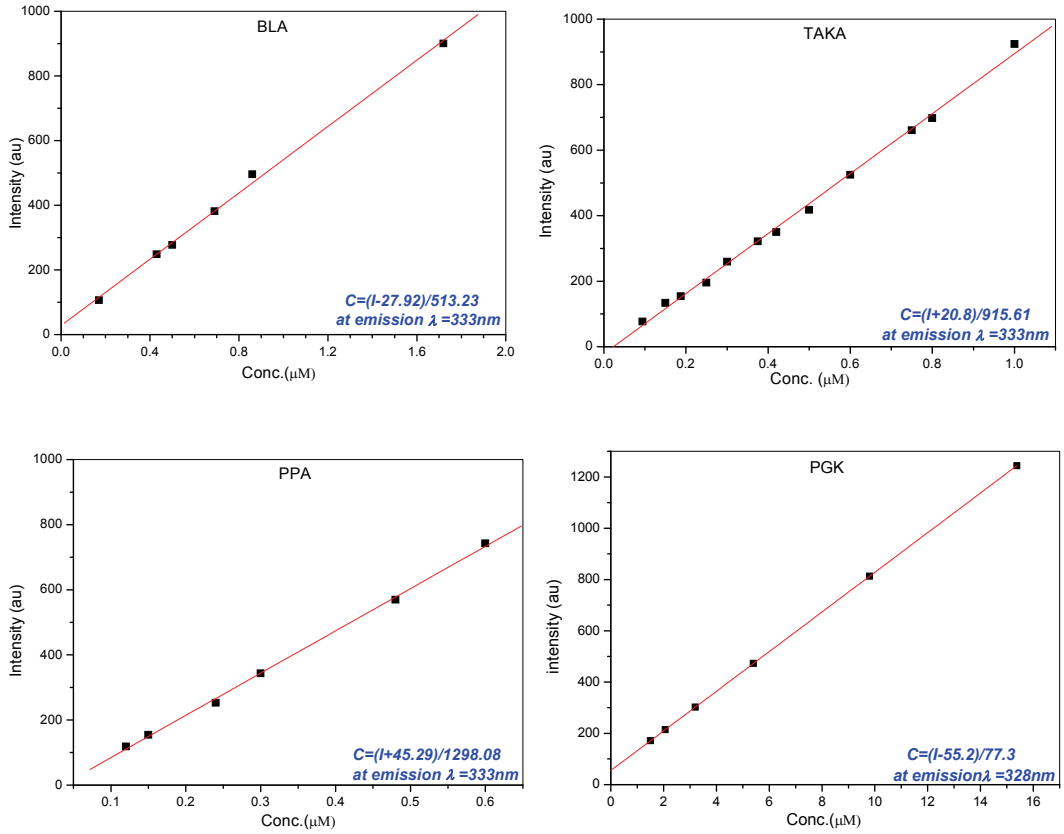

Figure 2-7.4: The calibration curves for the emission of unlabeled PGK, BLA, PPA and TAKA. The black squares are the measured emission intensities at known protein concentration, while the red lines represent the fitting result. All samples were excited at 280nm.

To determine the dye concentration we simply measured the absorption and applied Equation 2-7.1. Knowing both concentrations, we were able to calculate the labeling ratio.

References

1. http://www.olympusmicro.com/primer/anatomy/kohler.html

2. http://www.invitrogen.com/site/us/en/home/References/Molecular-Probes-The-Handbook/Technical -Notes-and-Product-Highlights/Fluorescence-Resonance-Energy-Transfer-FRET.html

3. Lakowicz, J. R. (1999) *Principles of Fluorescence Spectroscopy* Kluwer Academic / Plenum Press, New York.

4. PicoQuant GmbH (2011) Microtime 200, *PicoQuant GmbH*.

5. M.Sauer, J.Hofkens, and J.Enderlein (2011) *Handbook of Fluorescence Spectroscopy and Imaging* WILEY-VCH.

6. Holger Spanggaard (2003) A Mechanical Strain Sensor for Polymeric Materials and Photophysical Investigations of Large Molecules, *Thesis/Dissertation*.

7. M.Heilemann (2005) Design of Single-Molecule Optical Devices: Unidirectional Photonic Wires and Digital Photoswitches, *Thesis/Dissertation*.

8. http://www.scirus.com/srsapp/search?sort=0&t=all&q=fluorescence+&cn=all&co=AND&t=all&q=&cn=all&g=a&fdt=1980&tdt=2012&dt=all&ff=all&ds=jnl&ds=nom&ds=web&sa=agr&sa=chem, *scirus. com*. (2011).

9. Research Inverted System Microscope IX 71/IX 81, (2011), *Catalog*.

10. Thomas Dertinger (2007) Two-Focus Fluorescence Correlation Spectroscopy, *Thesis / Dissertation*

11. E.D.Salmon and Phong Tran (1998) in *Methods in Cell Biology* (Greenfield Sluder and David E.Wolf, Eds.) pp 153-184, Academic Press, San Diego CA.

12. http://historydb.adlerplanetarium.org/herschel/?p=biblio

13. Sisamakis, E., Valeri, A., Kalinin, S., Rothwell, P. J., and Seidel, C. A. (2010) in *Single Molecule Tools, Part B:Super-Resolution, Particle Tracking, Multiparameter, and Force Based Methods* (Nils G.Walter, Ed.) pp 455-514, Elsevier Inc..

14. Nicolas J.Turro, Juan C.Scaiano, and V.Ramamurthy (2008) *Principles of Molecular Photochemistry: an Introduction* University Science Books.

15. David Halliday, Robert Resnick, and Jearl Walker (2001) *Halliday Physics* WILEY-VCH.

16. Bruno Pignataro (2009) *Tomorrow's Chemistry today Concepts in Nanoscince,Organic Materials and Environmental Chemistry* WILEY-VCH.

17. Ottolenghi, M., Goldschmidt, C. R., and Potashnik, R. (1971) Intersystem Crossing in the Charge-Transfer Quenching of Molecular Fluorescence, *The Journal of Physical Chemistry 75*, 1025-1031.

18. Zhang, J., Roek, D. P., Chateauneuf, J. E., and Brennecke, J. F. (1997) A Steady-State and Time-Resolved Fluorescence Study of Quenching Reactions of Anthracene and 1,2-Benzanthracene by Carbon Tetrabromide and Bromoethane in Supercritical Carbon Dioxide, *Journal of the American Chemical Society 119*, 9980-9991.

19. Dreeskamp, H., Laufer, A., and Zander, M. (1984) Quencing of Perylene Fluorescence by Ag+ Ions via Exciplex Formation, *Chemical Physics Letters 112*, 479-482.

20. L Song, E J Hennink, I T Young, and H J Tanke (1995) Photobleaching Kinetics of Fluorescein in Quantitative Fluorescence Microscopy, *Biophys J 68*, 2588-2600.

21. Benjamin Schuler (2010) in *Protein Folding Protocols* (Y.Bal and R.Nussinov, Eds.) pp 115-138, Humana Press, New York, USA.

22. Kuzmenkina, E. V., Heyes, C. D., and Nienhaus, G. U. (2005) Single-Molecule Frster Resonance Energy Transfer Study of Protein Dynamics under Denaturing Conditions, *Proc. Natl. Acad. Sci. U. S. A 102*, 15471-15476.

23. Sapsford, K. E., Berti, L., and Medintz, I. L. (2006) Materials for fluorescence resonance energy transfer analysis: Beyond traditional donor-acceptor combinations, *Angewandte Chemie-International Edition 45*, 4562-4588.

24. Gruber, B. A. and Leonard, N. J. (1975) Dynamic and Static Quenching of 1,N6-Ethenoadenine Fluorescence in Nicotinamide 1,N6-Ethenoadenine Dinucleotide and in 1,N6-Etheno-9-[3-(Indol-3-Yl)Propyl]Adenine, *Proceedings of the National Academy of Sciences of the United States of America 72*, 3966-3969.

25. Mansbach, J. (2006) Introduction to Optical Microscopy-Objectives, *Microscopy and Microanalysis 12*, 1754-1755.

26. Giovani Battista Amici: Optical Instrument Maker, Astronomer, Naturalist, (2011) *http://gbamici. sns. it/eng/strumenti/microscopio_acromatico. htm*.

27. Michael W.Davidson (2005) Nineteenth Century Microscopes, *http://micro. magnet. fsu. edu/primer/museum/museum1800. html*.

28. Olaf Hollricher and Wolfram Ibach (2011) in *Confocal Raman Microscopy* (Dieing Thomas, Hollricher Olaf, and Toporski Jan, Eds.) pp 1-20, Springer-Verlag GmbH, Heidelberg, Heidelberg.

29. Michael W.Davidson and Mortimer Abramowitz. (2002) *Optical Microscopy. Encyclopedia of Imaging Science and Technology* John Wiley and Sons, Incorporation.

30. Carl Zeiss - A History Of A Most Respected Name In Optics, (2011) *http://www. msscweb. org/public/articles/History_of_Zeiss. pdf*.

31. Douglas B.Murphy (2001) *Fundamentals of Light Microscopy and Electronic Imaging* A John Wiley and Sons,Inc.,Publication, New York,USA.

32. Michael W.Davidson and Mortimer Abramowitz. Optical Microscopy. Olympus America . 1999.

33. http://labmed.ascpjournals.org/content/40/8/502.full

34. H.Gross, F.Blechinger, and B.Achtner (2008) in *Handbook of Optical Systems Survey of Optical Instruments* (Herbert Gross, Ed.) pp 555-722, WILLY-VCH Verlag GmbH& KGaA, Weinheim.

35. Wolfgang Becker and axel Bergmann (2003) Lifetime Imaging Techniques for Optical Microscopy, *Becker & Hickl GmbH*.

36. Drazba, J. (2006) Introduction to Confocal Microscopy, *Microscopy and Microanalysis 12*, 1756-1757.

37. Furrer, P. A. S. C., Mayer, J. M., and Gurny, R. O. B. E. (1997) Review Confocal Microscopy as a Tool for the Investigation of the Anterior Part of the Eye, *Journal of Ocular Pharmacology and Therapeutics 13*, 559-578.

38. James B.Pawley (2006) in *Handbook Of Biological Confocal Microscopy* (James B.Pawley, Ed.) pp 20-42, Springer Science+Business Media, New York.

39. Nathan S.Claxton, Tomas J.Fellers, and Michael W.Davidson (2004) Laser Scanning Confocal Microscopy, *http://www. olympusconfocal. com/theory/LSCMIntro. pdf* 1-37.

40. Wahl, M., Gregor, I., Patting, M., and Enderlein, J. (2003) Fast Calculation of Fluorescence Correlation Data with Asynchronous Time-Correlated Single-Photon Counting, *Opt. Express 11*, 3583-3591.

41. Gosch, M., Serov, A., Anhut, T., Lasser, T., Rochas, A., Besse, P. A., Popovic, R. S., Blom, H., and Rigler, R. (2004) Parallel Single Molecule Detection with a Fully Integrated Single-Photon [bold 2 x 2] CMOS Detector Array, *Journal of Biomedical Optics 9*, 913-921.

42. Magde, D., Elson, E., and Webb, W. W. (1972) Thermodynamic Fluctuations in a Reacting System-Measurement by Fluorescence Correlation Spectroscopy, *Phys. Rev. Lett. 29*, 705-708.

43. R.Rigler and E.S.Elson (2001) *Fluorescence Correlation Spectroscopy: Theory and Applications* Springer.

44. Yu Tian, Michelle M.Martinez, and Dimitri Pappas (2011) Fluorescence Correlation Spectroscopy: A Review of Biochemical and Microfluidic Applications, *Appl Spectrosc 65*, 115-124.

45. Dertinger, T., Pacheco, V., der Hocht, I., Hartmann, R., Gregor, I., and Enderlein, J. (2007) Two-Focus Fluorescence Correlation Spectroscopy: A New Tool for Accurate and Absolute Diffusion Measurements, *Chemphyschem 8*, 433-443.

46. Foeldes-Papp, Z. (2007) `True' Single-Molecule Molecule Observations by Fluorescence Correlation Spectroscopy and Two-Color Fluorescence Cross-Correlation Spectroscopy, *Experimental and Molecular Pathology 82*, 147-155.

47. Schwille, P., Meyer-Almes, F. J., and Rigler, R. (1997) Dual-Color Fluorescence Cross-Correlation Spectroscopy for Multicomponent Diffusional Analysis in Solution, *Biophysical Journal 72*, 1878-1886.

48. Hess, S. T. and Webb, W. W. (2002) Focal Volume Optics and Experimental Artifacts in Confocal Fluorescence Correlation Spectroscopy, *Biophysical Journal 83*, 2300-2317.

49. Berland, K. M., So, P. T., and Gratton, E. (1995) Two-Photon Fluorescence Correlation Spectroscopy: Method and Application to the Intracellular Environment, *Biophysical Journal 68*, 694-701.

50. Meseth, U., Wohland, T., Rigler, R., and Vogel, H. (1999) Resolution of Fluorescence Correlation Measurements, *Biophysical Journal 76*, 1619-1631.

51. Petty, J. T., Fan, C., Story, S. P., Sengupta, B., John Iyer, A., Prudowsky, Z., and Dickson, R. M. (2010) DNA Encapsulation of 10 Silver Atoms Producing a Bright, Modulatable, Near-Infrared-Emitting Cluster, *The Journal of Physical Chemistry Letters 1*, 2524-2529.

52. Wang, Q., Lu, G., Hou, L., Zhang, T., Luo, C., Yang, H., Barbillon, G., Lei, F. H., Marquette, C. A., Perriat, P., Tillement, O., Roux, S., Ouyang, Q., and Gong, Q. (2011) Fluorescence

Correlation Spectroscopy Near Individual Gold Nanoparticle, *Chemical Physics Letters 503*, 256-261.

53. Arne Gennerich and Detlev Schild (2000) Fluorescence Correlation Spectroscopy in Small Cytosolic Compartments Depends Critically on the Diffusion Model Used, *Biophysical Journal 79*, 3294-3306.

54. Saffarian, S. and Elson, E. L. (2003) Statistical Analysis of Fluorescence Correlation Spectroscopy: The Standard Deviation and Bias. *Biophysical Journal* 84, 2030-2042.

55. Wohland, T., Rigler, R., and Vogel, H. (2001) The Standard Deviation in Fluorescence Correlation Spectroscopy, *Biophysical Journal 80*, 2987-2999.

56. Edman, L., Mets, U., and Rigler, R. (1996) Conformational Transitions Monitored for Single Molecules in Solution, *Proceedings of the National Academy of Sciences of the United States of America 93*, 6710-6715.

57. Wennmalm, S., Edman, L., and Rigler, R. (1997) Conformational Fluctuations in Single DNA Molecules, *Proceedings of the National Academy of Sciences of the United States of America 94*, 10641-10646.

58. Haupts, U., Maiti, S., Schwille, P., and Webb, W. W. (1998) Dynamics of Fluorescence Fluctuations in Green Fluorescent Protein Observed by Fluorescence Correlation Spectroscopy, *Proceedings of the National Academy of Sciences 95*, 13573-13578.

59. Schwille, P. (2001) Fluorescence Correlation Spectroscopy and its Potential for Intracellular Applications, *Cell Biochemistry and Biophysics 34*, 383-408.

60. Volker Buschmann, Benedikt Krömer, Felix Koberling, Rainer Macdonald, and Steffen Rüttinger (2007) Quantitative FCS: Determination of the Confocal Volume by FC Sand Bead Scanning with the MicroTime 200, *http://photon-counting. com*.

61. Roy, M., Banerjee, A., and Roy, P. (2009) Partial Molar Volumes and Viscosity B-Coefficients of Nicotinamide in Aqueous Resorcinol Solutions at T = (298.15, 308.15, and 318.15) K, *International Journal of Thermophysics 30*, 515-528.

62. Doose, S., Neuweiler, H., and Sauer, M. (2009) Fluorescence Quenching by Photoinduced Electron Transfer: A Reporter for Conformational Dynamics of Macromolecules, *Chemphyschem 10*, 1389-1398.

63. Gray, H. B. and Winkler, J. R. (1996) Electron Transfer in Proteins, *Annu. Rev. Biochem. 65*, 537-561.

64. Wagenknecht, H. A. (2006) Electron Transfer Processes in DNA: Mechanisms, Biological Relevance and Applications in DNA Analytics, *Nat. Prod. Rep. 23*, 973-1006.

65. Vincenzo Balzani (2001) *Electron Transfer in Chemistry, Principles, Theories, Methods, and Techniques* WILEY-VCH Verlag GmbH, New York.

66. Markus Sauer, Johan Hofkens, and Jrg Enderlein (2011) pp 35-51, WILEY-VCH Verlag GmbH, Weinheim.

67. Noboru, M. (1986) Photoinduced Electron Transfer and Related Phenomena in Polar Solutions - Their Dynamics and Mechanisms Revealed by Recent Picosecond Laser Photolysis and Theoretical Studies, *Journal of Molecular Structure: THEOCHEM 135*, 279-297.

68. van de Linde, S., Krstic, I., Prisner, T., Doose, S., Heilemann, M., and Sauer, M. (2011) Photoinduced Formation of Reversible Dye Radicals and their Impact on Super-Resolution Imaging, *Photochem. Photobiol. Sci. 10*, 499-506.

69. Vaiana, A. C., Neuweiler, H., Schulz, A., Wolfrum, J., Sauer, M., and Smith, J. C. (2003) Fluorescence Quenching of Dyes by Tryptophan:Interactions at Atomic Detail from Combination of Experiment and Computer Simulation, *Journal of the American Chemical Society 125*, 14564-14572.

70. Marme, N., Knemeyer, J. P., Sauer, M., and Wolfrum, J. (2003) Inter- and Intramolecular Fluorescence Quenching of Organic Dyes by Tryptophan, *Bioconjug. Chem. 14*, 1133-1139.

71. Doose, S., Neuweiler, H., and Sauer, M. (2005) A Close Look at Fluorescence Quenching of Organic Dyes by Tryptophan, *Chemphyschem 6*, 2277-2285.

72. Ward, M. D. (1997) Photo-Induced Electron and Energy Transfer in Non-Covalently Bonded Supramolecular Assemblies, *Chem. Soc. Rev. 26*, 365-375.

73. Mataga, N. (1993) Photoinduced Electron-Transfer and Multiple States Mechanisms, *Pure and Applied Chemistry 65*, 1605-1610.

74. Steiner, Robert F. (1983) *Excited States of biopolymers* Plenum Press Corporation, New York.

75. Weber, G. (1952) Polarization of the Fluorescence of Macromolecules 1. Theory and Experimental Method, *Biochemical Journal 51*, 145-155.

76. Weber, G. (1952) Polarization of the Fluorescence of Macromolecules 2. Fluorescent Conjugates of Ovalbumin and Bovine Serum Albumin, *Biochemical Journal 51*, 155-168.

77. David Jameson (2011) Principles of Fluorescence Techniques 2011 Basics Fluorescence Principles I: Overview, Excitation and Emission Spectra, Quantum yields, Polarization/ Anisotropy, *Conference Proceeding*.

78. Yoneto, K., Kevin LI, S., Higuchi, W. I., Jiskoot, W., and Herron, J. N. (1996) Fluorescent Probe Studies of the Interactions of 1-alkyl-2-pyrrolidones with Stratum Corneum Lipid Liposomes, *J. Pharm. Sci. 85*, 511-517.

79. Kim, M., Kim, J., Son, B., and Kang, J. (2010) Dynamics of Bacteriophage R17 Probed with a Long-Lifetime Ru(II) Metal-Ligand Complex, *Journal of Fluorescence 20*, 713-718.

80. Joseph R.Lakowitz (2002) *Topics in Fluorescence Spectroscopy* Kluwer Academic Publishers, New York, Boston, Dordrecht, London, Moscow.

81. Lombardi, J. R. and Dafforn, G. A. (1966) Anisotropic Rotational Relaxation in Rigid Media by Polarized Photoselection, *The Journal of Chemical Physics 44*, 3882-3887.

82. Toshio Morizane, Itsurou Satoha, Naoki Kumagai, Hidetsugu Saito:Akiko Iino, Yasutaka Inagaki, Tetsu Watanabe, K. T., and Masaharu Tsuchiy (1986) New Micro-Glass-Tube Leukocyte Adherence Inhibition Assay Assessing Cell Adherence of Mononuclear Cell Subpopulations Defined by Monoclonal Antibodies, *Journal of Immunological Methods 91*, 225-229.

83. Hongying Zhu, aul S.Dale, Charles W.Caldwell, and Xudong Fan (2009) Rapid and Label-Free Detection of Breast Cancer Biomarker CA15-3 in Clinical Human Serum Samples with Optofluidic Ring Resonator Sensors, *anal. chem 81*, 9858-9865.

84. Groll, J., Amirgoulova, E. V., Ameringer, T., Heyes, C. D., Rocker, C., Nienhaus, G. U., and Moller, M. (2004) Biofunctionalized, ultrathin coatings of cross-linked star-shaped poly(ethylene oxide) allow reversible folding of immobilized proteins, *J Am. Chem. Soc. 126*, 4234-4239.

85. Guenter Gauglitz and Taun Vo-Dinh (2003) *Handbook of Spectroscopy* WILEY-VCH Verlag GmbH & Co. KGaA, Weinheim,Germany.

86. Gennis, R. B. and Cantor, C. R. (1972) Use of Nonspecific Dye Labeling for Singlet Energy-Transfer Measurements in Complex Systems. Simple Model, *Biochemistry 11*, 2509-2517.

3 Results and discussion

3-1 Setting up the microscopes for our single molecule measurements

In order to achieve a high sensitivity in our single molecule measurements, we have to choose suitable sets of filters for the used dyes and we have to perform a few calibrations with both setups, the wide field and the confocal microscope.

3-1.1 Selection of filters and dichroic mirrors for single and dual color imaging

One has to select dichroic mirrors and filters in a way that the fit to the emission and the absorption spectra of the dyes. An example of this choice is shown in Figure 3-1.1.

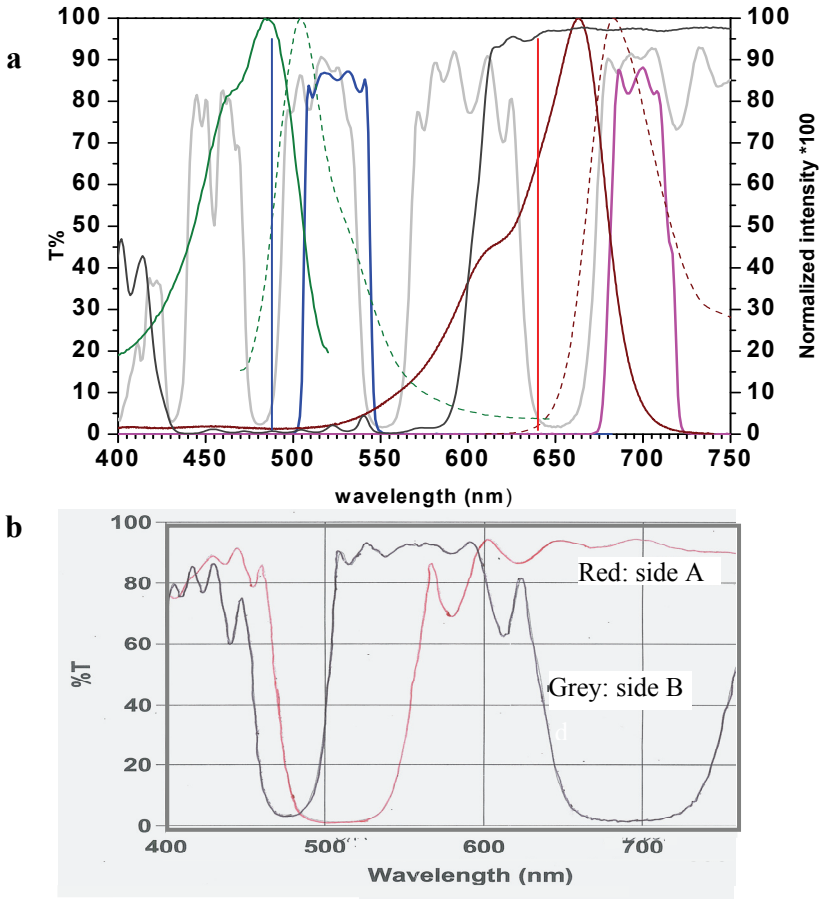

Figure 3-1.1: a) Spectral overlay of the filters and dichroic mirror spectra on an Atto655- GFP pair. According to the spectrum of the dichroic mirrors XF2046 400-485-558-640QBDR (gray line), we can see that the excitation laser lines at 488 nm (the straight blue line) and at 635nm (the straight red line) are good reflected by the multiband dichroic mirror. The excitation lines fit well into the absorption spectra near to the peak, and the emission filters XF3034 690DF40 (blue line), and XF3003 520DF40 (magenta line), cover the respective emission spectra of GFP (green dashed line) and of Atto655 (wine dashed line). The absorption of GFP (green solid line) and of Atto655 (wine solid line) is shown as well. We can separate the emitted fluorescence using a dichroic mirror 600 DCXR (the dark grey line as in the confocal microscope), or using b) a custom made wedged mirror (as in wide field microscope see Figure 2-2.3).

In this example we want to image surface tethered Atto 655 labeled ribosomes, which synthesize the green fluorescence protein (GFP). In this particular case we are dealing with two emission channels, one is the green channel (for the GFP) and the other one is for the red emission of the ribosomes (more details, see Section 3-2). A further important issue is to avoid inelastic Raman scattering, which was also considered by the choice of our emission filters. It is known from the literature (and was also checked by test measurement, data not shown) that the Raman peak becomes weak at excitation wavelengths above 590nm. For this reasons we considered only 470 (488) nm and 532 nm excitation and made sure not to collect light between 570-605 nm (see Fig. 3-1.1) and between 640-670 nm (Fig. 3-1.2), respectively.

In other measurements a BODIPY TMR was incorporated to the synthesized protein, which was accomplished by changing the blue filter to a green one, as shown in Figure 3-1.2.

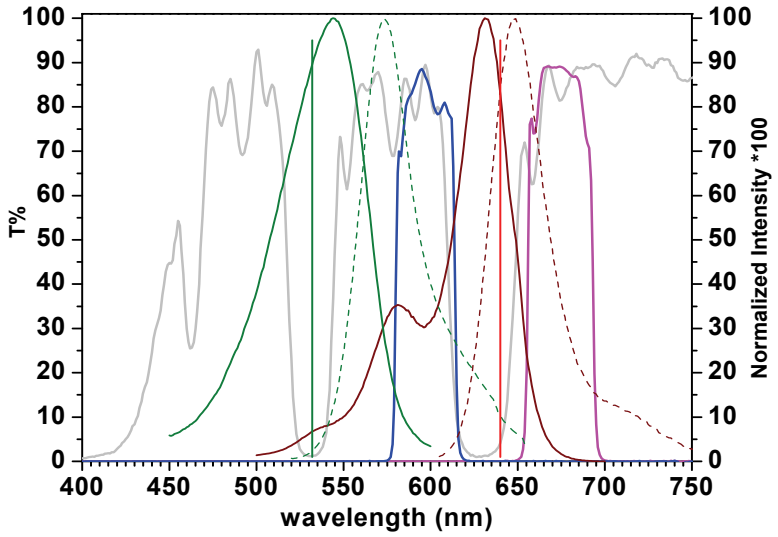

Figure 3-1.2: a) Spectral overlay of the filters and dichroic mirror spectra on an Alexa633- BODIPY TMR pair. According to the spectrum of the dichroics mirror XF2055 400-535-653TBDR (gray line), we can see that the excitation laser lines at 532 nm (the straight green line) and at 635nm (the straight red line) are good reflected by the multiband dichroic mirror. The excitation lines fit well into the absorption spectra near to the peak, and the emission filters XF3034 690DF40 (magenta line), and XF3003 590DF35 (blue line), cover the respective emission spectra of BODIPY TMR (green dashed line) and of Alexa 633 (wine dashed line). The absorption of BODIPY TMR (green solid line) and of Alexa 633 (wine solide line) is shown as well. We can separate the emitted fluorescence using a dichroic mirror 600 DCXR (not shown, as in the confocal microscope) and for wide filed we used another wedged mirror (spectra not shown).

In various other cases we have to measure only one fluorophore, here we either used only one filter and single band dichroic mirror, or we used the same setup for two colors and considered the photons from only one channel. In some of these experiments we studied proteins labeled with Alexa488 or with Atto655 see Figure 3-1.3.

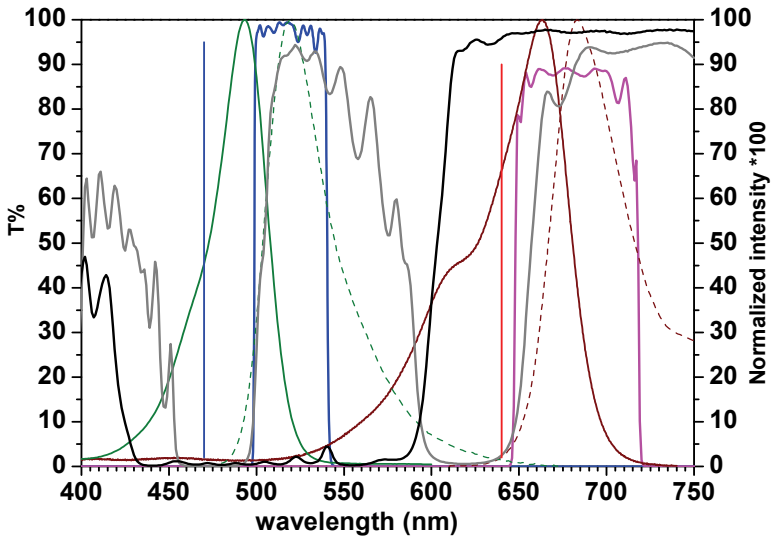

Figure 3-1.3: The same spectral overlay as shown in Figures 3-1.1 and 3-1.2, but for a Atto655-Alexa488 pair. The Dichroic mirror FTIC/CY5 from Chroma Technology Corp, Vermont, USA (gray line), with an excitation laser line 470nm (the straight navy line) and 635nm (the straight red line), the emission filters are HQ 690/70 from Chroma (magenta line), and FF101-520/35 from Semrock-IDEX Corporation, Illinois, USA (blue line). Also it shows the emission spectra of Alexa 488 (green dashed line) and Atto655 (wine dashed line).The absorption of Alexa488 (green solid line) and Atto655 (wine solid line). Like before we separate the emission fluorescence using a dichroic mirror 600 DCXR (black line).

3-1.2 Calibrations for the wide field microscope

A first important check of the setup is to verify that all optical elements are well aligned, that we do not have spectral or image overlap between both detection channels. For this purpose we employed a stage ruler slide (*from Carl Zeiss MicroImaging GmbH, Göttingen*). The stage ruler is a transparent slide divided as a ruler with a 10^{-2} mm scale, as shown in Figure 3-1.4a. The ruler was used to determine and to verify the total magnification of microscope setup. As shown in Figure 3-1.4b we took an image (some times it is better to crop the image to show only the required window in this case we crop an area around 250×250 pixels) with the stage ruler slide to see if the wedged dichroic mirror is well aligned in our setup. A further important issue related to the use of the stage ruler slide is to calibrate the physical dimensions (x and y) of the respective detection areas of the CCD camera. As already shown in Fig. 2-2.3 the wavelength

separation is accomplished by the wedged dichroic mirrors where the upper surface reflects the shorter wavelengths and the longer wavelengths are reflected by the lower surface. If the wedged dichroic mirror is aligned correctly we have two cases:

1- Vertical alignment of the detection channels: Here the red channel image will be the upper one and the blue/green channel image will be the lower one.

2- Horizontal alignment of the detection channels: In this case it was always assured that the red channel appeared on the left and the green/blue channel on the right side.

As shown in Figure 3-1.4 the detection channels are well separated geometrically (spatially). In a next step the wavelength separation of the respective images was checked. For this purpose we measured fluorescent microspheres beads (*from Invitrogen GmbH, Darmstadt, Germany*). For the red channel we used the dark red beads which are efficiently excited with a the 635 nm laser line and fluorescence appeared in the regime from 650 to 750 nm (*57*).

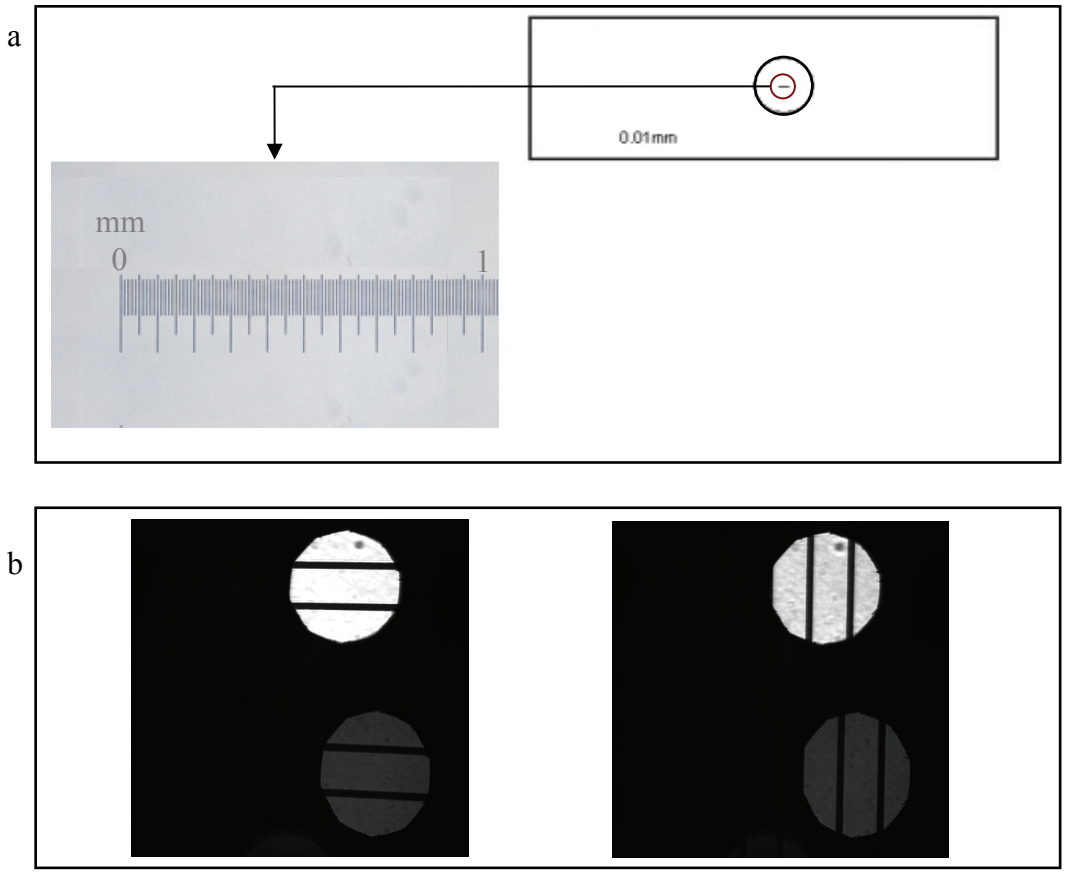

Figure 3-1.4: a) the stage ruler. b) The vertical and horizontal images of the stage ruler slide. From the images we can see that there is no spatial overlap between the channels (upper one from red color and the lower one from blue/green color).

For the blue channels we employed yellow-green fluorescent fluospheres beads which are excited efficiently using the 488 nm line and they fluoresce between 500 and 600 nm (*57*). For the green channel we used orange fluorescent microspheres beads which can be excited at 532 nm and show fluorescence in the regime from 500 to 650 nm (*2*,*49,57*). In Figure 3-1.5 we can see an example of the images from the beads which confirm the spectral separation of both channels. Now we are in a situation that the microscope, the excitation pathway, and the image formation pathway are well aligned. In a next step we have to check our sample protocols of preparation and the sample environment.

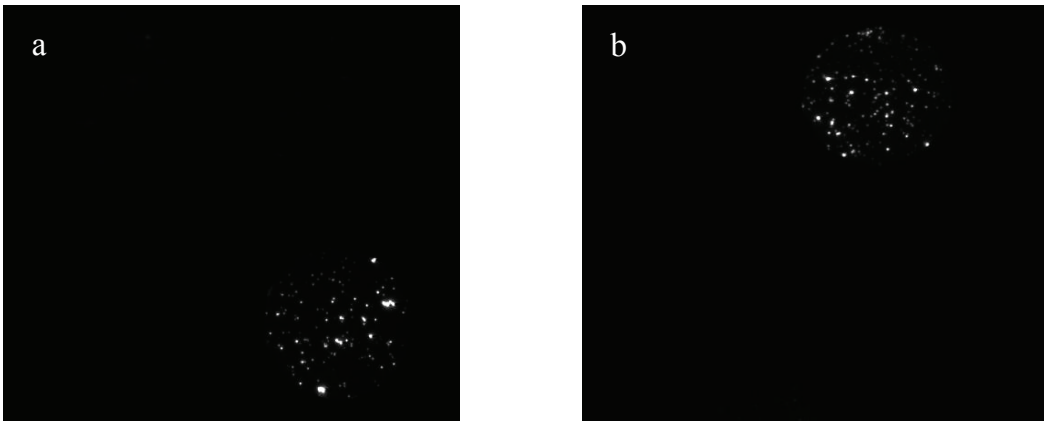

Figure 3-1.5: Fluorescent images of microspheres beads for a) the yellow green beads b) and the dark red beads. From the images a) and b) it is clear that no spots appear in the second channel which confirms the spectral separation of our setup.

For single molecule imaging sensitivity we need cover glass slides, which exhibit as little as possible impurities. Therefore we have to check the glass slides for auto-fluorescent impurities, which typically show up as individual intensity spots (Figure 3-1.6a,b). Every glass slide box included approximately 100 slides, therefore I took a few representative slides from every box and checked them for all laser lines we used. A good glass slide must show a homogenous image (Figure 3-1.6c, d). I found that approximately 90% of the glass slides had auto-fluorescent impurities.

A final important issue was to check whether we are able to image individual surface tethered single molecules. For this purpose we used labeled streptavidin (*from Invitrogen*) either with a red dye (Alexa633) or with a blue dye (Alexa488). I performed photo-bleaching measurements with tethered and dye labeled streptavidin. Following

the bleaching histogram of an individual spot we can conclude whether we imaged a single molecule or not.

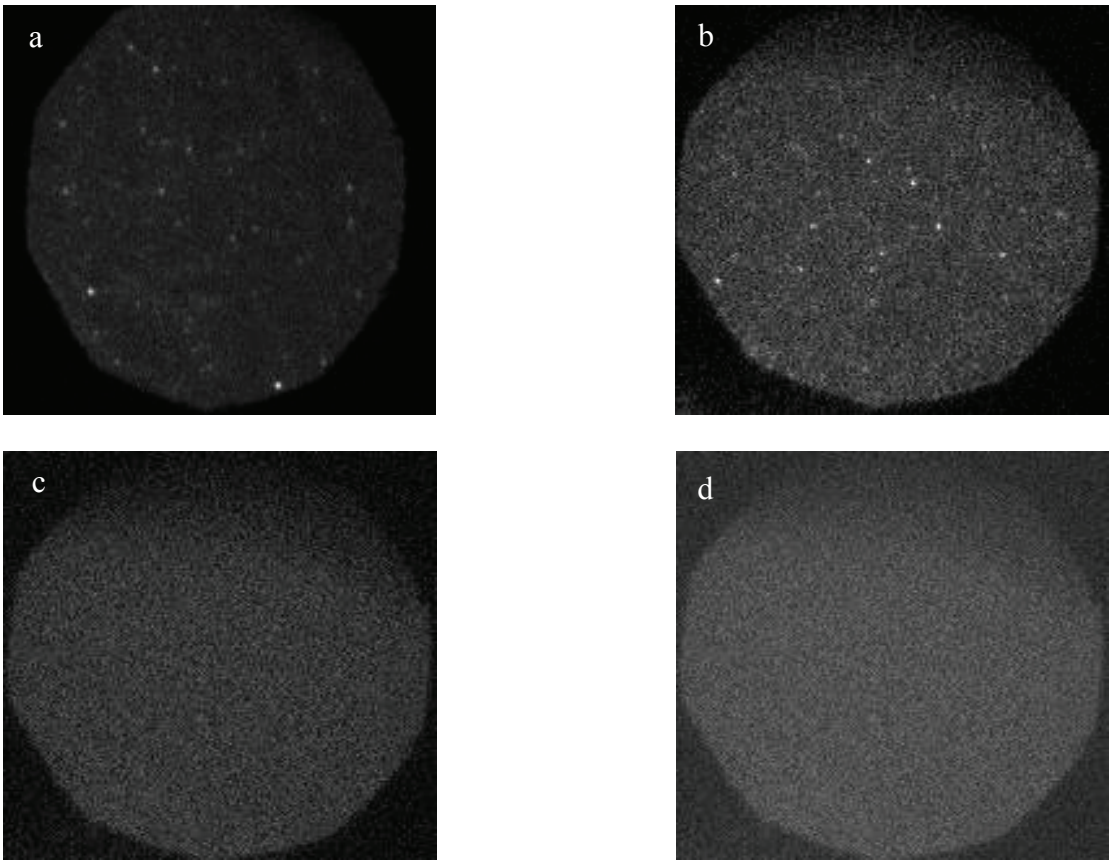

Figure 3-1.6: In this figure we can see images of a contaminated glass slide illuminated with a) 635 nm. b) 488 nm, and of an uncontaminated glass slide illuminated with c) 635 nm. d) 488 nm.

If the bleaching occurs in single step we are observing a single molecule. An example of this kind of measurements is shown in Figure 3-1.7. In the dual color imaging we have to measure the red and the blue/green channel simultaneously to verify the co-localization of two molecules. For this purpose some technical procedures are required to overlay both channels. As a result of a difference in the light path between the red and the blue/green beams after the tube lens (see Figure 2-2.4), the image channels became different in size and thereby different in the magnification.

Here I will describe the steps of cropping, resizing, and overlying the channels. For this particular case we used a stage ruler slide as follows:

1- Check the size and the position of every channel image with the stage ruler slide; In this step I made an image of the stage ruler slide in the transmission

illumination mode using an arc lamp to determine the size and position of every channel as shown in Figure 3-1.8.

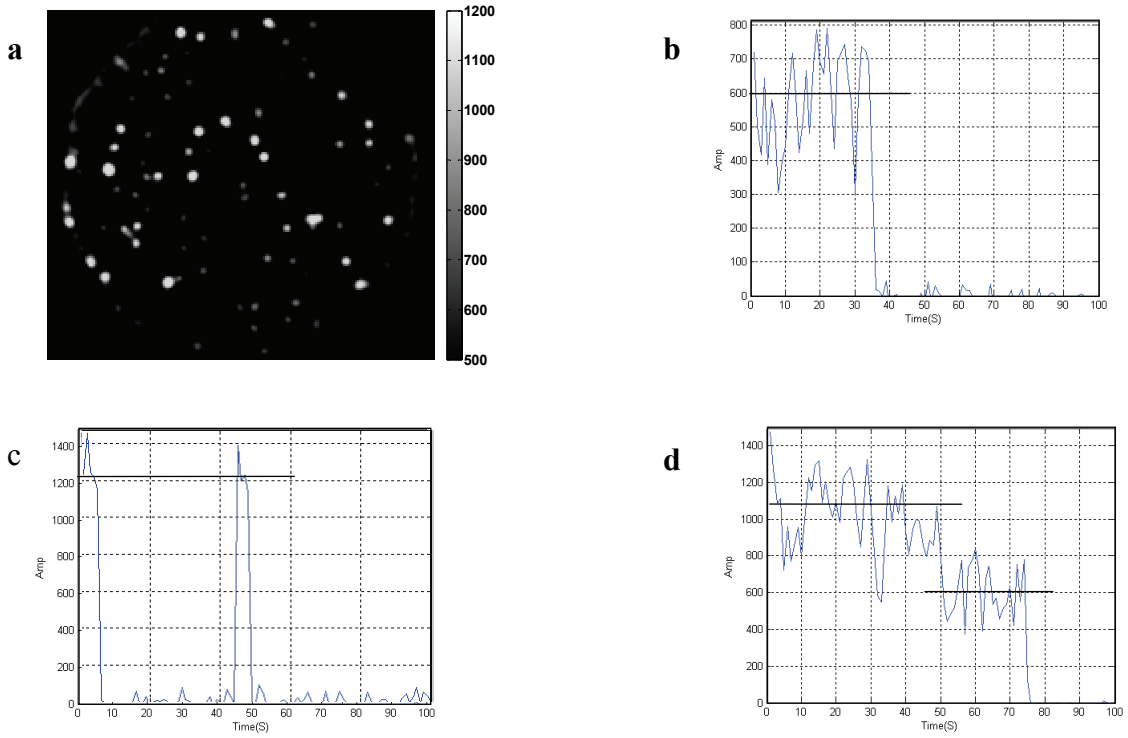

Figure 3-1.7: Photo-bleaching measurement for a streptavidin labeled with Alexa633. A time series of measurement performed with an excitation wavelength of 635nm and an exposer time of 2s for every frame. The images were treated with FFT band pass filter. a) Shows the image after treatment. The intensity of an area of 2x2 pixels was integrated for every spot at consecutive time steps. b) Shows single step decay indicating a single molecule, while c) shows single molecule, but in blinking state. d) Shows a two step decay, which indicates that we have imaged two molecules at the same time.

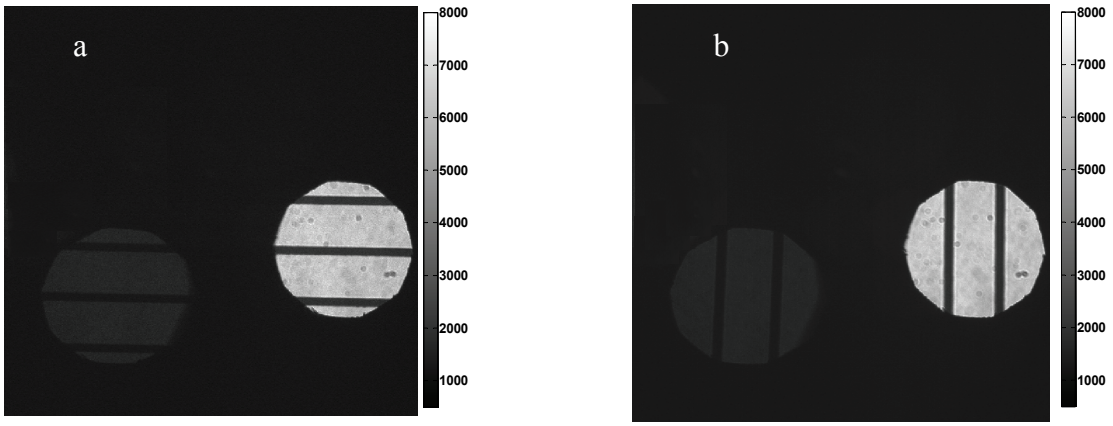

Figure 3-1.8: Images of the stage ruler slide, in a) horizontal and b) vertical orientation. The right channel displays red light and the left channel blue light.

2- After sample illumination the data were read and displayed using self-written matlab routines. The resulting images are shown in Figure 3-1.9.

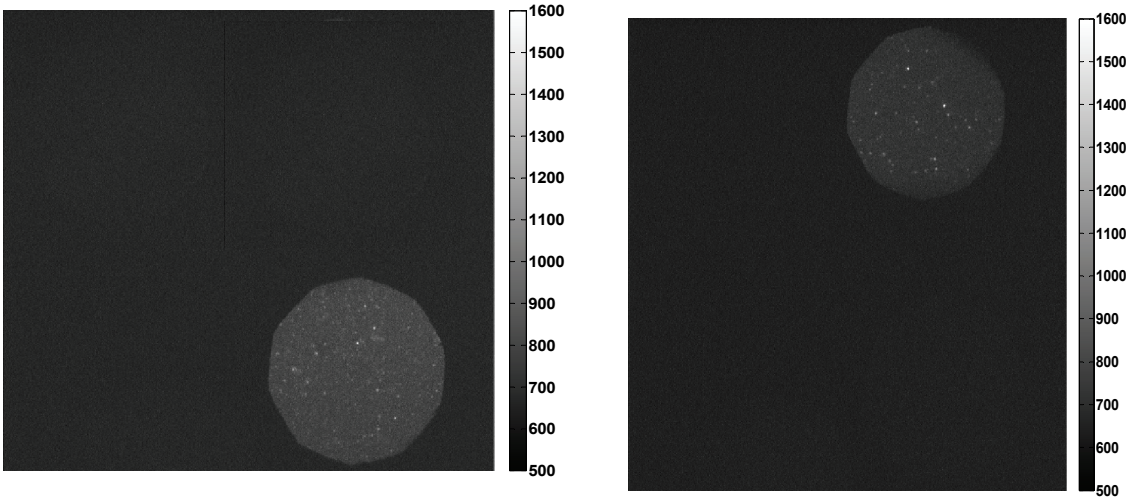

Figure 3-1.9: Images of surface tethered ribosomes the red channel (right image) and TMR the green channel (left image).

3- Cut (crop) the two channel images from the surrounding as shown in Figure 3-1.10 considering the channel dimensions as known from step one.

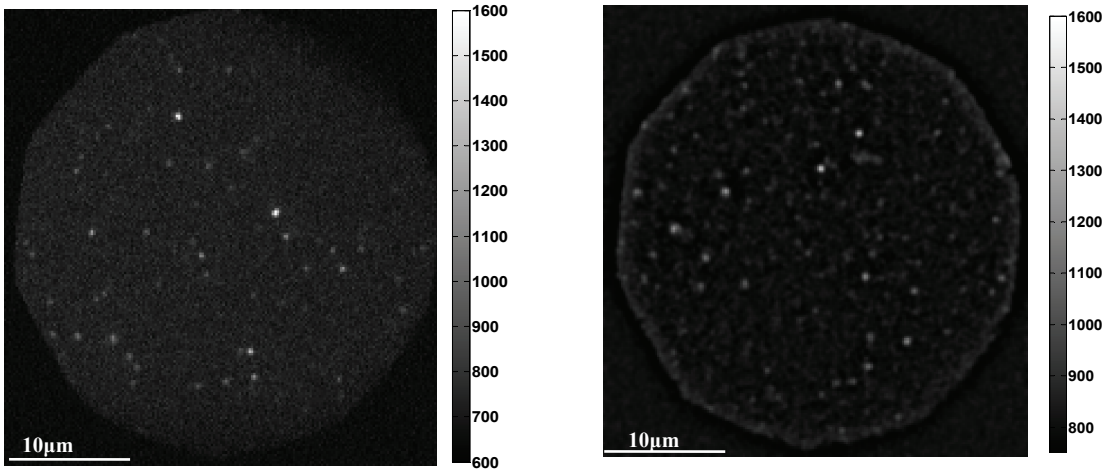

Figure 3-1.10: The left and right cropped images of images shown in Figure 3-1.9. The image size is 250 by 250 pixels. According to the wide field setup every pixel of the image corresponds to 0.156µm × 0.156 µm in real space (in case of camera binning 2x2).

4- Bringing both images to equal size.

5- A fast Fourier transformation (FFT) band pass filter is applied to flatten the background and to make fluorescence intensity spots easier to identify (*72*). Originally our CCD camera delivers images with a 14 bit depth if we divide the sensor area to 512 by 512 pixels (2x2 binning). This means that the resulting images experienced a conversion of incoming photon counts into 2^{14} (16384) different intensities (gray values) for each pixel. Typically further analysis included peak identification and peak intensity integration using integration masks for individual peaks of 2x2 pixels area sizes (larger peak structures have been excluded). In a similar way we can calculate the background surrounding every spot, an example of this treatment shown in Figure 3-1.11.

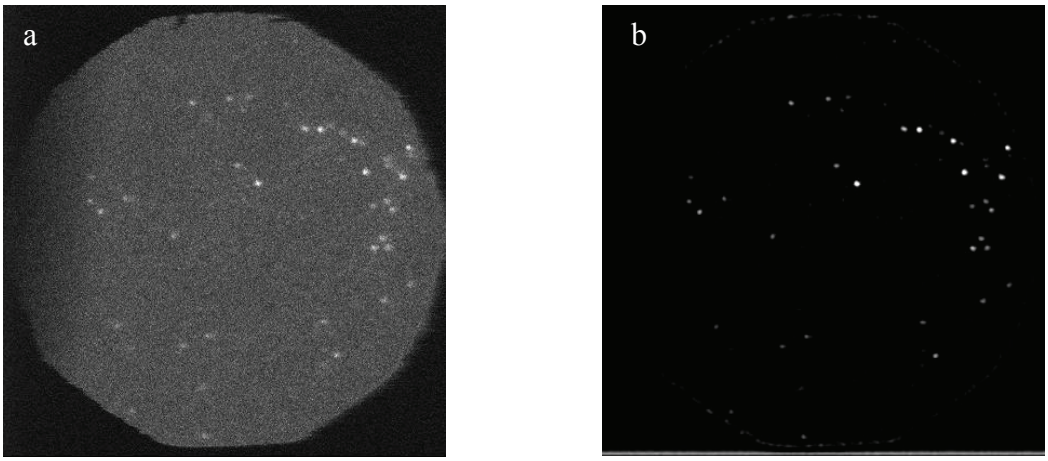

Figure 3-1.11: An example for a) untreated image, b) treated image (background subtraction and FFT band pass filtering).

6- For the co-localization purposes we converted the original images into 8 bit images and transformed the converted images into 3D matrix with RGB color mapping in the following order: the red channel, blue/green channel, and the sum of both. The resultant will be the overlay of both images. An example of this process is shown in Figure 3-1.12.

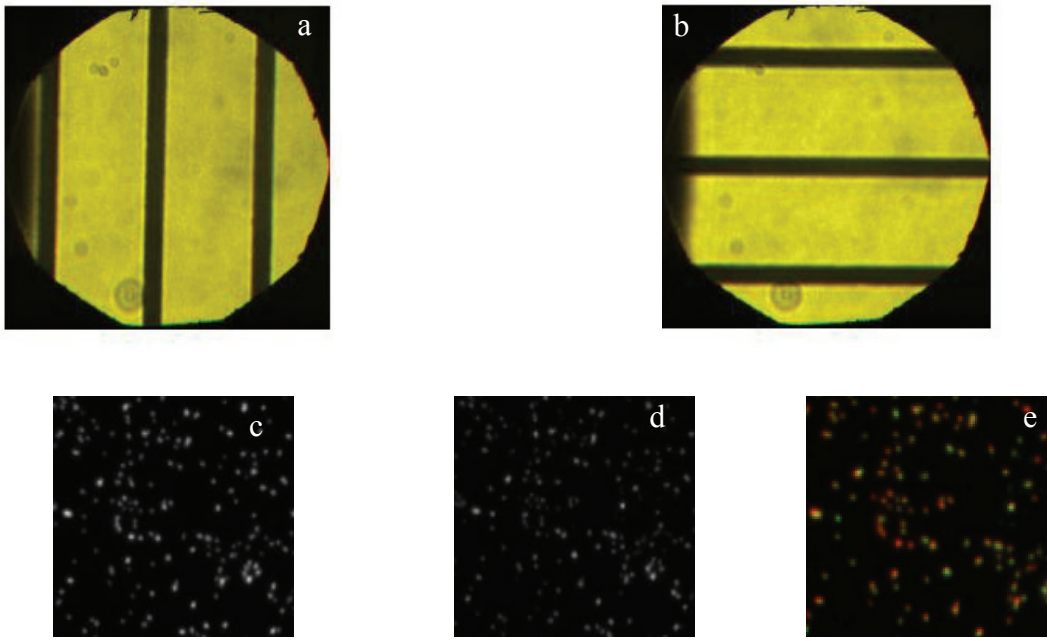

Figure 3-1.12: Examples from the overlaid images. For testing we overlaid a) the vertically oriented stage ruler slide, b) the horizontally oriented stage ruler slide (the ruler slide illuminated in transmission). c) Ribosomes labeled with Alexa 633. d) Synthesized protein labeled with BODIPY TMR. e) The overlaid images. The yellow spots refer to co-localized ribosomes and synthesized protein. The red spots represent ribosomes which have no co-localized BODIPY TMR. The green spots refer to the TMR which are not localized with ribosomes.

3-1.3 Calibrations for the confocal microscope

One goal of our studies was to analyze the structure in proteins in different folding states, by applying the FCS technique. For this purpose we employed a confocal microscope MicroTime 200 (*from PicoQuant GmbH, Berlin, Germany*). We measured the properties of the proteins by attaching dyes to the protein. In auto-correlation measurements we measured the particle diffusion through a confocal detection volume (for more details see Section 2-3). From measuring the diffusion time and the detection volume, as well as other parameters, one can calculate the diffusion coefficient and thereby the hydrodynamic radius (see Equation 3-1.2). The importance of the hydrodynamic radius is given by the fact that it is characterizing the size and thereby the folding state of the diffusing protein. In contrast to the diffusion coefficient the diffusion time is dependent on the detection volume. Hence if we know the detection volume (theoretically called confocal volume) and the diffusion time one can use the auto-

correlation equation (see Section 2-3) to calculate the proteins diffusion coefficient. So we performed calibration measurements to obtain the appropriate confocal volumes by using free dyes with known diffusion coefficient under the same conditions at which we measured the proteins.

The confocal volume is an opto-geometrical parameter strongly affected by the optical setup (pinhole size see section 2-3 and (*59*)). In addition to the pinhole size there are other parameters, such as the excitation power, the refractive index of the sample, the excitation wavelength, and the cover slide thickness which have to be considered (*18,19,50,65*). Typically in FCS measurements the sample concentration is very small (a few or fractions of nanomolar) and the optical and physical properties of the buffer solution is more less that of pure water.

But at high concentrations of ingredients in the buffer, such like GdnHCl, the viscosity and the refractive index will change. To correct for these effects we first measured free dyes with known diffusion properties. By measuring the auto-correlation of the free dye (an example is shown in Figure 3-1.13) we obtain the "real" value of the confocal detection volume and consider this value in the fitting model in order to get the correct value of the diffusion coefficient. Hence we can also use this volume for fitting the auto-correlation curves of the labeled proteins.

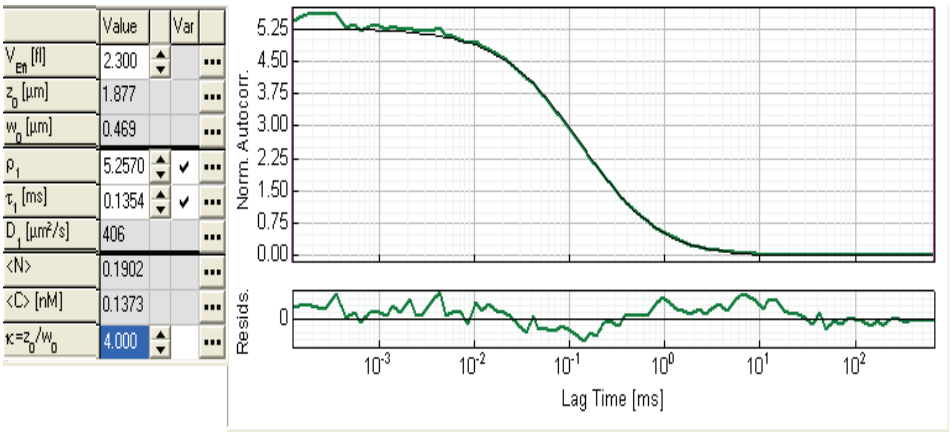

Figure 3-1.14: Auto-correlation curve (green line) of free diffusing Atto655. It is known from the optical setup that κ is in between 3 and 6 and V_{eff} is in between 1 and 3 femtoliter (fl). By adapting the κ value and V_{eff} we will get the fitting curve (black line) which gives the value of D, equal to the known value of Atto655 diffusion.

In general when time traces are measured with our single avalanche photo diodes a fast process (in the time regime of a few hundred ns) is visible in the auto-correlation, which

is called after-pulsing, as shown in Figure 3-1.14a. This after-pulsing creates additional artificial counts due to a feedback from the photon detector (*74*).

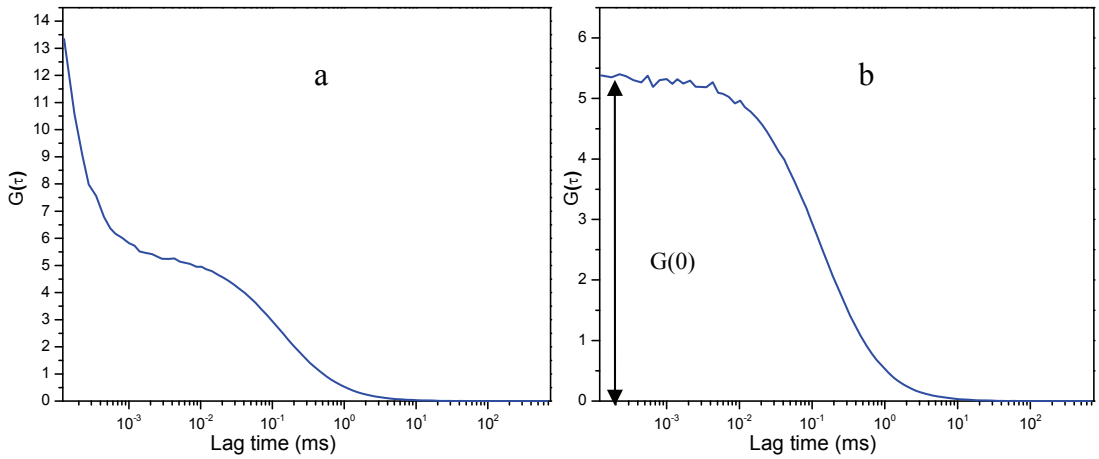

Figure 3-1.14: a) Auto-correlation curve for diffusing Atto 655. b) The removal of after-pulsing using the cross correlation.

To circumvent problems arising from these artifacts, we employed a 50/50 beam splitter dividing the signal and cross-correlated both channels (which is effectively still the auto-correlation of the original time trace, see Figure 3-1.14b).

We had also to deal with cases of dyes with unknown diffusion coefficient for which we employed another approach to determine the confocal volume. It is known from the literature that the detection volume in practice does not have a perfect uniform 3D-Gaussian shape. While the confocal volume is always defined theoretically as a 3D-Gaussian another notation of the effective volume (V_{eff}) was used see for example (*69*):

$$V_{con} = \left(\frac{1}{2}\right)^{\frac{3}{2}} V_{eff} \qquad 3\text{-}1.1$$

where the effective volume is given by (*9,23,24*):

$$V_{eff} = \frac{\langle N \rangle}{N_A C} \qquad 3\text{-}1.2$$

Here $N_A = 6.022 \times 10^{23}\ mol^{-1}$ is the Avogadro's number and $\langle N \rangle$ is the average number of diffusing particles through the detection volume (effective volume). According to Equation 3-1.2 one can plot a relation between the concentration and the average number. From the slope we can calculate the effective volume (*33,62,69*):

$$V_{eff} = \frac{slope}{N_A} \qquad 3\text{-}1.3$$

For this particular case we measured different particles and calculated the auto-correlation curve as shown in Figure 3-1.13b. <*N*> can be calculated from the auto-correlation by:

$$G(0) = \frac{1}{\langle N \rangle} \qquad 3\text{-}1.4$$

We measured the concentration of the employed dyes with an absorption-spectrometer (*UV-2401PC from SHIMADZU, Duisburg, Germany*). The obtained values of the detection volumes were employed for those cases where diffusion coefficients of the respective dyes were unknown. An example of these measurements is shown for Atto655 in Figure 3-1.15.

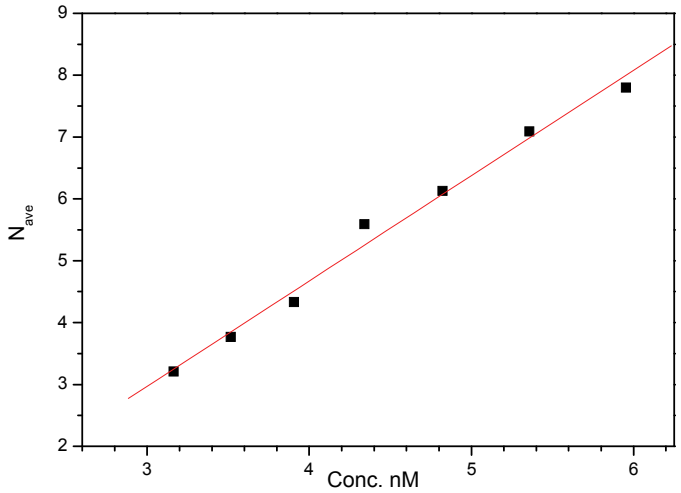

Figure 3-1.15: Dilution series of Atto655 in 50mM Na_2Co_3 buffer at pH7.4. The slope equals 0.99 nM^{-1} which leads to an effective volume: $V_{eff} = \frac{0.99 \times 10^{9}}{6.022 \times 10^{23}} = 1.6\ fl$

Another topic is the molecular brightness which gives the information of how many photons one can get out from one molecule in a certain time. In other words the molecular brightness defines the strength of the signal above the background (background counts are around 1-2 kHz). With diffusing molecules it is straightforward to obtain the molecular brightness from the time traces as measured with diffusion particles of known concentration (obtained from *G(0)*), see Figure 3-1.16.

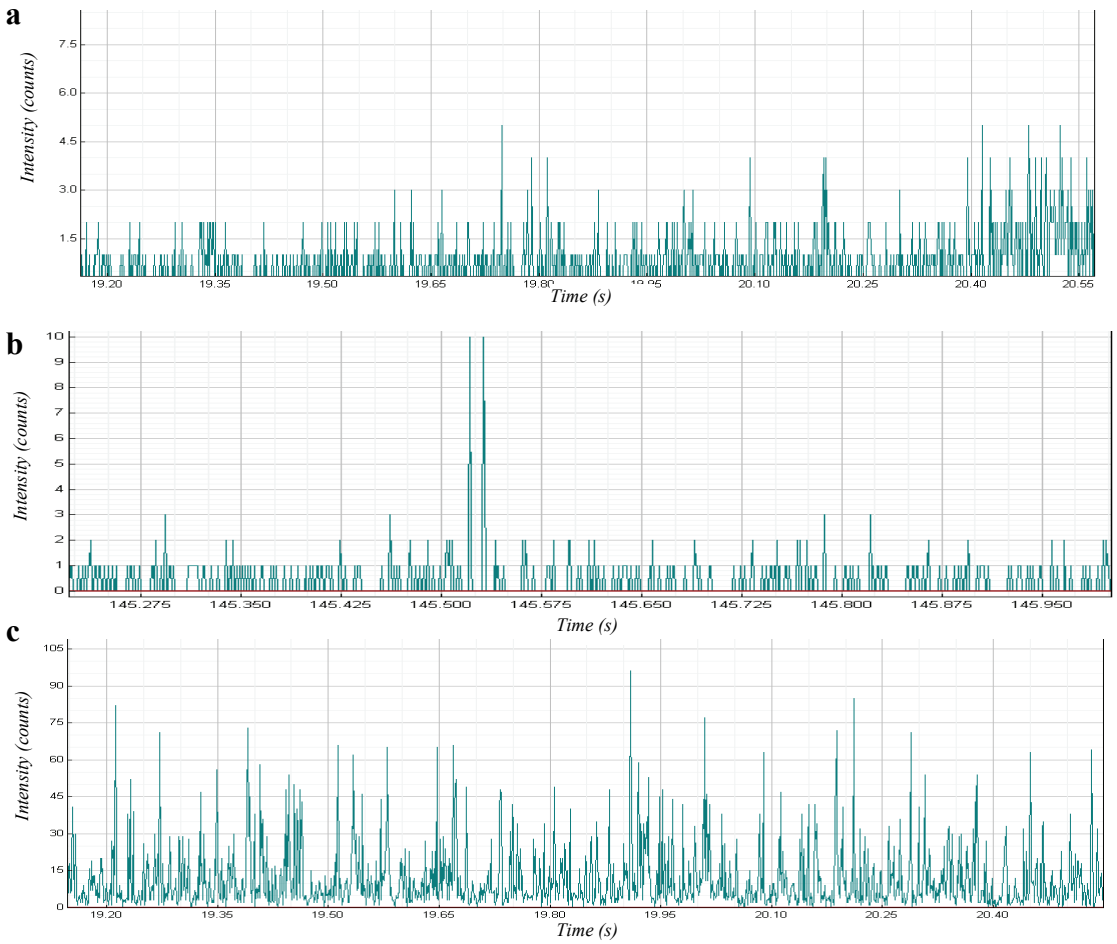

Figure 3-1.16: Time traces of only buffer (30mM Mops, 50 mM NaCl, 2 mM EDTA, pH 7.4) excited with 640nm and 470 nm, respectively (a, b). c) Atto655 in the same buffer with concentration of 400 pM excited with 640nm .

The molecular brightness is a meaningful property of a dye under defined excitation and emission conditions. It is a valuable measure to select appropriate dyes for single molecule studies and for the optimal excitation power (see Figure 3-1.17). Furthermore the known brightness is a helpful reference to check if the optical system is misaligned. From scanning the molecular brightness with different excitation powers one can identify the optical saturation point of the fluorophore. Optical saturation of fluorescent dyes may occur even at rather low excitation powers (only a few µW), as shown for the green fluorescence protein (GFP) in Figure 3-1.17. The photophysics of one and the same dye can already be altered upon attaching the dye to a target molecule (*18,64,65*).
In Figure 3.1-17 we displayed the molecular brightness for all fluorophores as a function of the excitation power.

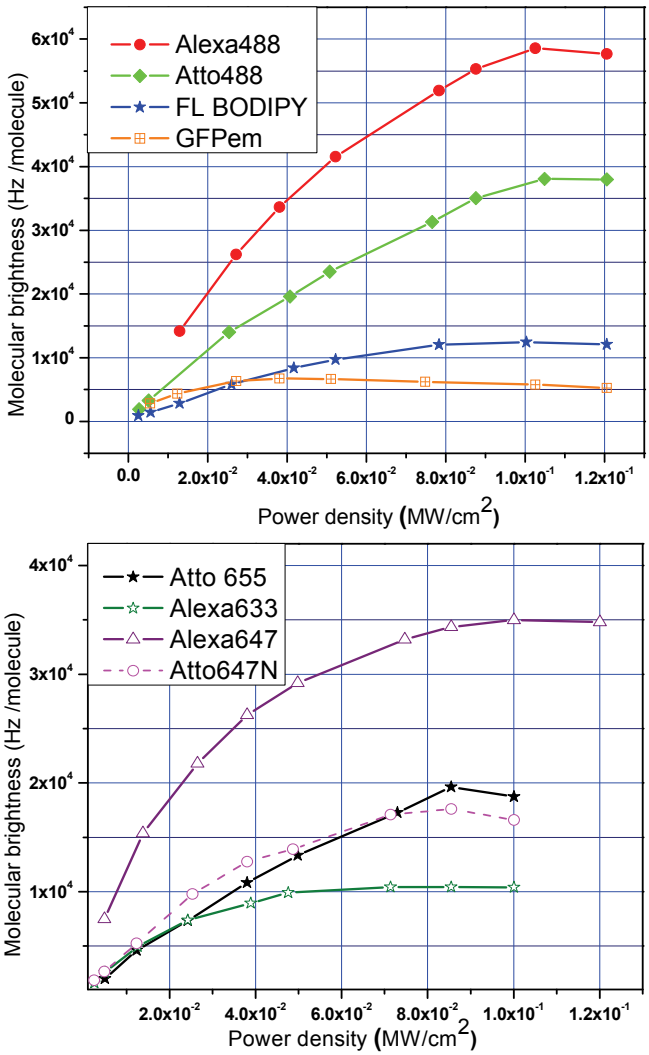

Figure 3-1.17: The molecular brightness of the used dyes as a function of the excitation power. It is demonstrated that an increasing the excitation power increases the brightness until a saturation point is reached and the molecular brightness stays more or less constant.

In Table 3.1.1 we summarized all diffusion coefficients and the hydrodynamic radii for biological molecules and for dyes. Hydrodynamic radii of biological particles were also measured by Dynamic Light Scattering (DLS) and agreed with the values from the literature (*64*). One of the most important tests which we had to perform regularly was to test the buffer for fluorescent impurities. Buffers typically represent a good medium for the growing of microorganisms which often contain also naturally fluorescent molecules.

Sample	Exp D ($\mu m^2/s$)	R_h (nm)	mass (kDa)
Atto655	407	-	0.845
Oregon-green 488	411	-	0.493
Alexa647	343 (a)	-	1.25(NHS)
Atto 488	369 (a)	-	0.981(NHS)
Alexa633	348 (a)	-	1.2(NHS)
Cy5	425	-	0.887
PGK	79	3	44
BLA	74	3.2	58.3

Table 3-1.1: Diffusion coefficients and the related hydrodynamic radii of different dyes and of proteins. The values are valid for a temperature of 25 °C. If not listed otherwise all the fluorophore functional groups are maleimides. The free fluorophores are measured in water. The protein hydrodynamic radii were measured in 30mM Mops,50 mM NaCl,2 mM EDTA, pH 7.4. (a) from personal communication with A.Loman and assured with the dilution series method. The values of diffusion coefficient of Atto655 and Oregon-green 488 are from (38,49,57) and for the Cy5 from(42). The hydrodynamic radius of PGK and BLA were measured using DLS(64).

Figure 3-1.18 shows an example of a contaminated MOPS buffer. The MOPS buffer we used for folding studies of alpha amylases and of PGK consist of 10mM MOP, 50mM NaCl, 2mM EDTA.

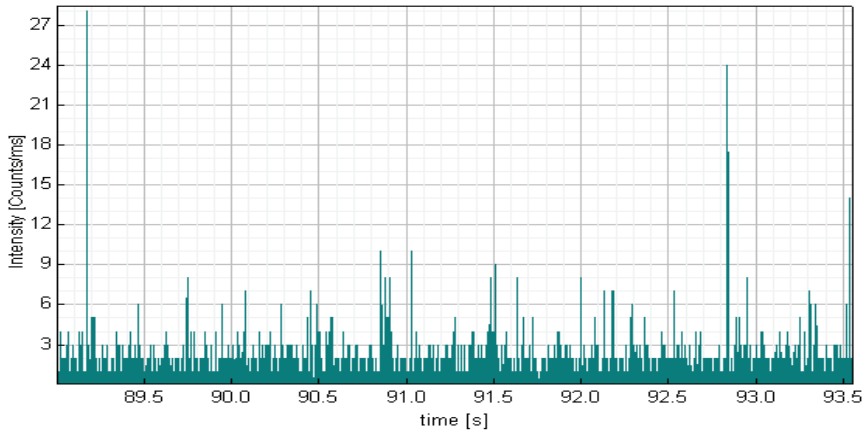

Figure 3-1.18: The time trace of a contaminated MOPS buffer.

By comparing this time trace with the time traces in Figure 3-1.16b, representing a clean buffer, we see the difference in background counts.

3-2 Monitoring protein synthesis and protein folding

In the last decade numerous studies have been performed on protein synthesis and its folding. These studies showed that protein folding and synthesis can differ substantially between *de novo* synthesized proteins and in vitro refolded proteins (*17,21,22*). In classical folding studies, formerly folded proteins need to be transferred into an unfolded state before the folding or refolding process can be studied. We saw in many cases that protein folding already takes place during the elongation of the nascent chain (co-translational folding) (*68*). Proteins can become fully folded and enzymatically active while they are still bounded to the ribosome through a C-terminal extension of about 31 amino acids, that spans the ribosomal channel (*37,39,40,44*). Significant differences have been observed between folding of *de novo* synthesized proteins and *in-vitro* refolding, with respect to folding rates, to the appearance of folding intermediates, and to yields (*12,22,25*). Therefore, one major goal is to understand how polypeptide chain elongation and folding are coupled. For this reason we performed two major sets of measurements. The first was to establish a kind of sample which allows us to observe the *de novo* synthesis and folding of a protein, in our case of the emerald green fluorescence protein ($GFP_{(em)}$). The $GFP_{(em)}$ has been synthesized from surface tethered ribosomes with release suppression of the produced protein as shown in Figure 3-2.1 (more details about the surface tethering in section 2-6).

As shown in Figure 3-2.2a, we can see the structure of the GFP as published in the protein data bank. The structure is a beta barrel (*3,55*) and the chromophore is located in the center of the barrel. Figure 3-2.2b shows the excitation and the emission spectra of the established GFP-S65T mutant. After the green fluorescence protein nascent chain has been synthesized, it starts to fold into the native state structure in which the chromophor is formed in steps as shown in Figure 3-2.2 c.

Hence GFP fluoresces only after the protein has been synthesized, and the chromophore has been formed. In this case we could not follow the protein folding by using fluorescence before the chromophore maturation. Therefore in a second approach we aimed to incorporate a dye into the nascent chain, in order to follow the synthesis and folding of the GFP.

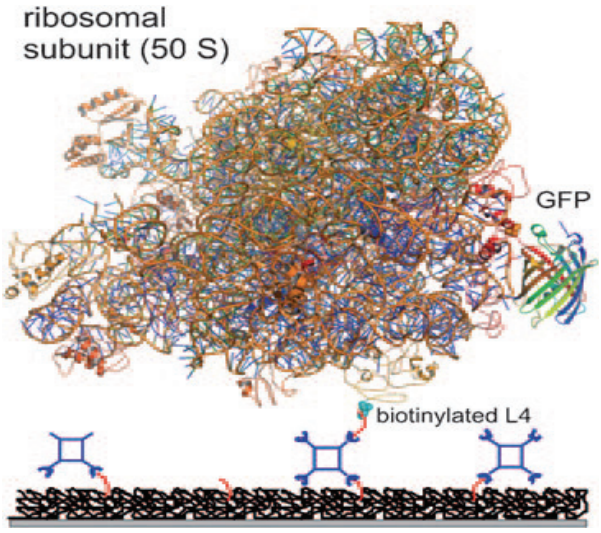

Figure 3-2.1 Schematic view of surface-tethered ribosomes (only the 50S subunit is shown, PDB code: 2AW4). The amino-functionalized cover slide is coated with a layer of poly (ethylene glycol) (PEG) that is biotinylated at low concentration(7). By the use of a streptavidin –biotin binding assay, fluorescently labeled ribosomes were linked to the surface through biotinylated ribosomal protein L4 (displayed molecules are not on scale).

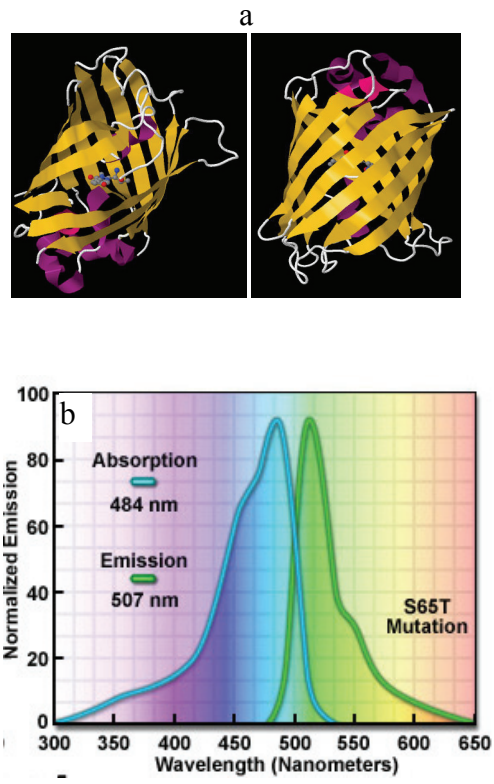

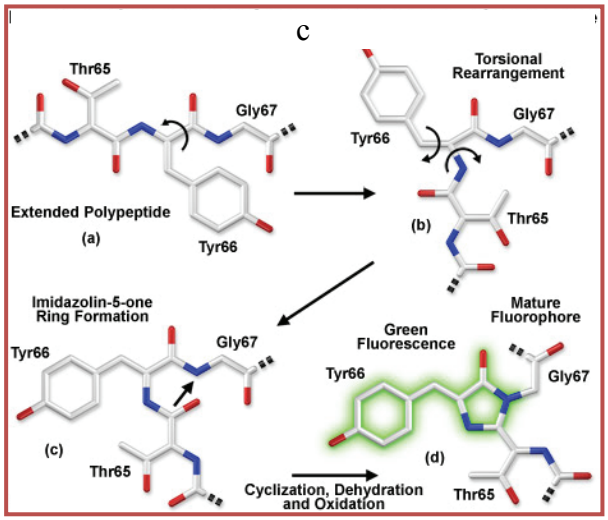

Figure 3-2.2: a) The GFP structure in a cartoon style from the protein data bank. b) The emission and absorption spectra of the GFP S65T. c) Steps of chromophore formation of the GFP(1).

For both goals we need surface tethered ribosomes, labeled with a red dye (we used Atto 655 or Alexa 633). For testing the functionality of the ribosomes, we let the ribosomes produce GFP *in-situ*. We elongate the construction by 31 amino acids (spanning the full ribosomal channel length). This extension ensures proper folding of the full length GFP outside the ribosomal channel (*20*). In the cell the proteins are typically released after the synthesis. In our case we suppress the release to keep the protein attached to the ribosome.

In both cases the surface tethered ribosomes were imaged using a wide field microscope (see section 2-1). The obtained images were processed and displayed using *ImageJ (from the National Institute for Health, Maryland, USA)* and by self written *Matlab* routines.

3-2.1 Biosynthesis of GFP molecules in a cell free expression system

We used ribosomes labeled with Atto655, and employed an emerald encoding plasmid GFP. In Figure 3-2.3a we can see the original image of labeled ribosomes. A clipping area of the ribosome image is shown in Figure 3-2.3b, while for the same area we cut out an area from the original GFP image, as shown in Figure 3-2.3c. Both images are overlaid in Figure 3-2.3d. The red spots are representing ribosomes, green spots are correspond to de novo synthesized GFPs. The yellow spots indicate the coexistence of single ribosomes and single GFP molecules, the later bound to their synthesizing ribosomes. In the Figure 3-2.3d we have a lot of ribosomes which did not produce a tethered GFP the (red spots), and therefore much less GFP molecules as compared to ribosomes. This can happen because the reaction mix ingredients did not ensure a higher synthesis productivity of the ribosomes. In our experiments we found that the number of produced GFP is around 10% of the total number of ribosomes. Also from the overlay we see that the majority of the produced GFP molecules appeared co-localized with the ribosomes. This tells us that these single GFP molecules are produced by related single ribosomes.

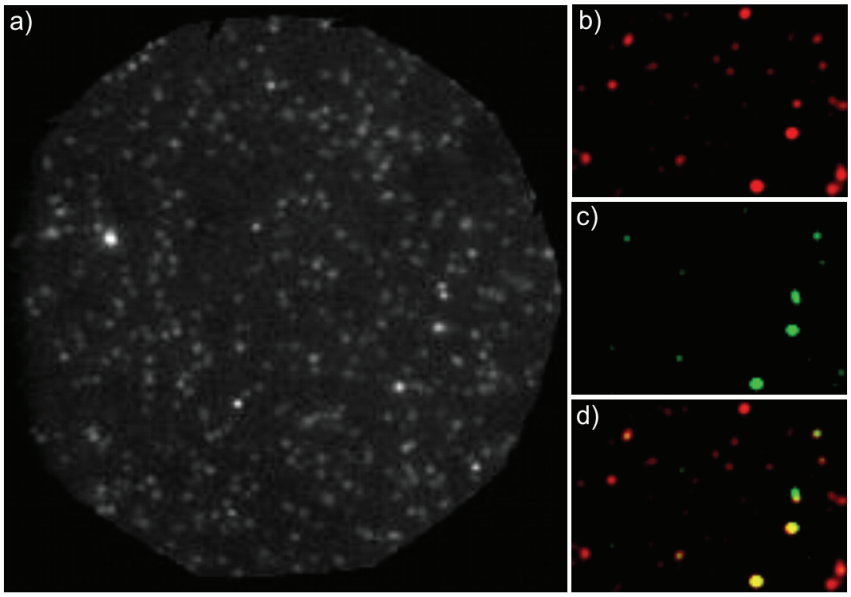

Figure 3-2.3: Fluorescence wide-field images from single surface-tethered ribosomes. a) A cropped area from the full screen of the red emission channel showing Atto 655-labeled ribosomes (exposure time of two seconds). Photo bleaching measurements demonstrated that the majority of individual peaks are related to single ribosomes. b) The red emission of ribosomes of a small selected area of image (a). c) For the same area, GFP fluorescence emission is shown, which was measured in the green channel after the transcription translation reaction had been running for 40 min at 25°C (laser excitation at 488 nm for 2 s). d) The overlay of the red (ribosomes) and the green (GFP) channel demonstrates that single surface-tethered ribosomes synthesized GFP molecules which become mature (i.e. fluorescent) while bound to the ribosome.

Time resolved measurements

With respect to the GFP synthesis and protein maturation process, we performed several measurements. I will show only a few. In the next series of measurements we prepared the surface tethered ribosomes, and injected 50 µl from the reaction buffer to start protein synthesis. Immediately after this we refocused the image with the red detection channel and started a time series of imaging by using blue excitation line (488 nm) over 120 images. The injection of the reaction buffer typically defocused the system slightly. For this particular case I employed a scheme, as shown in Flow chart 3-2.1, to take an image every 15 seconds, with exposer time of 2 seconds for every image. An important issue in our measurements was to achieve a proper focus stability. For testing this procedure we measured ribosomes labeled with Atto655 and refocused with the ZDC (more details in section 2-2.1) every 10 images. As shown in Figure 3-2.4a the intensity of individual spots exhibited a significant decrease (after approximately five images) which was due to focus lost.

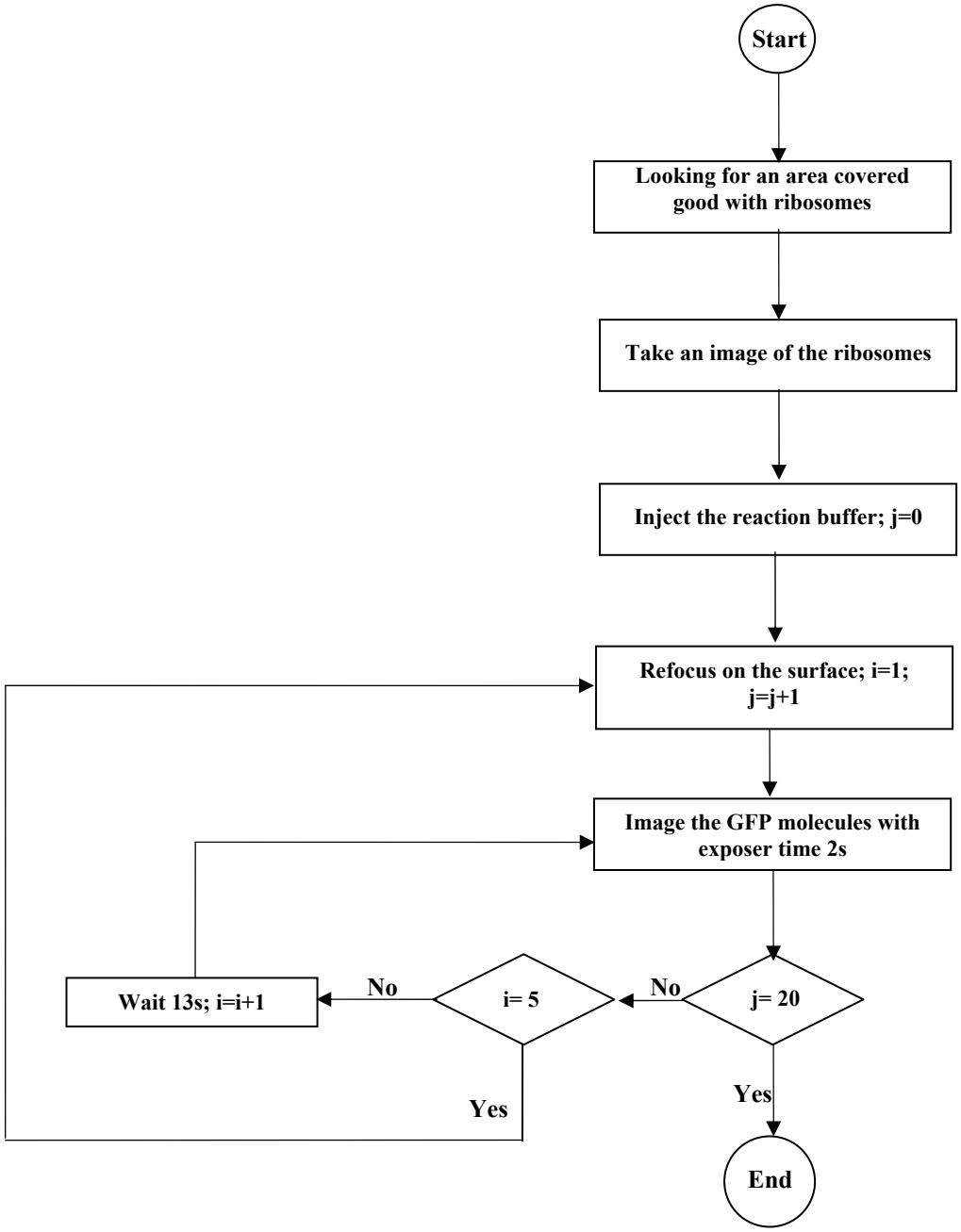

*Flowchart 2-2.1: A measuring scheme realized with the Cell M software (from Olympus, Hamburg Germany) which we used for the time series imaging. Here i is the number of images in the nested loop before the refocusing, j is the number of cycles, and i*j is the total number of images.*

Therefore we increased the frequency of refocusing (every 5 images) and obtained a more stable focus through the measurement as shown in Figure 3-2.4b.

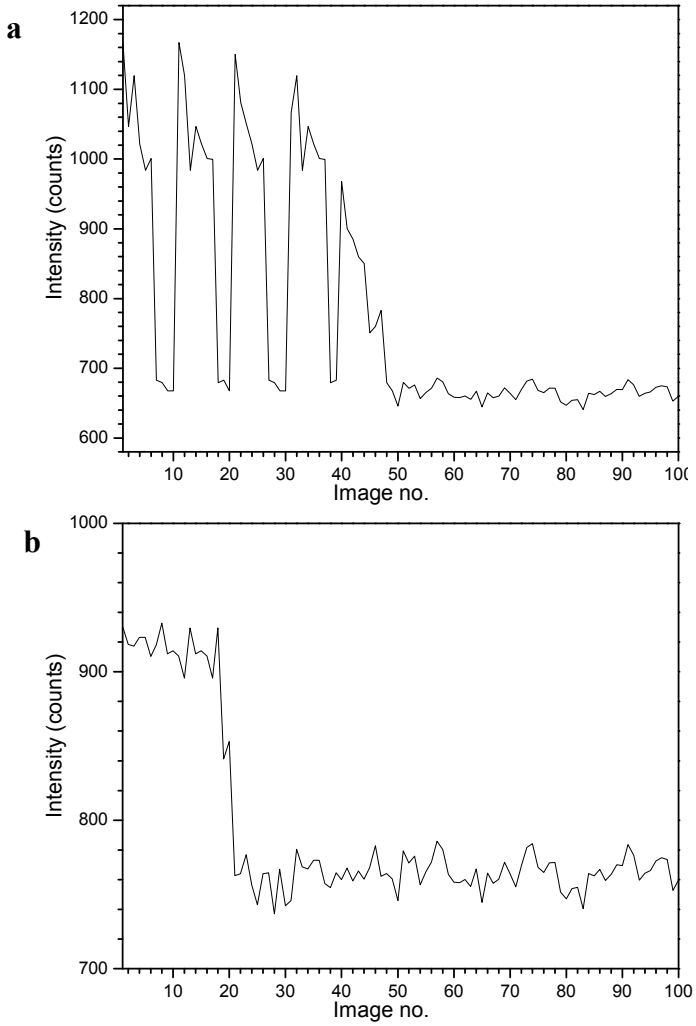

Figure 3-2.4: Focus stability. The intensity counts per image for a specific spot in a time series of measurements for: a) ribosomes labeled with Atto655. The exposer time was 2s with a pause of 13 s after every snapshot. Refocusing frequency was every 10 images. Clearly visible is a focus drift after about 6 images. b) BODIPY TMR with the same exposer and pause time, but the excitation was with 532nm and the refocusing was every 5 images. Here we do not have a focus drift as visible in (a). The intensities have been calculated for an area of 2x2 pixels.

Using further matlab routines, we localized and integrated spots over an area of 2x2 pixels after we treated the images with a FFT filter. Figure 3-2.5 shows some representative images. Passing through the whole time series, we obtained time traces of intensity values from synthesized GFP (co-localized with a ribosome) as shown in Figure 3-2.6.

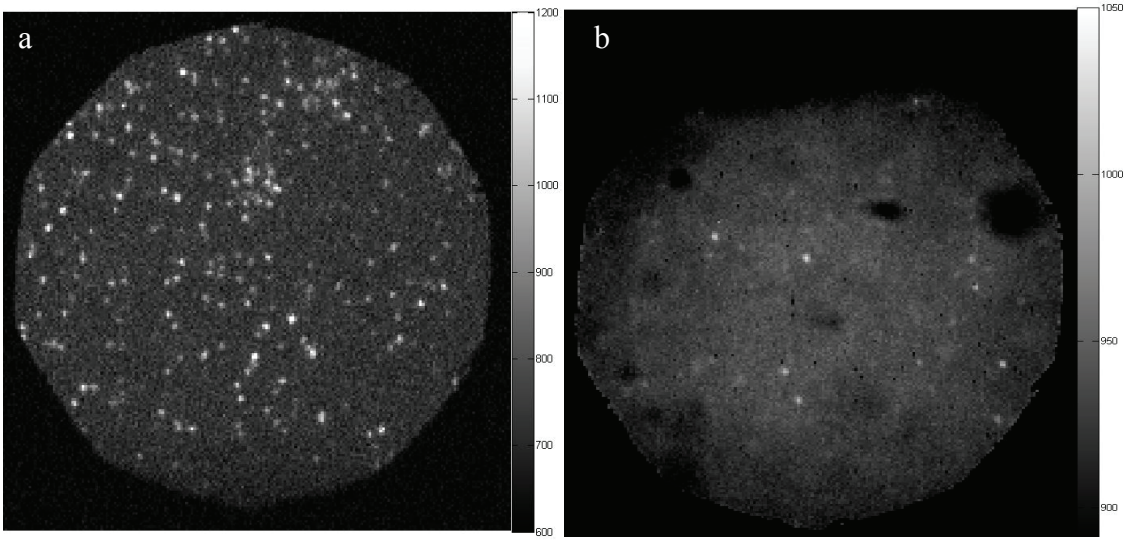

Figure 3-2.5: Fluorescence wide-field images from single surface-tethered ribosomes. a) The full screen of the red emission channel showing Atto655-labeled ribosomes. b) The full screen of the blue emission channel showing much less GFPem peaks through all the time series images.

In the most images (with an illumination time of 2 seconds) we obtained average background counts in the order of 920 counts. According to Poisson statistics the noise (*N*) or background fluctuation is given by the square root of the background counts (bc):

$$N = \sqrt{bc} = \sqrt{920} \approx 30 \qquad 3\text{-}2.1$$

This value is nicely reproduced in the data shown in Figures 3-2.6 While the signal or the peak intensity is typically around 90 counts the signal to noise ratio is:

$$\frac{S}{N} \approx 3 \qquad 3\text{-}2.2$$

From all measurements we extracted the appearance time of individual synthesized GFP molecules (see Figure 3-3.6 and 3-2.7a) and displayed the distribution of the appearance time as shown in Figure 3-2.7b.

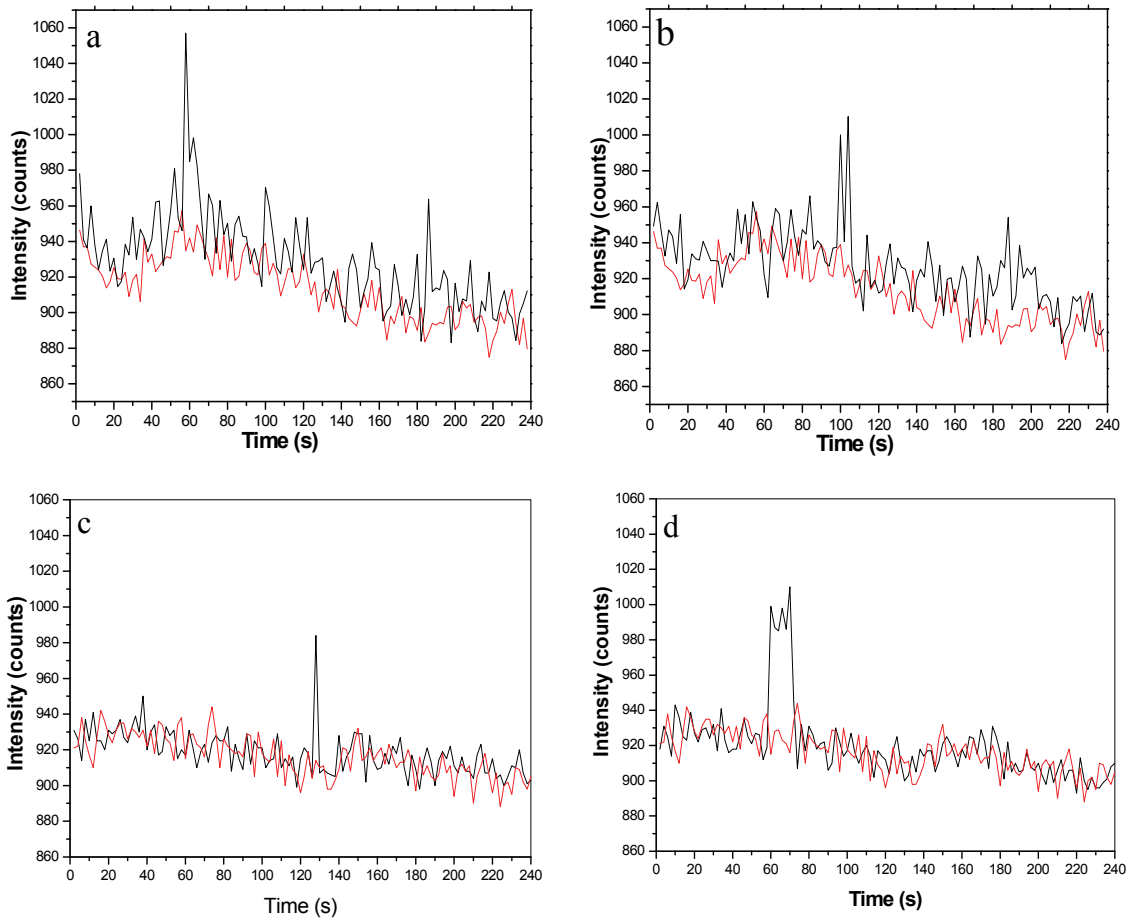

Figure 3-2.6: An example of integrated peak intensities (area of 2x2 pixels) are shown as a function of time, for fluorescent GFP molecules appearing after the initiation of biosynthesis. Fluorescence of individual GFP molecules can only be detected for a few consecutive exposures before photo-bleaching occurs (the black line). We can also see the background level (the red line). Through all the time series background is taken from, the surrounding pixels of the spot pixels (also an area of 2x2 pixels). a), b), c) and d) show GFP molecules formed at different times after the initiation of the biosynthesis with rather fast photo-bleaching.

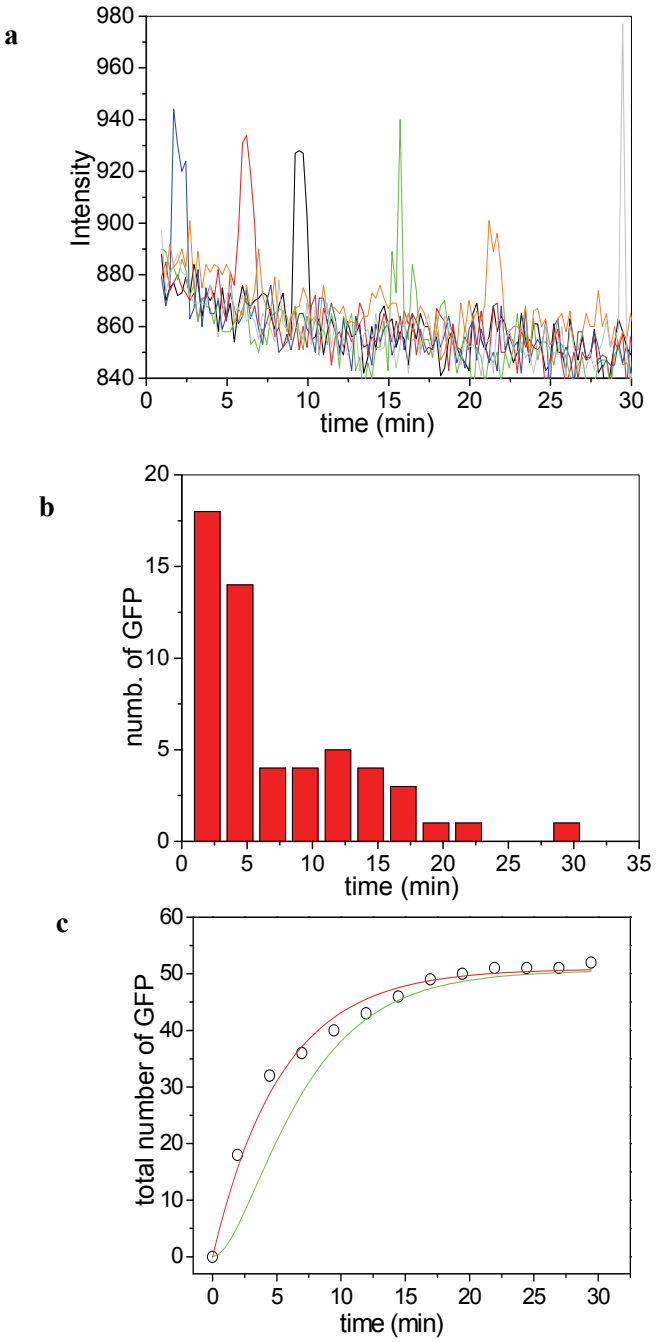

Figure 3-2.7 a) An example of integrated peak intensities (area of 2x2 pixels) are shown as a function of time for fluorescent GFP molecules appearing at different times after the initiation of biosynthesis. b) Histogram showing the number of de novo synthesized GFP molecules that appear in consecutive time intervals. After a dead time of about 40 s, a series of exposures was taken every 15 s at room temperature. The resulting appearance times of individual fluorescent GFP molecules, shown in chart (a), were binned into 2.5 min time slices. The data shown originate from five independent biosynthesis experiments. c) The time course of the total number of GFP molecules (o), and fittings with a mono exponential (red line) and a bi-exponential curve (green line). For details of the fitting procedure see the text.

To our surprise, GFP fluorescence shows up rather quickly, with a significant fraction within five minutes after initiating the polypeptide synthesis. According to the rather limited photo-stability of GFP, we observed in most cases photo-bleaching after a few exposures shown as in Figure 3-2.7a, and in some cases also photo blinking. The interpretation of our result has to consider at least three consecutive sub-processes. These processes include the polypeptide synthesis, protein folding, and chromophore formation, as part of the whole biosynthesis. Here we did not consider the transcription since it took place in the reaction buffer, before the sample was injected into the imaging chamber. For fitting the data we have to use a suitable model. We first tried a single exponential process:

$$N(t) = N_a[1 - \exp(-kt)] \qquad 3\text{-}2.3$$

Where N_a is the number of all *de novo* synthesized GFP molecules and k is the rate of GFP synthesis and maturation. Applying this model gave characteristic time constant ($1/k$) for the observed process of 5.3 min as shown in Figure 3-2.7c (the red line). This time is according to literature one of the fastest maturation times for a GFP mutant observed to date (*8,75*). Since we know that our process includes more than one step, we checked in addition an irreversible consecutive two-step process model (*31,53*).

$$S_1 \xrightarrow{k_1} S_2 \xrightarrow{k_2} S_3$$

Applying this model on the synthesis of the GFP, we are dealing with two transitions and their respective transfer rates (k_1, k_2). The first represents the polypeptide chain synthesis and the folding process (k_1), the second is referred to the chromophore formation (k_2). We have two cases, the first is $k_1=k_2$, which means that the synthesis and folding rate equal to the chromophore formation rate. This hypothesis is not valid because these rates are completely different due to the conditions which control the chromophore formation (*8,58,66,75*). So in our case we have to use the second hypothesis, the case of $k_1 \neq k_2$. Hence the number of the proteins which are matured and have a formed chromophor will be *N(t)* which is given by:

$$N(t) = \frac{k_2 N_a}{k_1 - k_2}\exp(-k_1 t) + \left(\frac{-k_2 N_a}{k_1 - k_2} - N_a\right)\exp(-k_2 t) + N_a \qquad 3\text{-}2.4$$

Fitting this function to the experimental data points yields 0.1 min for $1/k_1$ and 5.2 min for $1/k_2$. As we see the first time component is very fast comparing to the second component. Protein synthesis and protein folding must be rather fast (probably faster than one minute). In a consecutive two-step process, a much longer first process for protein folding (e.g. with $1/k_1 \approx 2$ min) and subsequent chromophore formation shows a distinct deviation from the experimental data points as shown in Figure 3-2.7c (green line) which was calculated with fixed values for $1/k_1$=2.0 min and $1/k_2$=5.3 min. Typical maturation times of other GFP mutants of the S65T type range from 15 to 45 min, whereas wild-type GFP shows even longer maturation times on the order of 2 h (*28,67,75*). The fast chromophore formation for GFP is important for its use in kinetic experiments in cells (*56,73*).

3-2.2 Attempts to establish a FRET pair to monitor co-translational folding

In the case of dye incorporation my colleague introduced additional 30-40 amino acids in front of the GFP sequence and incorporated a BODIPY TMR linked to a lysine by using the amber-codon (*6*). After these 30-40 amino acids there is a sequence of 6 histidines as shown in the schematic draw of the construction in Figure 3-2.8. Until this step the no histidines appear in the sequence and used reaction buffer does not contain any histidine. When the synthesis is reaching the histedines it will stop synthesizing, but the polypeptide chain will remain at the ribosome.

Figure 3-2.8: A schematic draw of the GFP construct to be used for experiments discussed in detail in text. This construction was prepared by my colleague Dr. A. Katranidis.

This synthesized polypeptide chain with leading BODIPY-TMR labeled lysine will expose the label at the exit of the ribosomal channel. To continue the reaction we have to inject a reaction buffer which contains histidines. Concomitant with the injection we started to record a time series of subsequent images. One other important issue is the label attached to the ribosome which has to be labeled site-specifically near the tunnel

exit to achieve FRET. We labeled our ribosomes with Alexa633 (the FRET partner of the TMR) at the end of the ribosomal channel.

The data shown in Figure 3-2.9 represent measurement done as described before. To analyze the images we must co-localize the peaks to verify that nascent chain which incorporated the dye was synthesized by its respective surface tethered ribosome. The images were treated using our routines as described in Section 3-1.2. and the resulting overlaid images are shown in Figure 3-2.9e.

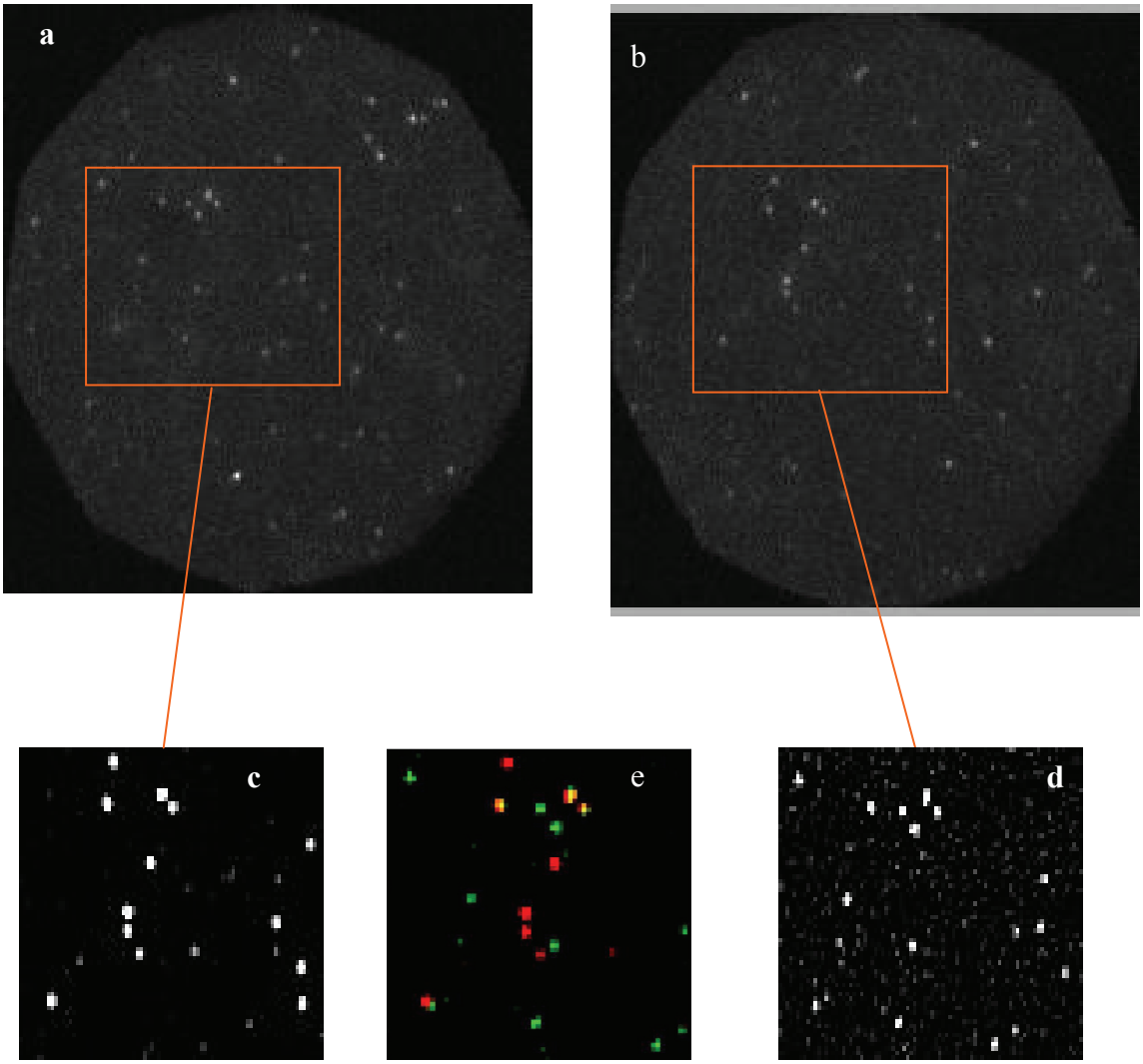

Figure 3-2.9: Fluorescence wide-field images from single surface-tethered ribosomes. a) The red emission channel for ribosomes. b) BODIPY TMR fluorescence emission is shown, which was measured in the green channel, after the transcription translation reaction has been running for 40 min at 25°C in a histidine free medium. For both original ribosomes and BODIPY TMR images an area from the original image was cropped and treated as usual with our subroutines. Shown in c, d. e) yellow peaks indicate the coexistence of single ribosomes and single BODIPY TMR molecules bound to their synthesizing ribosomes.

In this figure we can see that very little labeled polypeptide chains are co-localized with ribosomes, which yielded yellow peaks. The non co-localized TMR (green peak) may result either from labeled polypeptide chains produced by unlabeled ribosomes or from aminoacyl-tRNA constructs which also carry the BODIPY TMR and may stick unspecifically to the surface. Furthermore we cannot rule out ribosomes which are non-functional and will not synthesize polypeptide chains. In this case we will observe only red spots.

Results from time-series measurements in terms of integrated peak intensities as a function of time are shown in Figure 3-2.10. In this figure we show only intensities of the BODIPY-TMR (donor) channel, because in these particular measurements we had problems with secondary images of the blue channel falling on the area of the red channel (which we later solved by using more appropriate emission filters). Therefore an analysis in terms of FRET was not possible with the data because the acceptor channel was contaminated with donor counts. The only aspect which was analyzed with this data is related to question whether we observe really single molecules or not. Since the shown peak intensities drop down in one single step (Fig. 3-2.10a,b,c) we can be sure to deal with single molecules. Furthermore we have samples of molecules which start to fluoresce slightly retarded after the initial starting time (time zero), while we expected to see fluorescence directly starting at the time zero. A possible explanation for this behavior might be a quenching process of the donor at the "starting position" before we restarted the synthesis again with histidine rich medium. In other cases we observed a donor fluorescence appearing much later (Fig. 3-2.10d,e). Here fluorescence blinking of the respective fluorophores is the most probable explanation for this phenomenon. Considering our initial experimental approach with two dyes having an assumed inter-dye distance in the order of the Förster radius of our pair (for the BODIPY-TMR Alex633 pair R_o is approximately 50 Å) we cannot rule out that intensity fluctuations as visible in all intensity traces of Fig. 3-2.10 might be due to energy transfer to the acceptor. Only further measurements with well aligned mirrors can give us the complete information to find out whether and to which extend FRET takes places in theses samples.

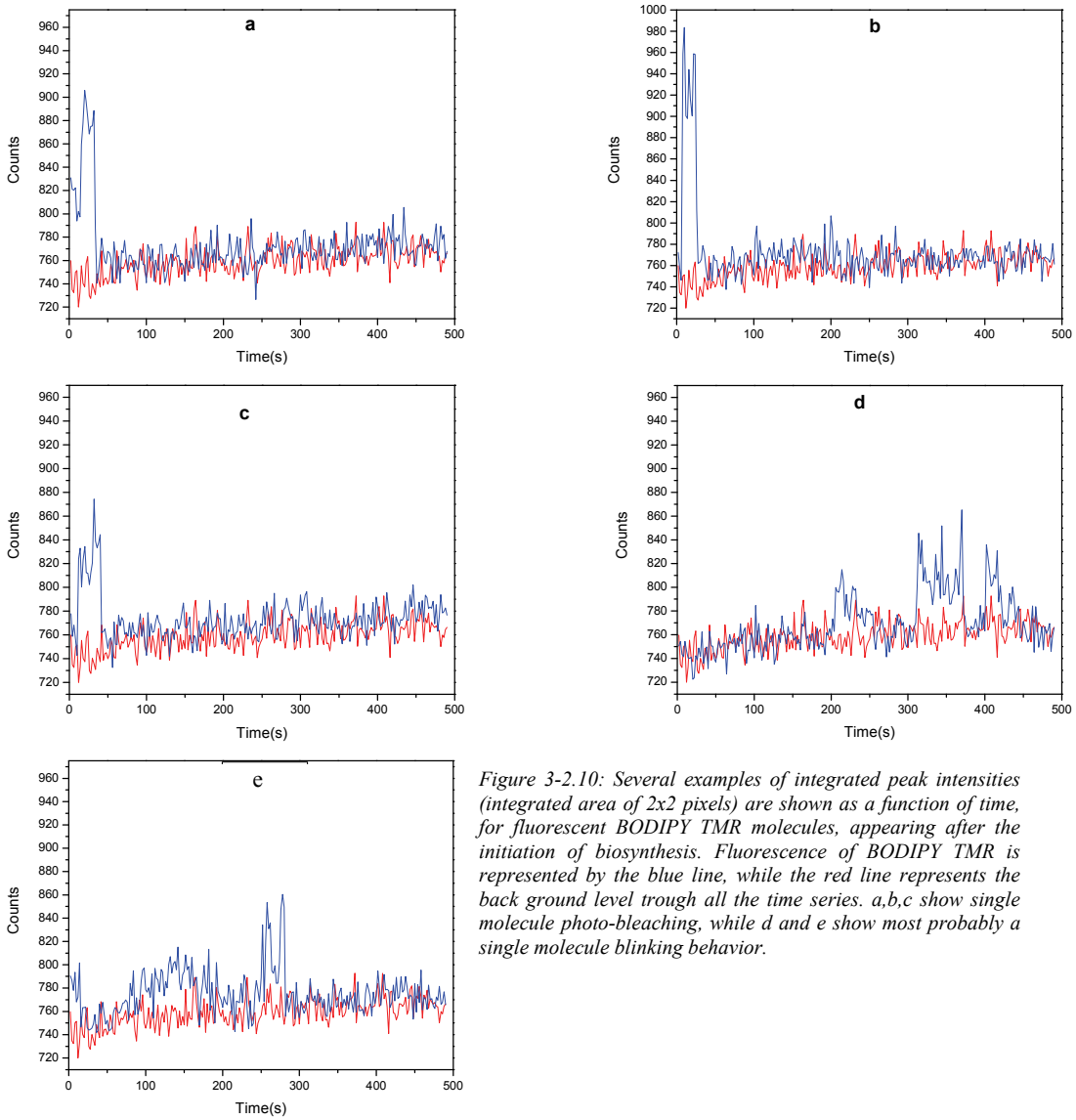

Figure 3-2.10: Several examples of integrated peak intensities (integrated area of 2x2 pixels) are shown as a function of time, for fluorescent BODIPY TMR molecules, appearing after the initiation of biosynthesis. Fluorescence of BODIPY TMR is represented by the blue line, while the red line represents the back ground level trough all the time series. a,b,c show single molecule photo-bleaching, while d and e show most probably a single molecule blinking behavior.

3-3 Observing proteins as single molecules encapsulated in surface-tethered polymeric nanocontainer

A key technique for immobilizing proteins (water soluble) is encapsulation. In a typical single-molecule study using a confocal microscope, the detection volume becomes very small. As a consequence the detection time is limited by the diffusion time which is in the range of fractions of milliseconds to a few milliseconds, according

to the hydrodynamic radius of the diffusing particle. To achieve longer observation times, we have to immobilize the protein. Optical trapping techniques did not give satisfactory results on the single molecule level due to the low polarizabilities of single molecules. One requirement for almost all single-molecules studies with immobilized proteins is to reduce, as much as possible, interactions of the protein with the surfaces of the enclosing cavity used for immobilization. In protein folding or during enzymatic action cycles, perturbing protein-surface interactions might significantly alter the polypeptide structure and dynamics. This can give rise to artifacts in the obtained results (*47*). For investigating and analyzing a nanocontainer encapsulated protein, this container must be stable, and durable throughout the chemical and physical changes. It is known from the literature that capsules which are formed from the ABA tri-block copolymers have this desired stability (*15,46*). In addition a limiting factor for protein folding studies is that the vesicles must be permeable to the unfolding conditions (heat or chemicals). Fortunately the membrane of our vesicles is permeable to the GdnHCl (*60*), which we were used as a chemical denaturant. The ABA co-polymer consists of a large hydrophobic block B (PDMS, with 60 dimethylsiloxane units) and two shorter hydrophilic blocks A (PMOXA, with 20 methyloxazoline units; ABA: PMOXA20-PDMS60-PMOXA20).

For the polymerosome preparation we mixed a 3.6 mg of triblock copolymer with a 0.4 mg of biotinylated triblock copolymer and dissolved all of them in 1ml chloroform. By rotating the solution in a tube permanently under a nitrogen atmosphere a dried film has been formed. By adding to this film 0.8 ml of the buffer and sonication for 1 min polymerosomes were formed. For encapsulating the protein inside the polymerosomes 200 µl of a protein was added to the buffer. Thereafter the mixture was stirred at room temperature (the protein solution concentration and the stirring time are depending on the protein). The resulting suspension was subsequently extruded approximately 20 times through a polycarbonate membrane (diameter 100 nm) using a Lipofast-basic extruder (*Avestin Europe GmbH, Mannheim, Germany*). For purification and removing the non-capsulated protein a 30 cm long Sephadex G75 column was added. While about 10% from the triblock copolymer is biotinylated we can use our tethering protocol to immobilize the polymerosomes to the treated glass surface (for more details see section 2-6).

3-3.1 Protein encapsulation inside polymerosomes

In order to determine the number of encapsulated proteins per polymerosome we performed photo-bleaching measurements (*11,13,54*). For this purpose we tethered polymerosomes. With encapsulated PGK labeled with Atto655 (label ratio 0.6 dyes per protein, see Section 2.7) and tethered them to a glass slide.

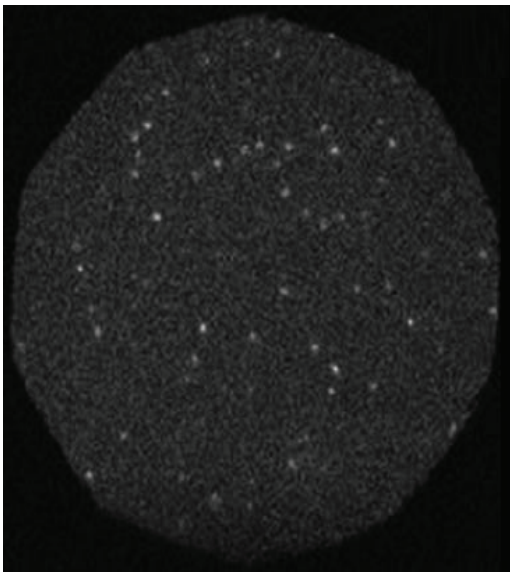

Figure 3-3.1 Wide-field fluorescence image of surface tethered polymerosomes containing Atto655-labeled PGK. The excitation wavelength is 640nm, the exposer time was 2s.

We took 100 subsequent images with exposer times of 2s (Figure 3-3.1) resulting in 200s of total illumination time. This led to a pronounced photo-bleaching of fluorophores as bound to the encapsulated proteins. The number of encapsulated proteins per polymerosomes can be determined by the number of discrete photo-bleaching steps, visible by a sharp decline in fluorescence intensity. Typical examples of the time course of step-wise decays (photo-bleaching) are shown in Figure 3-3.2.

In principle the process of protein encapsulation into vesicles follows Poisson statistics, yielding a probability distribution of numbers of proteins per vesicle (*11,54*). We observed that approximately 80% of all imaged polymerosomes exhibited one-step bleaching, and 20% exhibited two-step bleaching. According to the distribution, we also expected to have a considerable fraction of polymerosomes with unlabeled proteins or polymerosomes without protein, but these will not show up in a fluorescence image. Hence, polymerosomes as prepared with our protocol are indeed suitable for single-molecule encapsulation, and for single molecule detection.

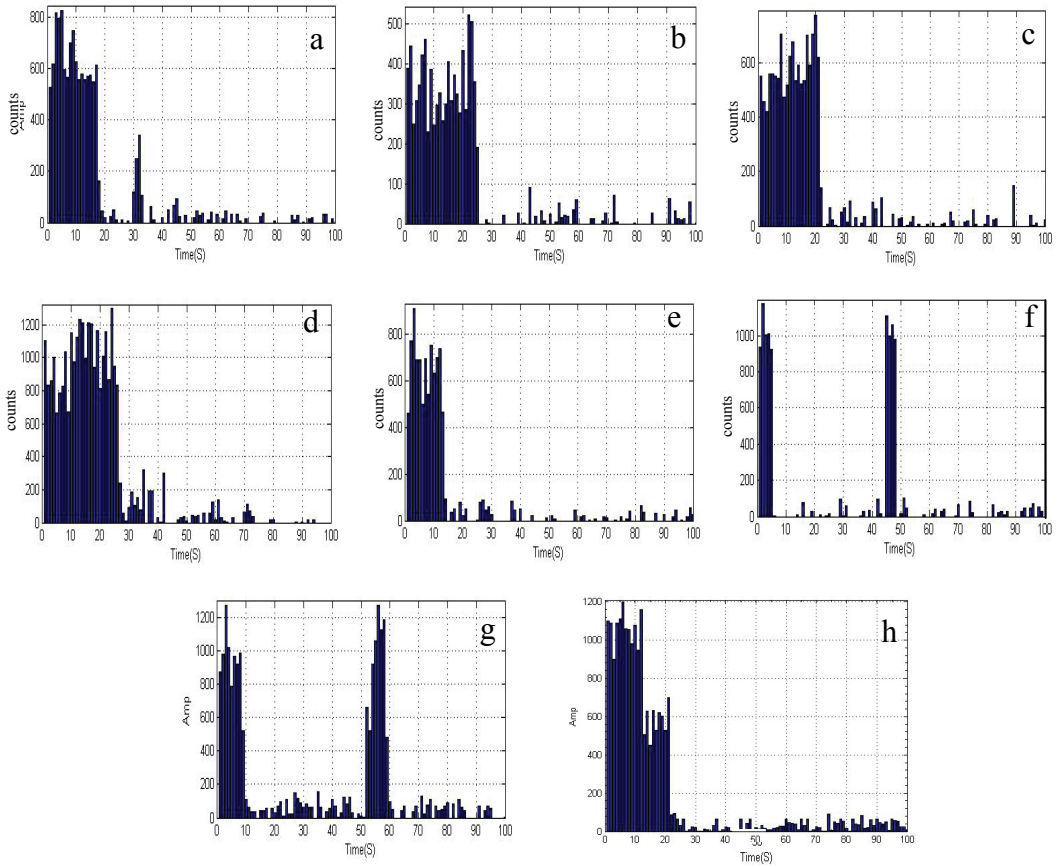

Figure 3-3.2 Time course of photo-bleaching experiments. a, b, c, d and e) show a single step decay which gives evidence for single molecules encapsulation. f and g) also shows a single molecule, but blinking happens. h) Shows a clear two step decay, which means that this vesicle contains two fluorophores. For the counts we localized and integrated the intensity over peak area (2x2 pixels) through the entire time course for every spot, see Figure 3-3.1.

3-3.2 Characterizing folded and unfolded states of encapsulated proteins

For reasonable protein-folding/unfolding studies, the protein must be free of unwanted interactions with the surface of the polymerosomes. The proteins should be able to diffuse freely inside the polymerosomes. So we employed fluorescence anisotropy measurements which provide valuable information in this respect. Using the confocal microscope equipped with a polarization beam splitter cube one can measure the rotational freedom of dyes as bounded to the protein. Hence we can calculate the anisotropy. Anisotropy thereby allows us to detect potentially perturbing interactions of the proteins with the vesicle surfaces. Figure 3-3.3 and Table 3-3.1 show the time-

resolved and the steady-state anisotropy measurements for the unbound dyes, for dyes bound to native proteins, and for dyes bound to unfolded proteins. They are slightly different but all of them are rather small. The results indicate a high degree of rotational freedom for all samples. In addition we measured an amphiphilic lipid (DOPE labeled with Atto655) which was embedded in the polymer matrix and therefore exhibited a rather high anisotropy. As expected, and in contrast to the encapsulated molecules, DOPE is rather immobile. Time-resolved fluorescence anisotropy decays were measured on a MicroTime 200 confocal microscope.

Sample	**Native Buffer**		**5M GdnHCl buffer**	
	In solution	encapsulated	In solution	encapsulated
Unbound Atto 655	0.03 ±0.002	0.04± 0.01	0.05± 0.002	-
PGK/BLA -Atto655	0.12 ±0.03	0.13± 0.05	0.09± 0.05	0.1 ±0.05
DOPE-Atto655	-	0.27± 0.02	-	-

Table 3-3.1 Anisotropy values as obtained from steady-state measurements.

For this purpose a droplet of a protein solution or a solution of protein encapsulated in polymerosomes (both at approximately 400 pM of sample) was deposited on the surface of a cover slide. The fluorophore was exited with a 640 nm laser line and we focused the beam approximately 20 μm inside the buffer solution above the surface of the cover slide. Time-resolved anisotropy decays were calculated and displayed as shown in Figure 3-3.3. In this figure we can see a fast and almost complete decay of the anisotropy within 2 ns for an unbounded Atto655, which showed indication for freely rotating molecules. In contrast, Atto655 bounded to the native PGK exhibited a fast but not a complete decay. This indicates a partial rotational freedom of the bounded dye which was most probably confined within a groove on the protein surface.

For the unfolded PGK, we observed again a different behavior. A slower, but complete decay within the observation time is visible. In this case the dye seems to experience a higher rotational freedom than the rotational freedom of the dye attached to native protein, because the protein structure had melted. The protein unfolding dissolves the formerly existing groove and is no longer hindering the rotational motion. Due to a rather flexible protein structure local collisions lead to a slower decay process. In contrast to the cases discussed so far, membrane-embedded dyes (Atto655-labeled DOPE) showed a much weaker anisotropy decay with significantly larger final

anisotropy values. In order to judge whether encapsulated proteins exhibited an interaction with the inner surface of the polymerosomes or not, we compared the results from proteins in solution with those obtained from encapsulated proteins. This comparison revealed that anisotropy decays were rather similar for both cases as shown in Figure 3-3.3. On the other hand, they differed significantly from values obtained for dyes more tightly coupled to the polymerosomes (Atto655-labeled DOPE).

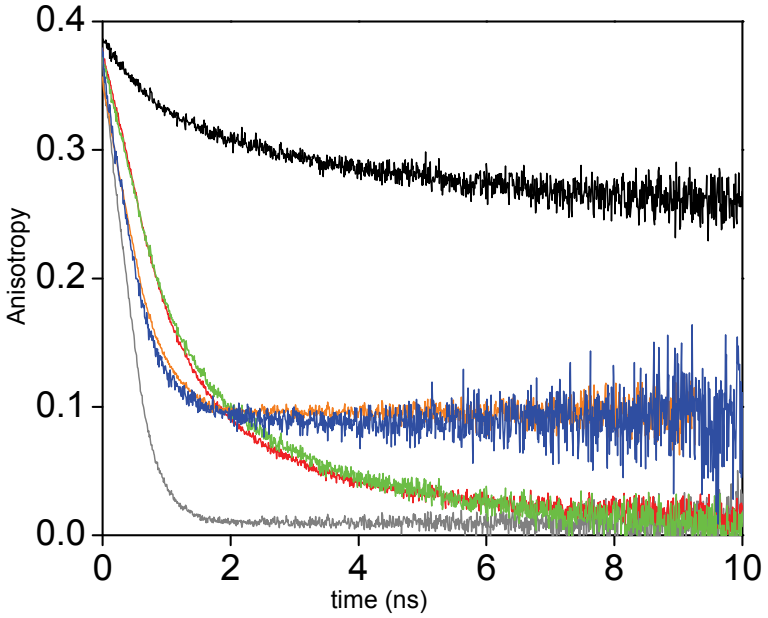

Figure 3-3.3: Anisotropy decays observed for Atto655 in the unbound state (gray curve), bound to freely diffusing unfolded PGK (orange, almost hidden behind the blue curve), bound to freely diffusing native PGK (red), and bound to polymer-matrix-embedded DOPE (black). Green curves (native PGK) and Blue curves (unfolded PGK) represent measurements with encapsulated protein.

To obtain a more detailed picture from the anisotropy decays we fitted the data with an appropriate model as shown in Figure 3-3.4.

The time-resolved fluorescence anisotropy decays were fitted with the **wobbling in-a-cone** model (*26,34*) which is described by:

$$r(t)= r_o\,[(\,1- A_\infty)\,exp(-t/\tau_c)+ A_\infty] \qquad 3\text{-}3.1$$

with $A_\infty = \frac{r_\infty}{r_\circ}$, which this leads to the following equation:

$$r(t)=(\,r_o- r_\infty)\,exp(-t/\tau_c) + r_\infty \qquad 3\text{-}3.2$$

where r_o is the zero time anisotropy, r_∞ is the limiting anisotropy and τ_c is the rotational correlation time. We were fitted the curves using Equation 3-3.2 as shown in Figure 3-3.4 and Table 3-3.2.

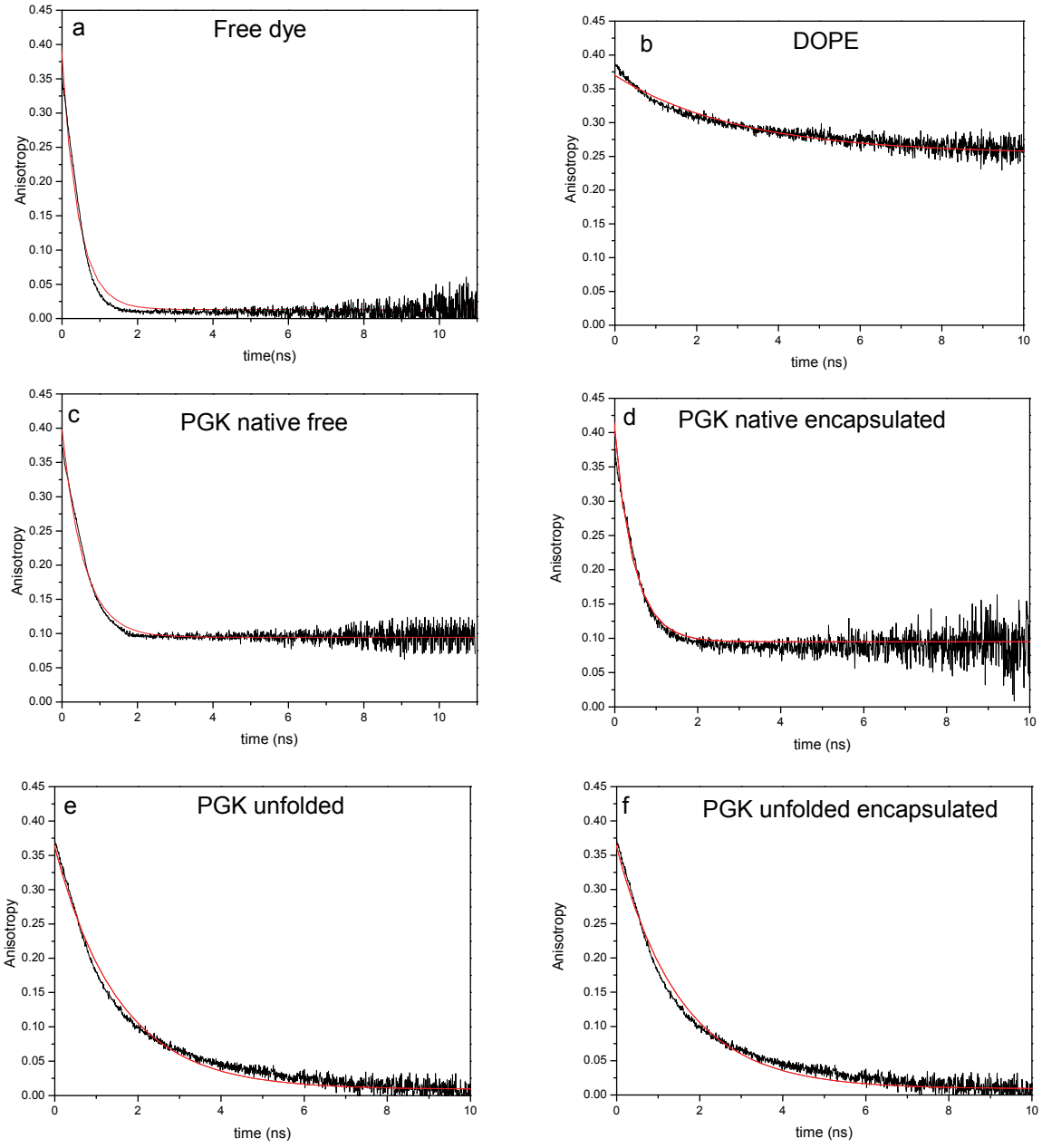

Figure 3-3.4: The experimental data as shown in Figure 3-3.3 (black curve) are tail-fitted (red curve) using the model wobbling in-a-cone (Equation 3-3.2). The fitting parameters are given in Table 3-3.2.

In the table we can see the similarity in the range of error between the fitting data of the free diffused and encapsulated native PGK. Also we can see the same similarity for the

unfolded PGK for the free diffusing and the encapsulated protein. The case of DOPE demonstrates that the encapsulated protein did not stick to the polymerosomes.

Sample		r_o	r_∞	τ_c (ns)
free PGK-Atto655	native	0.397 ± *2* 10^{-3}*	0.094 ± *3*10^{-3}*	0.57 ± *6*10^{-3}*
	5M GdnHCl	0.360 ± *2*10^{-3}*	0.009 ± *5*10^{-4}*	1.55 ± *0.018*
encapsulated PGK-Atto655	native	0.396 ± *0.012*	0.095 ± *1*10^{-3}*	0.5 ± *17*10^{-4}*
	5MGndHCl	0.360 ± *2 *10^{-3}*	0.0092 ± *5*10^{-4}*	1.55 ± *2*10^{-3}*
Atto655	free	0.368 ± *7 *10^{-3}*	0.013 ± *1*10^{-2}*	0.447 ± *17*10^{-3}*
	DOPE	0.369 ± *16*10^{-4}*	0.253 ± *7*10^{-3}*	3.05 ± *9*10^{-2}*

Table 3-3.2: Resulting fitting values of the freely diffusing and encapsulated PGK labeled with Atto655. r_∞-values show a high agreement with those obtained from steady state anisotropy measurements, as shown in Table 3-3.1.

3-3.3 Application of photoinduced electron transfer (PET) to monitor the unfolding/refolding of PGK

Our issue is to study the unfolding process. In our particular case we studied encapsulated proteins which we have proven to be unperturbed upon the encapsulation process. To study the unfolding process we need a method which measures the folding state (folded/unfolded) of PGK. We can not do that with the conventional ensemble methods like circular dichroism (*CD*) spectroscopy or tryptophan fluorescence because the signal from single molecules would be too weak. A good solution to this problem is to use single molecule techniques which can monitor the protein folding (*47,71*). PET with Atto 655 bound to the PGK structure has been proven to monitor protein folding on the single molecule level due to its sensitivity. For analyzing PET the employed dye has to be in the vicinity of a donor. Tryptophan in our case is a donor for Atto655 (*45*). So we bound the dye to the lysine which is near to the tryptophan in the native state. When the protein structure unfolds and the average distance between the dye and the quencher (donor) will increase which would result in a lower quenching efficiency (*16,51*).

In spite of the fact that the amino acid sequence of PGK includes a large number of lysine amino acids (target of the NHS-functionalized dyes), only two lysines (*Lys213,*

Lys257) are in close proximity to the two tryptophans that are located in the C-terminal domain of the protein as shown in Figure 3-3.5.

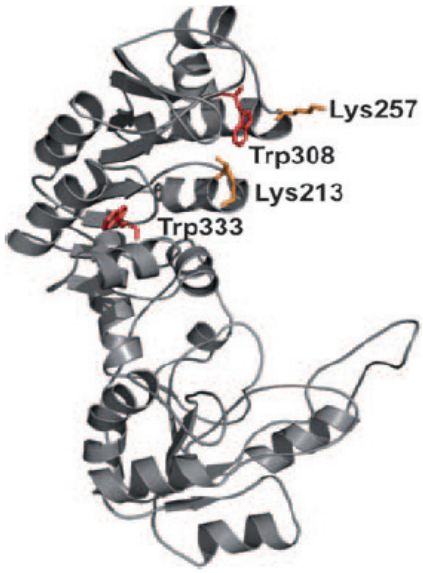

Figure 3-3.5: A structural model of PGK with highlighted Tryptophan residues (red) and two nearby lysine residues (orange), which are supposed to bind NHS functionalized fluorescent dyes.

A preferential labeling of these lysines would give us the opportunity to detect native and unfolded states (*at least of the C domain*) by simply measuring the fluorescence emission intensity of Atto655.

Results from ensemble measurements (Figure 3-3.6) indicate that Atto655 is quenched by nearby of tryptophans. As demonstrated in Figure 3-3.6, the thermally induced unfolding of the protein (monitored by intrinsic Tryptophan fluorescence, blue lines) was accompanied by an increase of the Atto655 emission intensity (red lines), caused by reduced PET upon structural expansion during unfolding. A similar but much more pronounced increase in the emission intensity of Atto655 was observed for PGK incubated in 5M GdnHCl buffer (*60*).

In addition to the unfolding induced fluorescence intensity increase (i.e. reduction of PET) we have to consider that GdnHCl also increases the dissociation constant of the non-fluorescent tryptophan-Atto655 complexes (*16*). This means that the GdnHCl itself reduces the PET. As seen from the temperature-induced unfolding in Figure 3-3.6, the

much stronger signal increase in the Atto655 emission intensity observed upon GdnHCl-induced unfolding is only partly caused by structural unfolding. Moreover, for studying the unfolding conditions of polymerosome-encapsulated proteins on a single-molecule level, the GdnHCl-induced increase of Atto655 fluorescence intensity bound to PGK is a useful measurement.

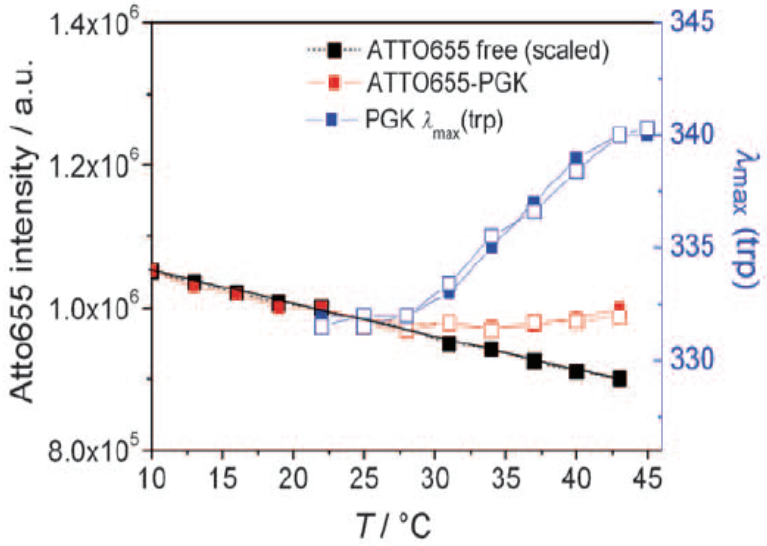

Figure 3-3.6: For ensemble measurements in 0.7M GdnHCl, 30 µM Mops, 50 µM NaCl, 2 µM EDTA, and pH 7.4, the reversible thermal unfolding of PGK was monitored by the shift of the Tryptophan fluorescence emission peak (blue curves, right y-coordinate) and by the Atto655 emission intensity (red curves, left y-coordinate). In both cases, solid and open symbols represent data during heating and cooling, respectively. The black line represents the typical temperature dependence of the fluorescence intensity for free Atto655. The deviation of the red curves from the black curve at temperatures above 30°C is caused by decreasing PET during spatial expansion of the unfolding PGK. The standard deviation for the experimental data points in this figure is on the order of the size of the symbols. This figure is taken from(60).

Finally we want to follow for one at the same molecule repetitive folding and unfolding events. For this particular case we continued the experiments with tethered and encapsulated PGK-Atto655. Then during the experiment we imaged encapsulated PGK under native buffer conditions for 4 seconds followed by an image (also 4 seconds illumination) under unfolding buffer conditions (5M GdnHCl). Analyzing the resulting images, and calculating the counts difference between the folded and unfolded states,

we found that in average, there is an enhancement in counts by approximately 58% for the unfolding conditions. For some integrated peaks we displayed the counts for the folded and the unfolded state as shown in Figure 3-3.7. In the same kind of experiments images from samples incubated with native buffer and with 5M GdnHCl, measured in an alternating sequence, exhibit alternating intensity values from individual spots. In this case we reduced the exposer time to 2 seconds because we do not want to bleach the fluorophores.

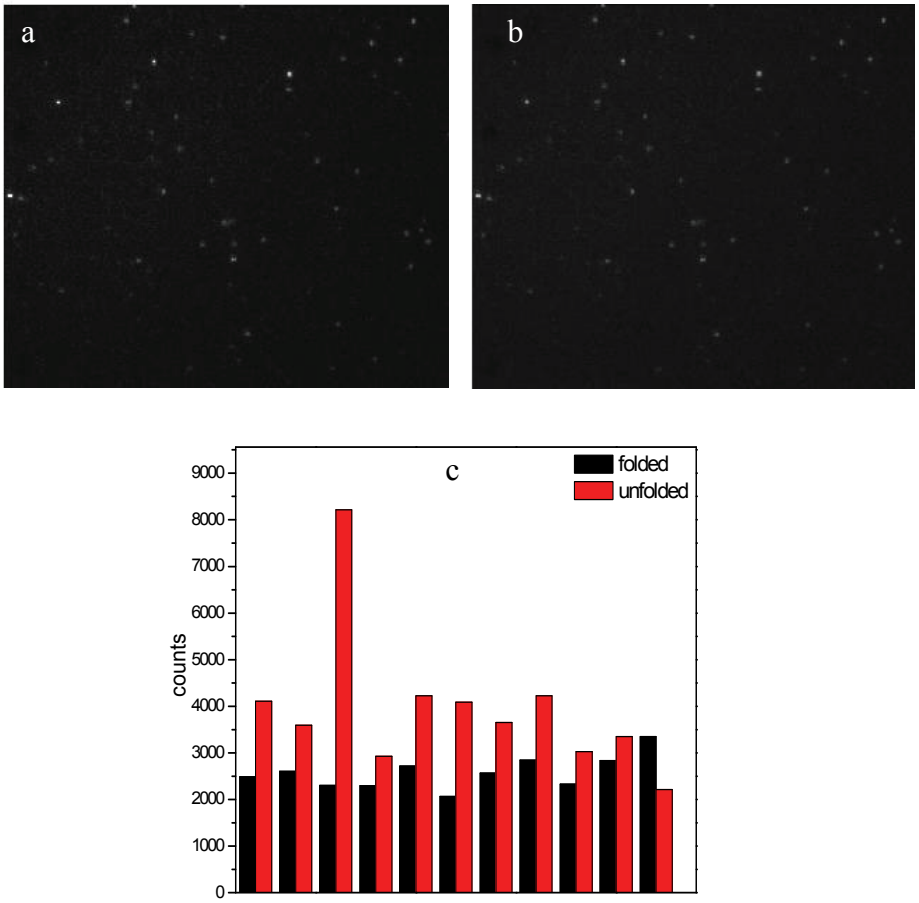

Figure 3-3.7: Wide-field fluorescence images of surface tethered polymerosomes containing Atto655 labeled PGK in a) native buffer, b) 5M GdnHCl buffer. c) The black bars represent the intensity of fluorophores from folded and the red bars that of unfolded PGK. The sample was exposed with a laser line at 640nm for 4 s.

An example of this behavior is shown in Figure 3-3.8. For a large number of spots, we observed an increase in intensities, upon the change from native buffer to unfolding buffer conditions, and a decrease in intensity when changing the buffer back to native.

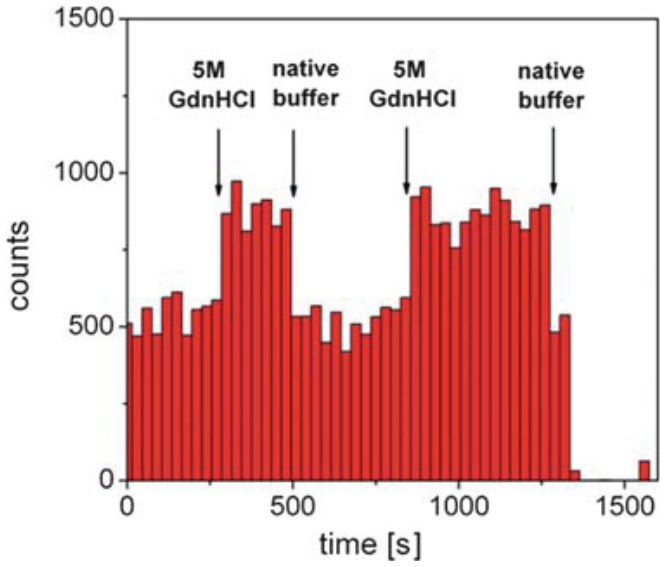

Figure 3-3.8: A typical time course of the measured emission intensity as obtained from the integration of an individual spot is shown in this figure. The images were measured every 30 s with polymerosomes bound to cover slides. The arrows indicate buffer exchange from native to unfolding conditions or vice versa.

Since the PET approach worked quite well with PGK we wanted to extend these studies to other proteins like BLA and TAKA. Although Atto655 labeled BLA and TAKA exhibited similar anisotropy values as observed for PGK (Table 3-3.1), we did not observed the typical Atto655 fluorescence intensity changes caused by PET upon unfolding and refolding transitions (see also section 3-4.2). In contrast to PGK, Atto 655-labeled α-amylases did not show PET or a change in Atto655 fluorescence emission intensities upon protein unfolding. This indicates that for the investigated α-amylases, none of the lysine in the vicinity of tryptophan was accessible for Atto655-NHS.

3-4 Native and unfolded states of multi-domain proteins studied by FCS

As stated earlier a protein is a sequence of polypeptides in a chain forming secondary and tertiary structure elements which give the protein its functionality. This process is called protein folding. The native protein is typically characterized by a rather compact state. We are interested to study the unfolding of multi-domain proteins, particularly the α-amylases like TAKA from *Aspergillus oryzae* (52.5 kDa, 499 residues (*4*)) and the alpha amylase BLA from *Bacillus licheniformis* (58.3 kDa, 512 residues (*5*)). The structure of each is shown in Figure 3-4.1. In addition we also want to study Phosphoglycerate kinase from baker yeast (PGK, 44.3 kDa, 415 residues (*10,35,70*)). PGK is composed of two roughly equally sized subunits connected by a flexible hinge (*14,70*). As shown in Figure 3-4.1 TAKA and BLA are composed of three domains.

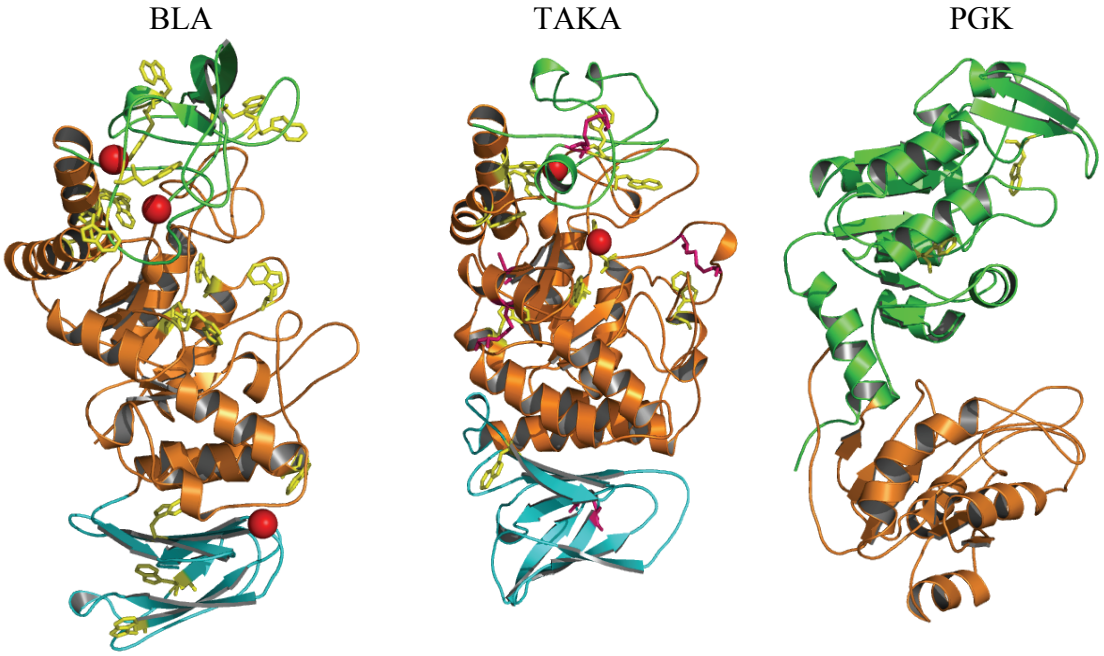

Figure 3-4.1: Schematic drawing of studied proteins in a cartoon style from the protein data bank(10,43,70). In this scheme the colors orange, green and cyan represent different domains in the respective proteins.

An unfolding induced structural expansion of the proteins should be visible when we measure a parameter which is related to the size of the protein. This parameter might be the radius of gyration in the case of employing small angle scattering by neutrons or X-

rays. Also one can use the hydrodynamic radius as a size parameter determined by dynamic light scattering or by fluorescence correlation spectroscopy. Our purpose is to study the degree of unfolding as a function of a chemical denaturant (GndHCl) concentration for PGK, TAKA and BLA using the FCS technique.

As a result of adding a high concentration (a few molar) of GndHCl to the buffer, the buffer viscosity will be changed. The change of the buffer viscosity leads also to change of the refractive index. Due to the fact that we have different molarities of the GndHCl, we have different viscosities. As discussed before in Section 2-3.1 the detection volume is a function of the refractive index, so we have to correct our obtained results for these changes. In this particular case we have to determine exactly the confocal volume for the different buffer concentrations. Using known diffusion coefficients, in our case of some dyes, we can determine the required detection volume. The diffusion coefficient of the free dye was already measured (see Section 3-1.3) and is well defined in the native buffer (50mM Na_2CO_3, pH7.4). With these known values of the diffusion coefficients we can use Equation 3-4.1 to calculate apparent hydrodynamic radii of free dyes which are not expected to change according to the buffer. The addition of chemical denaturant GndHCl to the native buffer affects the buffer viscosity according to the GndHCl concentration. I used some of the published values (*36*) and interpolated by using a simple polynomial (see Figure 3-4.2).

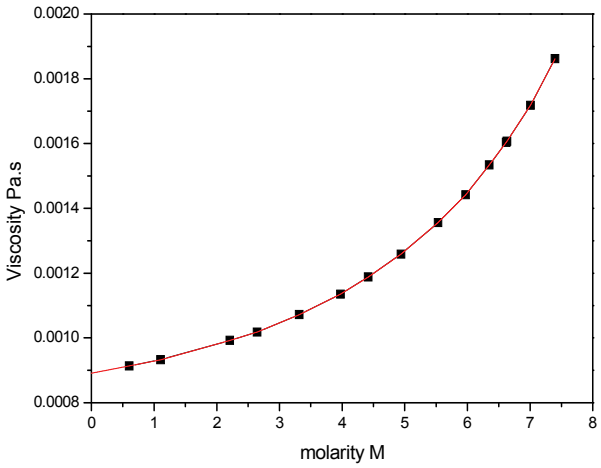

Figure 3-4.2: The viscosity values for different molarities of the chemical denaturant GndHCl. The black squares are the known values from the literature(36), while the red line represents the interpolating polynomial.

Using the viscosity values for different GndHCl concentration we can calculate the diffusion coefficient as shown in Table 3-4.1, and Figure 3-4.1 using the following equation (*52*):

$$D(\eta,T)=\frac{K_B T}{6\ \pi\ \eta\ R_h} \qquad 3\text{-}4.1$$

where K_B is Boltzmann constant, T is the temperature in Kelvin, η is the medium viscosity, and R_h is the hydrodynamic radius of the diffusing particle.

	Alexa 647			Atto 655		
GndHCl Conc. (M)	***R_h (nm)***	***D_{25} ($\mu m^2/s$)***	***V_{eff} (fl)***	***R_h (nm)***	***D_{25} ($\mu m^2/s$)***	***V_{eff} (fl)***
0	0.71	343 (a)	2.1	0.6	407 (b)	2.1
0.5		334	2.1		396	2.2
1		328	2.2		390	2.1
2		311	2.3		370	2.3
4		267	2.8		319	2.8
6		208	2.7		248	2.5

Table 3-4.1: Calculated diffusion coefficients using Equation 3-4.1 (black numbers). The temperature was set at 298°K (i.e. 25 °C). The value of R_h was calculated in advance using the same equation for the measured diffusion coefficient value of the free dye (red numbers) diffusing in native buffer (i.e. 0M, more details in Section 3-1.3). The last column lists the fitted effective confocal volumes for each denaturant concentration. (a) This value is from a personal communication with A. Loman and (b) from the reference(49). Both values were also verified by measurements using the dilution series method.

Also in this table I show the effective detection volume (V_{eff}) related to each GndHCl concentration (more explanation about the method in Section 3-2). To see the effect of different GndHCl concentration on the diffusion time of the diffusing dye, we fitted the auto-correlation curve with an appropriate model (for more details see Section 2-3.1).

One example of an auto-correlation fit is shown in Figure 3-4.3.

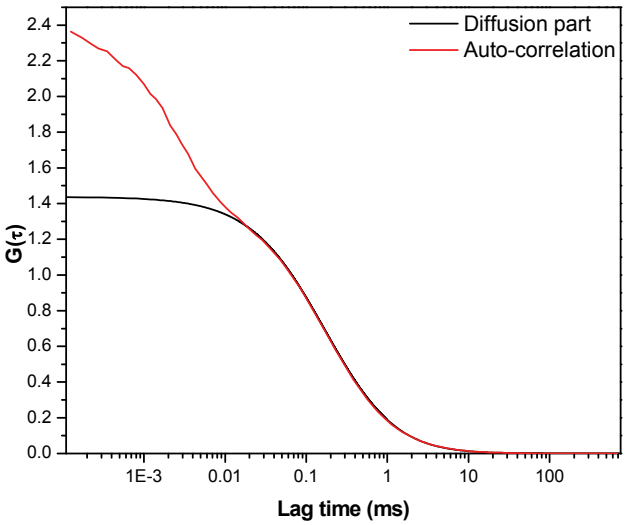

Figure 3-4.3: The auto-correlation curve of Alexa 647 pure dye diffusing in native buffer and the diffusion part (fit) as calculated using Equation 2-3.12.

The auto-correlation curves of the Atto655 and Alexa647 at different GndHCl concentrations are shown in Figure 3-4.4.

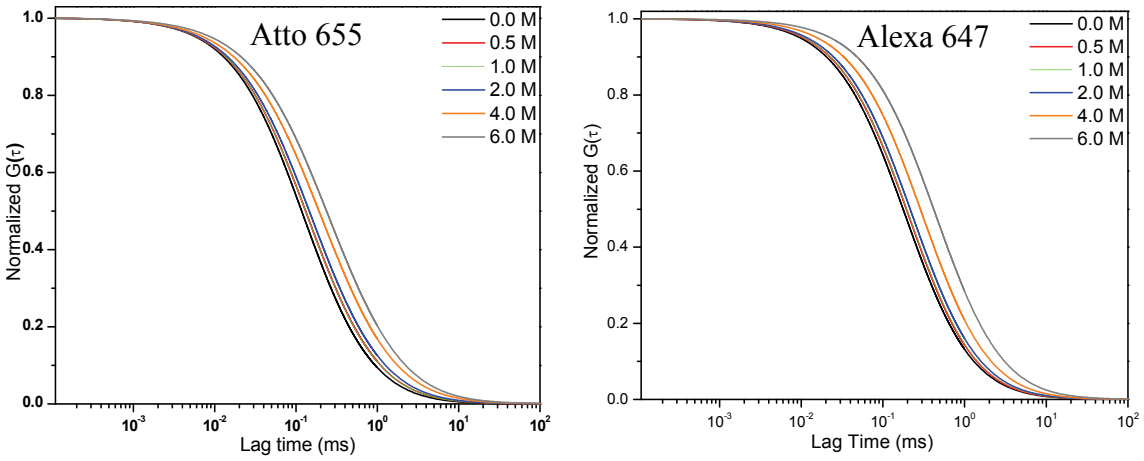

Figure 3-4.4: The pure diffusion part of the auto-correlation curve fitting of free dye diffusing in different concentrations of chemical denaturant GndHCl.

In Figure 3-4.5 we can see the resulting changes in the diffusion coefficient as function of denaturant concentration.

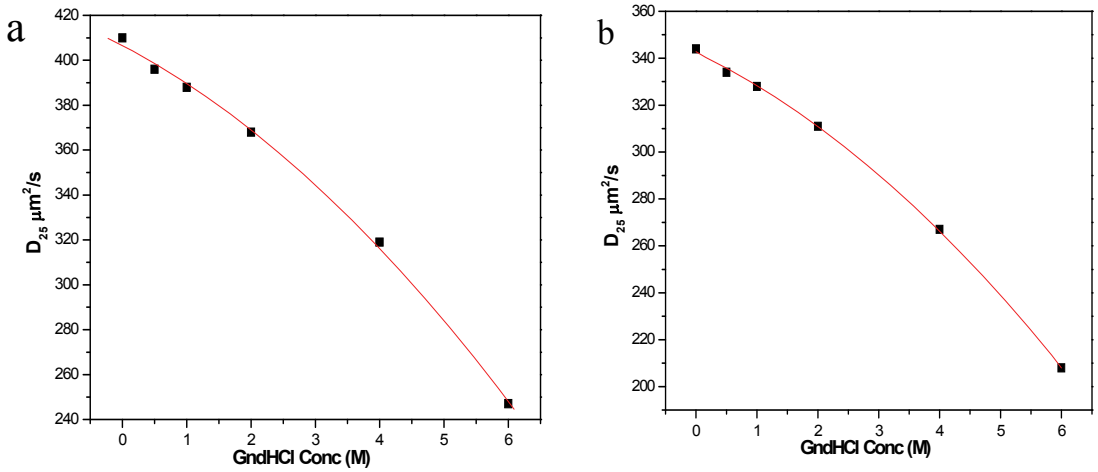

Figure 3-4.5: The diffusion coefficients as a function of GndHCl concentrations (black squares) of diffusing free Atto655 (a) and Alexa647 (b). The red line is a polynomial fit.

It is known from the literature that the sensitivity of proteins to chemical denaturants is different, depending on their individual stability (*30,32*). Therefore we measured the diffusion of the labeled proteins at different denaturant concentrations. An important parameter in this respect is given by the $C_{1/2}$-value, which gives the denaturant concentration where the protein is half folded/unfolded. The $C_{1/2}$ values for GndHCl of the proteins under investigation are listed in Table 3-4.2.

Protein	PGK	BLA	TAKA
$\boldsymbol{C_{1/2}}$ **(M)**	0.7	0.98	0.34

Table 3-4.2: The $C_{1/2}$ values for GndHCl of the proteins PGK, BLA and TAKA(41).

Knowing the $C_{1/2}$ values for the individual proteins we can relate different diffusion coefficients of the proteins measured at specific denaturant concentrations to structural parameter of the proteins (R_h) to obtain information on various folding states. As discussed above we have to consider effects caused by changes of solvent properties which have been analyzed in detail with free dyes (see Figure 3-4.4 and 3-4.5).

3-4.1 Determination of hydrodynamic radii for GndHCl induced unfolded states

By using FCS we want to measure the diffusion and thereby the hydrodynamic radius of the proteins, the latter as a measure of the protein size. In this respect FCS is a straight forward method because we can attach our dyes to any position at the protein and the result is not depending on the label position, in contrast to FRET and /or PET studies. Here we want to study the unfolding properties of PGK and of some α-amylases. The results for PGK are shown in Figure 3-4.6.

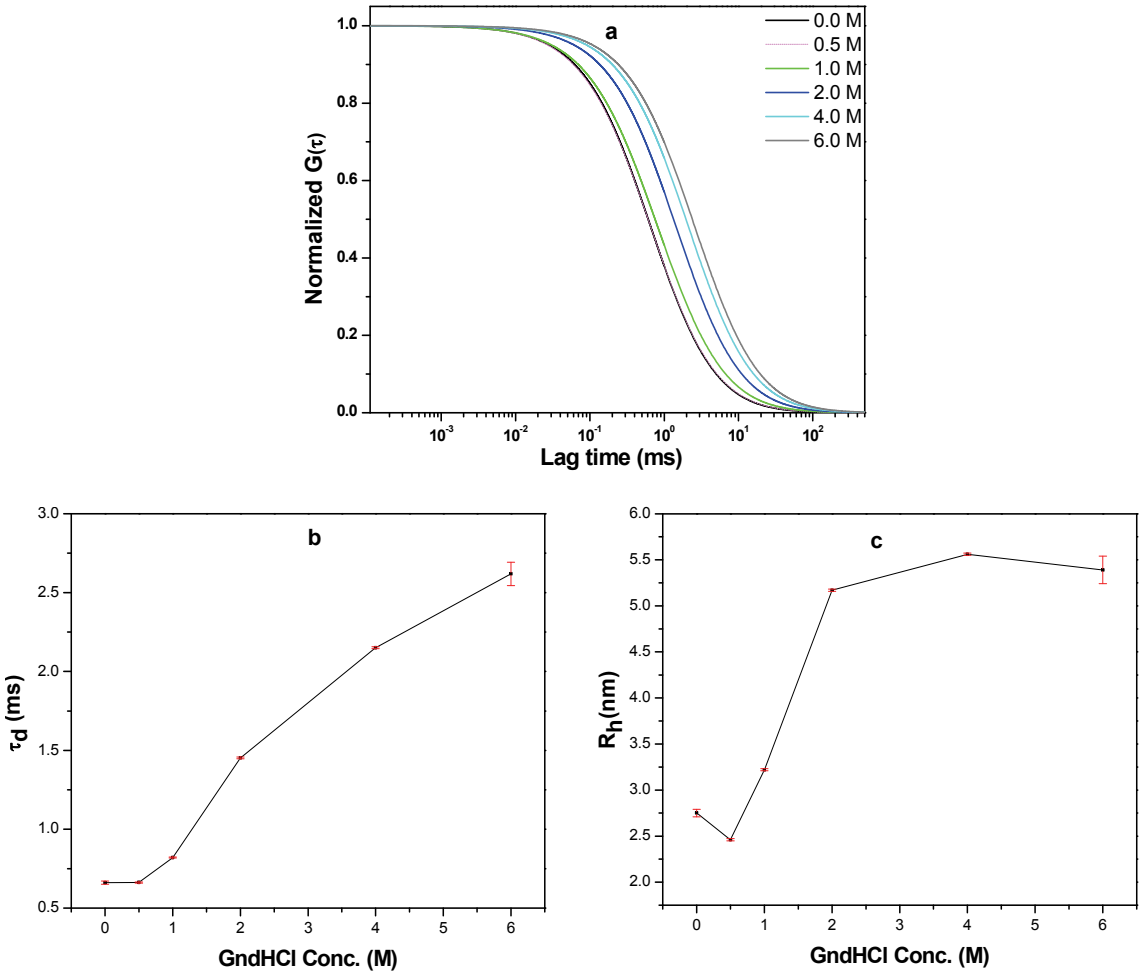

Figure 3-4.6: The diffusion of PGK labeled with Alexa647 diffusing in different concentrations of the chemical denaturant GndHCl with incubation time 1h. a) The pure diffusion fitting part of the auto-correlation. b) The diffusion time of the diffusing protein. c) The hydrodynamic radius of the diffusing protein calculated using Equation 3-4.1.

Equivalent results for BLA are shown in Figure 3-4.7 and for TAKA in Figure 3-4.8.

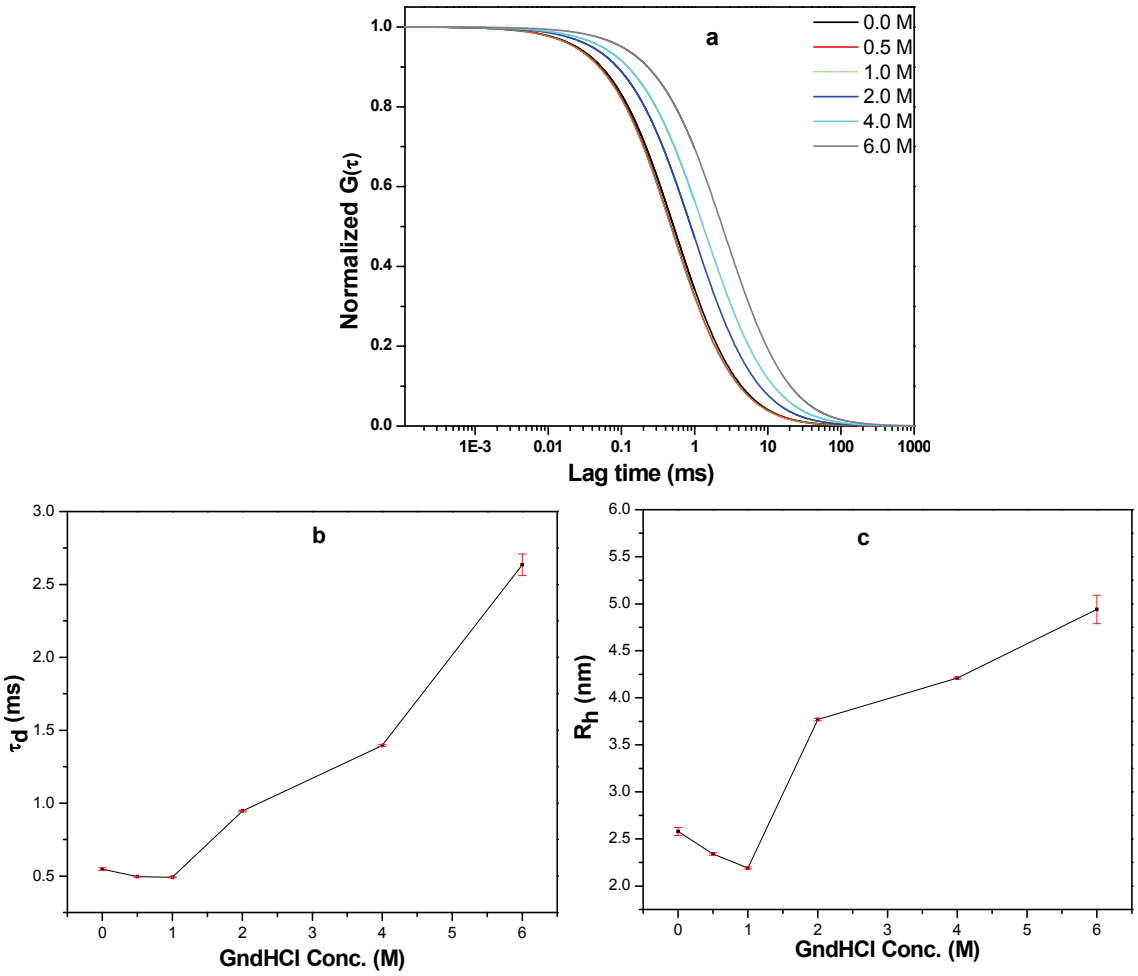

Figure 3-4.7: The same measurements like in Figure 3-4.6 but for BLA.

As expected for most proteins the increase of the GndHCl concentration causes an expansion of the protein structure. For PGK this is notable from the increased viscosity corrected diffusion times and their corresponding hydrodynamic radii. At low concentration of the denaturant ($C < 1.5\ M$) there is an unexpected increase in the diffusion coefficient resulting in a decrease of hydrodynamic radii, or in other words an apparent collapse of the protein structure. This apparent collapse was also detected by FRET measurements for other of proteins (*48*). A similar compaction was obtained from single molecule FRET studies with PGK (*61*).

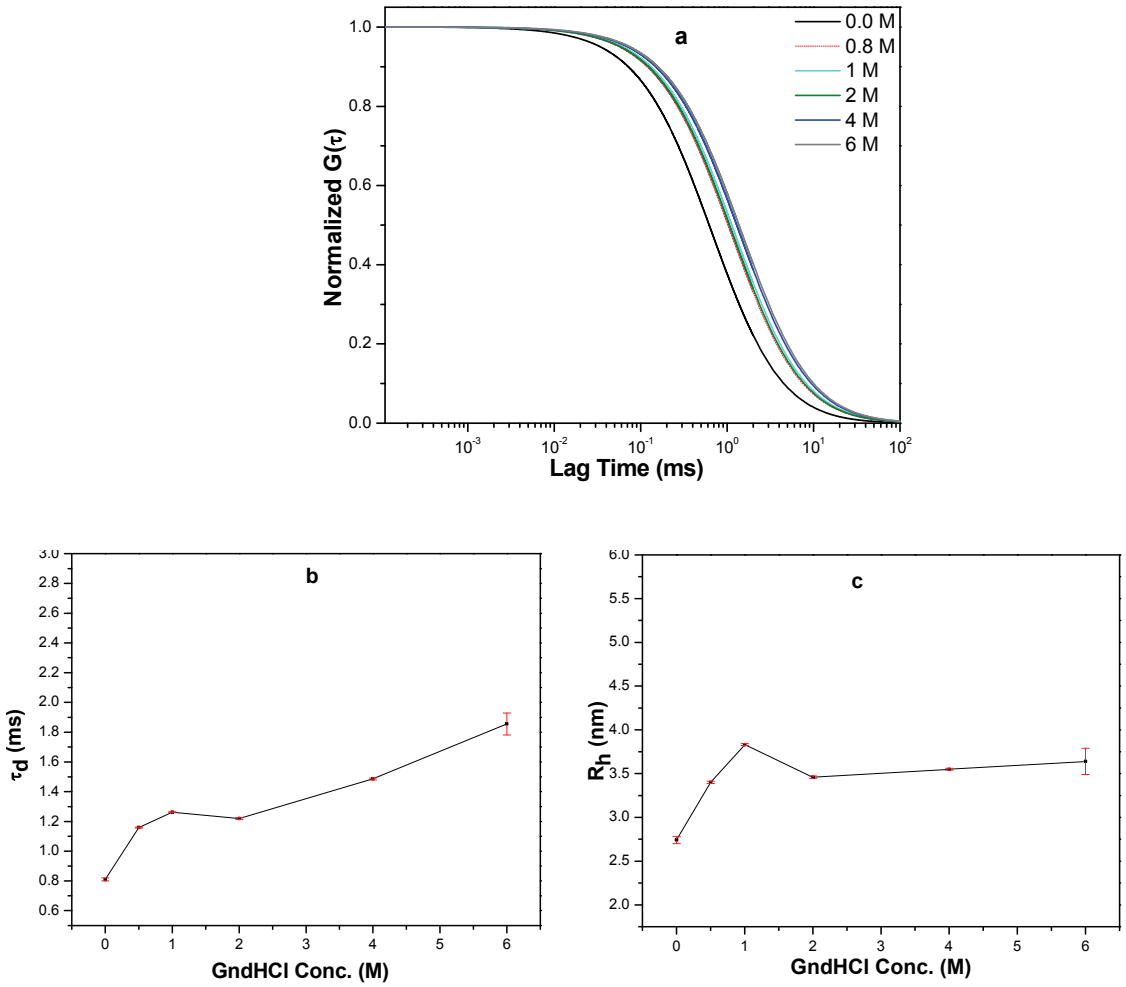

Figure 3-4.8: The same measurements like in Figure 3-4.6 but for TAKA.

We observed for PGK this slight compaction at concentrations of 0.5 molar GndHCl. Interestingly a similar compaction was also observed for other salts of the Hofmeister series (*61*). It is therefore assumed that this effect is related to interactions caused by hydrophobic effects (*29*) and by charge-charge interactions. The compaction according of GndHCl concentration is not the same for all proteins. In PGK we found that the compaction takes place around 0.5 M of GndHCl. The compaction of the BLA takes place at higher denaturant concentrations while TAKA does not show such a compaction.

The hydrodynamic radii of our proteins are in a reasonable regime between 2.8-3.2 nm for the native state. Unfortunately, we obtained values which are partly smaller in the native state and in the early unfolding states which demonstrates that we still have some problems with the determination absolute R_h values from FCS. However, at least

relative values are more reliable and the general tendencies of R_h values changes can be trusted. According to this we see a small compaction of the native state and then the proceeding unfolding is really increasing the hydrodynamic radius dramatically, even at high concentration of GdnHCl above 3M. We see in most cases a still expanding protein. This phenomenon is known as the global coil transition and was also observed in many FRET studies (*61*), not only for PGK.

3-4.2 Analyzing structural dynamics and compactness by employing PET

When a protein is in the native state the structure exhibits certain flexibility and the residues are partly free to move. The PET rate (more details about PET in Section 2-4) can give a measure about how fast the structure is fluctuating. At the same time the PET rate is also determined by the collision frequency of the electron donor and the related acceptor which is strongly depending on the average distance between both colliding partners. Therefore a decreasing PET rate can be indicative for an increasing average distances between both colliding partners. So the PET rate can be employed to measure the structural compactness of our Atto655 labeled PGK (see Section 3-3.3). For this purpose we performed again FCS measurements with Atto655 labeled PGK at different concentrations of GndHCl as a chemical denaturant. In contrast to the previous cases we did not only analyze the pure translational diffusion but also investigated faster fluctuations assumed to be related to PET. Atto655 is a stable dye and did not show significant triplet state transitions, as shown in Figure 3-4.9. So any fast process which shows up in the auto-correlation function should be related to dynamical dye quenching, which is in the case of our PGK sample caused by PET between Atto655 and the neighboring tryptophan residues.

As we discussed before in Section 2-3 the auto-correlation can be fitted with an appropriate model. In the case of PET we used the following model (*27,63*):

$$G(\tau) = \left(1 - A_{PET} + A_{PET} e^{\left(-\frac{\tau}{\tau_{PET}}\right)}\right) G(0) \left(1 + \frac{\tau}{\tau_D}\right)^{-1} \left(1 + \frac{\tau}{\tau_D \kappa^2}\right)^{-1/2} \qquad 3\text{-}4.2$$

where τ_D the diffusion time, τ_{PET} is the diffusion time of quenched fluorophore. A_{PET} is the amplitude of quenched fluorophore diffusion.

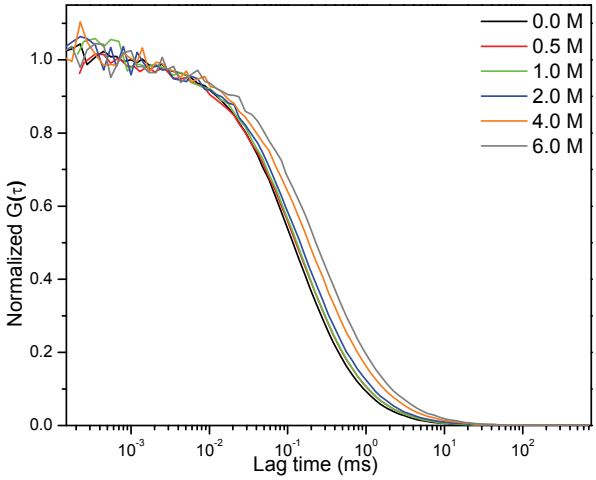

Figure 3-4.9: Normalized autocorrelation curves of free Atto655 diffusing in different concentrations of GndHCl.

This model is equal to that which considers triple state dynamics and was introduced already in Section 2-3.1. Like in the previous section I made a fitting of the pure diffusion part (not shown) to take the maximum value in this fitting as a normalization factor (Figure 3-4.10 and Table 3-4.3). We can see that for low concentrations of GndHCl and for the native state we obtain a fast process. In other words we have two processes, one is very fast (with amplitude A_{PET}) in the order of a few hundred nanoseconds and another one is slower (with amplitude A= G (0) - A_{PET}) in the order of fractions of milliseconds. The slower one refers to the translational diffusion of PGK. The faster one refers to those proteins which experienced a complex formation between the Atto655 and tryptophan. The amplitude of both components (A and A_{PET}) gives an idea about the concentration of the quenched and non quenched fluorophores. It is clear from Table 3-4.3 and Figure 3-4.10 that we have a very fast process, showing a decreasing amplitude A_{PET} with an increase of the denaturant concentrations.

In order to obtain a more detailed picture of the underlying processes, we take a closer look at the obtained fitting parameters. The association rate constant k_+ and dissociation rate constant k_- of the colliding partners could be extracted from our data if we rewrite our model function in slightly different manner.

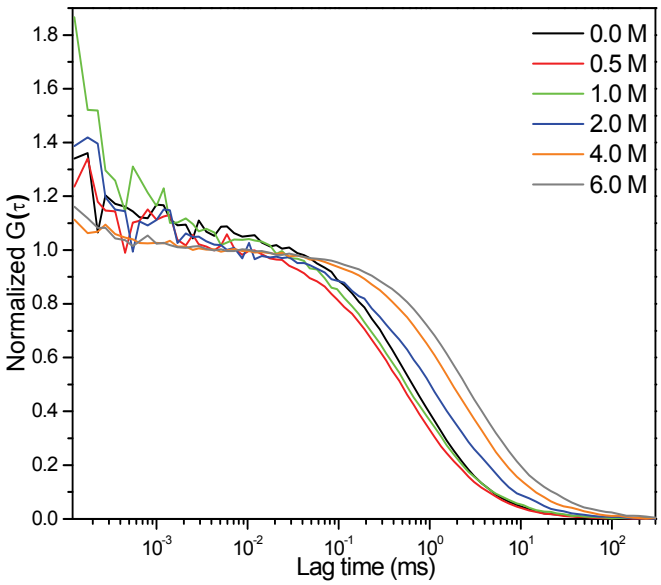

Figure 3-4.10: The normalized auto-correlation of the PGK labeled with Atto655 diffusing in different GndHCl concentrations with incubation time 1h. The auto-correlation curves are normalized to the G(0) of the pure diffusion component.

The auto-correlation equation in the case of diffusing quenched particle gives in a 2D approximation (see (*16*)):

$$G(\tau) = \frac{1}{\langle N \rangle} \frac{1}{1 + \frac{\tau}{\tau_D}} \left(1 + k_{equ} e^{\left(-\frac{\tau}{\tau_{exp}} \right)} \right) \qquad 3\text{-}4.3$$

Here $\tau_{exp} = (k_+ + k_-)^{-1}$ is the correlation time and $k_{equ} = k_+ / k_-$ is the equilibrium constant, both determined by the association and the dissociation rate of the PET collision partners k_+ and k_-, respectively. With only one species of diffusing particles in the 2D approximation we obtain from Equation 2.3.19 and 3-4.2 the following:

$$G(\tau) = \left(1 - A_{pet} + A_{pet} e^{\left(-\frac{\tau}{\tau_{pet}} \right)} \right) G(0) \left(1 + \frac{\tau}{\tau_D} \right)^{-1} \qquad 3\text{-}4.4$$

GndHCl Conc. (M)	D ($\mu m^2/s$)	τ_D (ms)	A	A_{PET}	τ_{PET} (10^{-7} s)	R_F%
0	74	0.67	4.33	0.51	1.00	11.84
0.5	100	0.53	6.1	0.542	1.20	8.89
1	91	0.61	3.63	0.68	1.00	18.68
2	53	1.1	3.97	0.17	4.00	4.21
4	33.8	1.95	5.33	0.098	5.00	1.84
6	26.3	2.83	3.34	0.099	3.00	2.96

Table 3-4.3: The diffusion coefficient D, the diffusion time τ_D, the pure diffusion amplitude A of PGK labeled with Atto655 diffusing in different concentration of GndHCl with incubation time 1h. τ_{PET} is the inverse PET rate of quenched fluorophores and A_{PET} is the amplitude of the quenching process. R_F is the fraction percentage of A_{PET} to A. All the previous parameters are calculated according to the auto-correlation Equation 3-4.2. From 2-3.20 $A = G(0) * (1 - A_{trp})$

from Equation 2-3.20

$$G(0)\ (1 - A_{pet}) = \frac{1}{\langle N \rangle} \Rightarrow\ \langle N \rangle\ G(0) = \frac{1}{(1 - A_{pet})} \qquad 3\text{-}4.5$$

$$G(\tau) = (1 - A_{pet}) \left(1 + \frac{\tau}{\tau_D}\right)^{-1} G(0) + G(0) A_{pet} \left(1 + \frac{\tau}{\tau_D}\right)^{-1} e^{\left(-\frac{\tau}{\tau_{pet}}\right)}$$

$$= \frac{1}{\langle N \rangle} \frac{1}{1 + \frac{\tau}{\tau_D}} + G\ (0) A_{pet} \frac{1}{1 + \frac{\tau}{\tau_D}} e^{\left(-\frac{\tau}{\tau_{pet}}\right)}$$

$$G(\tau) = \frac{1}{\langle N \rangle} \frac{1}{1 + \frac{\tau}{\tau_D}} \left(1 + \langle N \rangle\ G(0)\ A_{pet}\ e^{\left(-\frac{\tau}{\tau_{pet}}\right)}\right)$$

from Equation 3-4.5 $\quad \langle N \rangle\ G(0) = \frac{1}{1 - A_{pet}}$

$$G(\tau) = \frac{1}{\langle N \rangle} \frac{1}{1 + \frac{\tau}{\tau_D}} \left(1 + \frac{A_{pet}}{1 - A_{pet}} e^{\left(-\frac{\tau}{\tau_{pet}}\right)}\right) \qquad 3\text{-}4.6$$

Comparing Equation 3-4.6 with Equation 3-4.3 one obtains

$$k_{equ} = \frac{k_+}{k_-} = \frac{A_{pet}}{1 - A_{pet}} \qquad 3\text{-}4.7$$

and $$\tau_{\exp} = \tau_{pet} = \frac{1}{k_+ + k_-} \qquad 3\text{-}4.8$$

Solving the Equations 3-4.7 and 3-4.8 simultaneously we obtain for the association/dissociation rate constants

$$k_+ = \frac{A_{pet}}{\tau_{pet}} \quad and \quad k_- = \frac{1 - A_{pet}}{\tau_{pet}} \qquad 3\text{-}4.7$$

Finally we can calculate the association and dissociation rate constants using the values of Table 3-4.3 as shown in Table 3-4.4.

GndHCl Conc. (M)	A_{PET}	τ_{PET} (10^{-7} s)	k_{equ}	$1/k_+$ (10^{-6} s)	$1/k_-$ (10^{-6} s)
0	0.51	1.00	1.04	0.19	0.20
0.5	0.542	1.20	1.18	0.22	0.26
1	0.68	1.00	2.13	0.15	0.31
2	0.17	-	-	-	-
4	0.098	-	-	-	-
6	0.099	-	-	-	-

Table 3-4.4: The association k_+ dissociation k_- rate constants of PGK are given as a function of the GndHCl concentration. For PET components with amplitudes $A_{PET} < 0.2$ no reliable rate constants can be given. From 3-3.20 $A = G(0) * (1 - A_{trp})$

Compared to previous studies from Sauer and co-workers (*16*), where they studied free trypthophan with free MR121 (very similar to Atto655) at different GndHCl concentrations (0-5 M), we obtained here association and dissociation rates which are at least in the same order of magnitude. Sauer et al. obtained values for both inverse rates in the order of 10-100 ns, while our inverse rates are slower by a factor of 2-10 (Tab. 3-4.4 and Fig. 3-4.11). There are several possible reasons for this observed difference. First our sample is rather different, since we are dealing with dyes and quenching partners which are part of the protein structure, while in the literature case free diffusion particles are investigated. This can give rise to a significant change in the accessibility of the PET partner molecules to GndHCl molecules. As a result the effect of GndHCl on life time of the PET-complex can be quite different. Secondly, the correlation times of

the association/dissociation events are rather fast and on the edge of our measuring window (see Fig. 3-4.10). Therefore, we cannot rule out that in particular at higher GndHCl concentrations much stronger PET amplitudes with faster rates may occur.

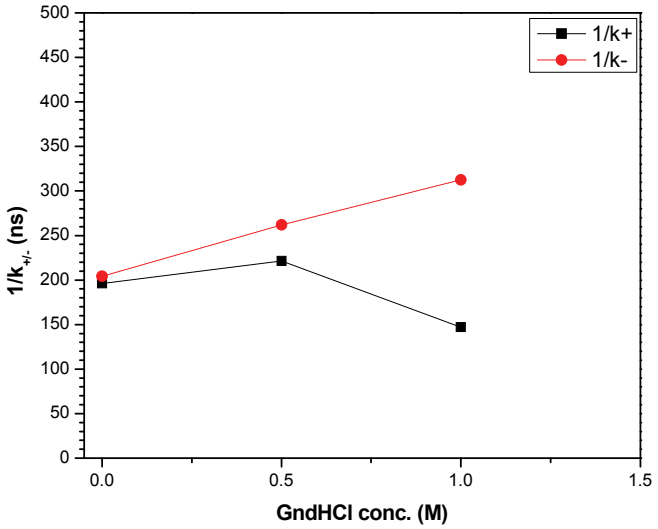

Figure 3-4.11: The effect of GndHCl concentration on the association $1/k_+$ and the dissociation $1/k_-$ rate constants of the TRP-Atto655 of PGK complex formation.

At a concentration of 1 M GndHCl we found that the amplitude of this fast PET process is the highest which might be an indication for the closest distance between both PET partners and would refer to a protein compaction which we have already seen in the previous subsection. This is also visible in an anti-correlated PET amplitude with respect the PGK hydrodynamic radius, as shown in Figure 3-4.12 for different concentration of the GdnHCl.

To assure that we really observe tryptophan-Atto655 collisions and therefore a PET process in the respective auto-correlation measured with PGK, we also studied labeled BLA and TAKA samples. From the results discussed previously, we know that for the α-amylases we do not observe any PET (see section 3-3.3).

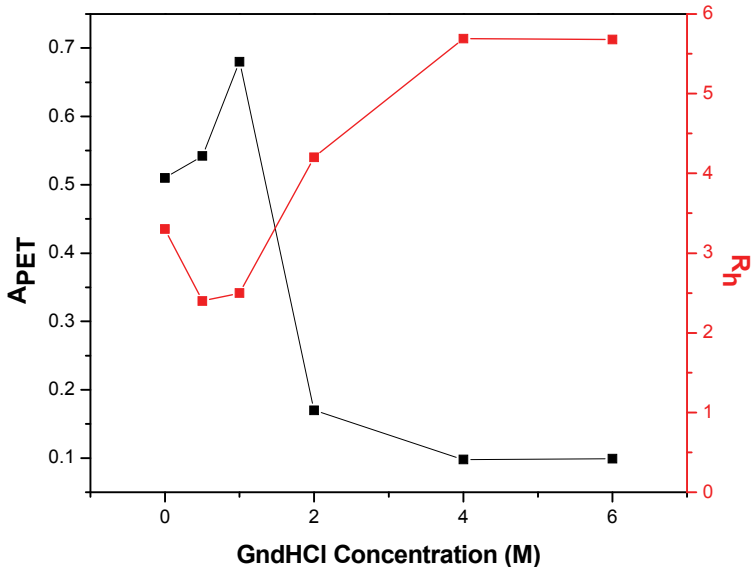

Figure 3-4.12: The change of the PET component amplitude (black line) and the hydrodynamic radius (red line) of the PGK with the denaturant concentration.

In Figure 3-4.13 and Tables 3-4.5 and 3-4.6 auto-correlation curves and resulting parameters clearly show, that we do not have a fast process, similar to results obtained with the free Atto655.

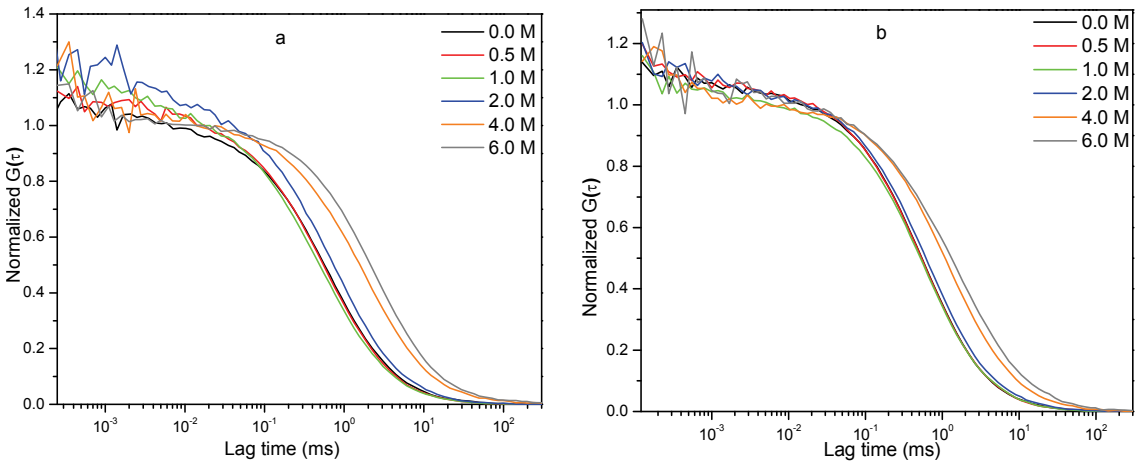

Figure 3-4.13: The same measurements like in Figure 3-4.6 but for a) BLA, b) TAKA.

Although the results from PGK indicate clearly that we are observing dynamical collision between PET partner molecules, the interpretation of these result in terms of structural changes and dynamical properties of the protein structure is not straightforward. Since the PET rate depends not only on the average distance between the colliding partners (because it defines the probability of collisions) but also on the

GndHCl concentration, which directly influences the dissociation rate k_- *(16)*, the measured PET rates do not give unambiguous on the structural state of the protein.

GndHCl Conc. (M)	***D ($\mu m^2/s$)***	***τ_D (ms)***	***A***	***A_{PET}***	***τ_{PET} (ms)***	***R_F%***
0	88	0.61	3.88	$4.20 \cdot 10^{-5}$	-	0.001
0.5	94	0.60	4.85	0.065	-	1.3
1	102	0.54	4.43	0.054	-	1.2
2	72	0.79	5.91	0.076	-	1.2
4	40.6	1.72	2.83	0.041	-	1.4
6	29.8	2.34	2.27	0.022	-	0.95

Table 3-4.5: The same values like in Table 3-4.3, here for BLA.

GndHCl Conc. (M)	***D ($\mu m^2/s$)***	***τ_D (ms)***	***A***	***A_{PET}***	***τ_{PET} (ms)***	***R_F%***
0	81	0.64	8.90	0.03	-	0.3
0.5	86	0.60	8.54	0.01	-	0.1
1	78	0.67	7.89	0.04	-	0.5
2	67	0.88	6.20	0.09	-	1.4
4	46.3	1.35	4.06	0.05	-	1.2
6	30.5	2.01	4.19	0.04	-	0.95

Table 3-4.6: The same values like in Table 3-4.3, here for TAKA.

References

1. http://zeiss-campus.magnet.fsu.edu/print/probes/jellyfishfps-print.html

2. http://products.invitrogen.com/ivgn/product/F8792

3. Green Fluorescent Protein From Aequorea Victoria . http://www.rcsb.org/pdb/explore/explore.do?structureId=1EMA . 2009.

4. *AMYA1_ASPOR*. http://www.uniprot.org [47]. 2011. UniProtKB/Swiss-Prot.

5. *AMY_BACLI*. http://www.uniprot.org [112]. 2011. UniProtKB/Swiss-Prot.

6. A.Katranidis (2009) Single Molecule Studies on Co-translational Folding of Nascent Polypetide Chains, *Thesis/Dissertion*.

7. Amirgoulova, E. V., Groll, J., Heyes, C. D., Ameringer, T., Rocker, C., Moller, M., and Nienhaus, G. U. (2004) Biofunctionalized Polymer Surfaces Exhibiting Minimal Interaction Towards Immobilized Proteins, *Chemphyschem 5*, 552-555.

8. Andrew B.Cubitt, Roger Heim, Stephen R.Adams, Aileen E.Boyd, Larry A.Gross, and Roger Y.Tsien (1995) Understanding, Improving and Using Green Fluorescent Proteins., *Trends in Biochemical Sciences 20*, 448-455.

9. Avaltroni, F., Seijo, M., Ulrich, S., Stoll, S., and Wilkinson, K. J. (2006) Conformational Changes and Aggregation of Alginic Acid as Determined By Fluorescence Correlation Spectroscopy, *Biomacromolecules 8*, 106-112.

10. Boel, E., Brady, L., Brzozowski, A. M., Derewenda, Z., Dodson, G. G., Jensen, V. J., Petersen, S. B., Swift, H., Thim, L., and Woldike, H. F. (1990) Calcium Binding in Alpha-Amylases: an X-Ray Diffraction Study at 2.1-Angstrom Resolution of Two Enzymes from *Aspergillus*, *Biochemistry 29*, 6244-6249.

11. Boukobza, E., Sonnenfeld, A., and Haran, G. (2001) Immobilization in Surface-Tethered Lipid Vesicles as a New Tool for Single Biomolecule Spectroscopy, *Journal of Physical Chemistry B 105*, 12165-12170.

12. Clark, P. L. and King, J. (2001) A Newly Synthesized, Ribosome-Bound Polypeptide Chain Adopts Conformations Dissimilar from Early *in vitro* Refolding Intermediates, *J Biol Chem. 276*, 25411-25420.

13. Das, S. K., Darshi, M., Cheley, S., Wallace, M. I., and Bayley, H. (2007) Membrane Protein Stoichiometry Determined from the Step-Wise Photobleaching of Dye-Labelled Subunits, *Chembiochem. 8*, 994-999.

14. Dhar, A., Samiotakis, A., Ebbinghaus, S., Nienhaus, L., Homouz, D., Gruebele, M., and Cheung, M. S. (2010) Structure, Function, and Folding of Phosphoglycerate Kinase are Strongly Perturbed by Macromolecular Crowding, *Proceedings of the National Academy of Sciences 107*, 17586-17591.

15. Discher, D. E. and Eisenberg, A. (2002) Polymer Vesicles, *Science 297*, 967-973.

16. Doose, S., Neuweiler, H., and Sauer, M. (2005) A Close Look at Fluorescence Quenching of Organic Dyes by Tryptophan, *Chemphyschem 6*, 2277-2285.

17. Elcock, A. H. (2006) Molecular Simulations of Cotranslational Protein Folding: Fragment Stabilities, Folding Co-Operativity, and Trapping in the Ribosome, *PLoS Comput. Biol 2*, e98.

18. Enderlein, J., Gregor, I., Patra, D., and Fitter, J. (2004) Art and Artefacts of Fluorescence Correlation Spectroscopy, *Curr. Pharm. Biotechnol. 5*, 155-161.

19. Enderlein, J., Gregor, I., Patra, D., Dertinger, T., and Kaupp, U. B. (2005) Performance of Fluorescence Correlation Spectroscopy for Measuring Diffusion and Concentration, *Chemphyschem 6*, 2324-2336.

20. Etchells, S. A. and Hartl, F. U. (2004) The Dynamic Tunnel, *Nat. Struct. Mol. Biol 11*, 391-392.

21. Fedorov, A. N. and Baldwin, T. O. (1997) Cotranslational Protein Folding, *J Biol Chem. 272*, 32715-32718.

22. Fedorov, A. N. and Baldwin, T. O. (1999) Process of Biosynthetic Protein Folding Determines the Rapid Formation of Native Structure, *J Mol. Biol 294*, 579-586.

23. Foeldes-Papp, Z., Demel, U., and Tilz, G. P. (2001) Ultrasensitive Detection and Identification of Fluorescent Molecules by FCS: Impact for Immunobiology, *Proceedings of the National Academy of Sciences 98*, 11509-11514.

24. Foeldes-Papp, Z., Demel, U., and Tilz, G. P. (2002) Detection of Single Molecules: Solution-Phase Single-Molecule Fluorescence Correlation Spectroscopy as an Ultrasensitive, Rapid and Reliable System for Immunological Investigation, *Journal of Immunological Methods 260*, 117-124.

25. Frydman, J., Erdjument-Bromage, H., Tempst, P., and Hartl, F. U. (1999) Co-Translational Domain Folding as the Structural Basis for the Rapid *de-novo* Folding of Firefly Luciferase, *Nat. Struct. Biol 6*, 697-705.

26. Gunnar F.Schröder, Ulrike Alexiev, and Helmut Grubmüller (2005) Simulation of Fluorescence Anisotropy Experiments: Probing Protein Dynamics, *Biophysical Journal 89*, 3757-3770.

27. Haupts, U., Maiti, S., Schwille, P., and Webb, W. W. (1998) Dynamics of Fluorescence Fluctuations in Green Fluorescent Protein Observed by Fluorescence Correlation Spectroscopy, *Proceedings of the National Academy of Sciences 95*, 13573-13578.

28. Heim, R., Cubitt, A. B., and Tsien, R. Y. (1995) Improved Green Fluorescence, *Nature 373*, 663-664.

29. Hiller, S., Wider, G., Imbach, L., and Wuethrich, K. (2008) Interactions with Hydrophobic Clusters in the Urea-Unfolded Membrane Protein OmpX, *Angewandte Chemie International Edition 47*, 977-981.

30. Ikai, A., Fish, W. W., and Tanford, C. (1973) Kinetics of Unfolding and Refolding of Proteins. II. Results for Cytochrome c, *J Mol. Biol 73*, 165-184.

31. Ingo Schwaiger, Mechael Schleiger, Angelika A.Noegel, and Mattias Rief (2011) The Folding Pathway of a Fast-Folding Immunoglobulin Domain Revealed by Single-Molecule Mechanical Experiments, *EMBO J* 6, 46-51.

32. Jäger, M. and Plückthun, A. Domain Interactions in Antibody Fv and scFv Fragments: Effects on Unfolding Kinetics and Equilibria. FEBS letters 462, 307-312. 1999.

33. Jose, B., Steffen, R., Neugebauer, U., Sheridan, E., Marthi, R., Forster, R. J., and Keyes, T. E. (2009) Emission Enhancement within Gold Spherical Nanocavity Arrays, *Phys. Chem. Chem. Phys. 11*, 10923-10933.

34. K.Kinosita, S.Kawato, and A.Ikegami (1977) A Theory of Fluorescence Polarization Decay in Membranes, *Biophysical Journal 20*, 289-305.

35. Kameshwari M.Pappu, Baburaj Kunnumal, and Engin H.Serpersu (1997) A New Metal-Binding Site for Yeast Phosphoglycerate Kinase as Determined by the Use of a Metal-ATP Analog, *Biophys J. 72*, 928-935.

36. Kawahara, K. and Tanford, C. (1966) Viscosity and Density of Aqueous Solutions of Urea and Guanidine Hydrochloride, *Journal of Biological Chemistry 241*, 3228-3232.

37. Kolb, V. A., Makeyev, E. V., and Spirin, A. S. (1994) Folding of Firefly Luciferase During Translation in a Cell-Free System, *EMBO J 13*, 3631-3637.

38. Korlann, Y., Dertinger, T., Michalet, X., Weiss, S., and Enderlein, J. (2008) Measuring Diffusion with Polarization-Modulation Dual-Focus Fluorescence Correlation Spectroscopy, *Opt. Express 16*, 14609-14616.

39. Kramer, G., Ramachandiran, V., and Hardesty, B. (2001) Cotranslational Folding--Omnia mea mecum porto?, *Int. J Biochem Cell Biol 33*, 541-553.

40. Kudlicki, W., Chirgwin, J., Kramer, G., and Hardesty, B. (1995) Folding of an Enzyme into an Active Conformation While Bound as Peptidyl-tRNA to the Ribosome, *Biochemistry 34*, 14284-14287.

41. Kumari, A., Rosenkranz, T., Kayastha, A. M., and Fitter, J. (2010) The Effect of Calcium Binding on the Unfolding Barrier: A Kinetic Study on Homologous Alpha-Amylases, *Biophys. Chem. 151*, 54-60.

42. Loman, A., Dertinger, T., Koberling, F., and Enderlein, J. (2008) Comparison of Optical Saturation Effects in Conventional and Dual-Focus Fluorescence Correlation Spectroscopy, *Chemical Physics Letters 459*, 18-21.

43. Machius, M., Wiegand, G., and Huber, R. (1995) Crystal Structure of Calcium-Depleted Bacillus licheniformis Alpha-Amylase at 2.2 A° resolution, *J. Mol. Biol. 246*, 545-559.

44. Makeyev, E. V., Kolb, V. A., and Spirin, A. S. (1996) Enzymatic Activity of the Ribosome-Bound Nascent Polypeptide, *FEBS Lett. 378*, 166-170.

45. Marme, N., Knemeyer, J. P., Sauer, M., and Wolfrum, J. (2003) Inter- and Intramolecular Fluorescence Quenching of Organic Dyes by Tryptophan, *Bioconjug. Chem. 14*, 1133-1139.

46. Mecke, A., Dittrich, C., and Meier, W. (2006) Biomimetic Membranes Designed from Amphiphilic Block Co-polymers, *Soft Matter 2*, 751-759.

47. Michalet, X., Weiss, S., and Jager, M. (2006) Single-Molecule Fluorescence Studies of Protein Folding and Conformational Dynamics, *Chem. Rev. 106*, 1785-1813.

48. Mueller-Spaeth, S., Soranno, A., Hirschfeld, V., Hofmann, H., Rueegger, S., Reymond, L., Nettels, D., and Schuler, B. (2010) Charge Interactions can Dominate the Dimensions of

Intrinsically Disordered Proteins, *Proceedings of the National Academy of Sciences 107*, 14609-14614.

49. Muller, C. B., Loman, A., Pacheco, V., Koberling, F., Willbold, D., Richtering, W., and Enderlein, J. (2008) Precise Measurement of Diffusion by Multi-Color Dual-Focus Fluorescence Correlation Spectroscopy, *Epl 83*; doi: 10.1209/0295-5075/83/4600

50. Müller, C. B., Eckert, T., Loman, A., Enderlein, J., and Richtering, W. (2009) Dual-Focus Fluorescence Correlation Spectroscopy: a Robust Tool for Studying Molecular Crowding, *Soft Matter 5*, 1358-1366.

51. Neuweiler, H., Johnson, C. M., and Fersht, A. R. (2009) Direct Observation of Ultrafast Folding and Denatured State Dynamics in Single Protein Molecules, *Proc. Natl. Acad. Sci. U. S. A 106*, 18569-18574.

52. Nicolai L.Vekshin (2009) *Fluorescence Spectroscopy of Biommacromolecules* URSS.

53. Noelting, B. (1999) *Protein Folding Kinetics* Springer, Berlin.

54. Okumus, B., Wilson, T. J., Lilley, D. M., and Ha, T. (2004) Vesicle Encapsulation Studies Reveal That Single Molecule Ribozyme Heterogeneities are Intrinsic, *Biophys. J 87*, 2798-2806.

55. Ormo, M., Cubitt, A. B., Kallio, K., Gross, L. A., Tsien, R. Y., and Remington, S. J. (1996) Crystal Structure of the Aequorea Victoria Green Fluorescent Protein, *Science 273*, 1392-1395.

56. Pedelacq, J. D., Cabantous, S., Tran, T., Terwilliger, T. C., and Waldo, G. S. (2006) Engineering and Characterization of a Superfolder Green Fluorescent Protein, *Nat. Biotechnol. 24*, 79-88.

57. Peter Kapusta (2010) Absolute Diffusion Coeffecients: Compilation of Reference Data for FCS Calibration, PicoQuant, *Report*.

58. Reid, B. G. and Flynn, G. C. (1997) Chromophore Formation in Green Fluorescent Protein, *Biochemistry 36*, 6786-6791.

59. Rigler, R., Mets, Widengren, J., and Kask, P. (1993) Fluorescence Correlation Spectroscopy with High Count Rate and Low Background: Analysis of Translational Diffusion, *European Biophysics Journal 22*, 169-175.

60. Rosenkranz, T., Katranidis, A., Atta, D., Gregor, I., Enderlein, J., Grzelakowski, M., Rigler, P., Meier, W., and Fitter, J. (2009) Observing Proteins as Single Molecules Encapsulated in Surface-Tethered Polymeric Nanocontainers, *Chembiochem 10*, 702-709.

61. Rosenkranz, T., Schlesinger, R., Gabba, M., and Fitter, J. (2011) Native and Unfolded States of Phosphoglycerate Kinase Studied by Single-Molecule FRET, *Chemphyschem 12*, 704-711.

62. Ruttinger, S., Buschmann, V., Kramer, B., Erdmann, R., Macdonald, R., and Koberling, F. (2008) Comparison and Accuracy of Methods to Determine the Confocal Volume for Quantitative Fluorescence Correlation Spectroscopy, *Journal of Microscopy-Oxford 232*, 343-352.

63. Schwille, P. (2001) Fluorescence Correlation Spectroscopy and its Potential for Intracellular Applications, *Cell Biochemistry and Biophysics 34*, 383-408.

64. Strucksberg, K. H., Rosenkranz, T., and Fitter, J. (2007) Reversible and Irreversible Unfolding of Multi-Domain Proteins, *Biochim. Biophys. Acta 1774*, 1591-1603.

65. Thomas Dertinger, Benjamin Ewers, Benedikt Krümer, Felix Koberling, Iris v.d.Hocht, and Jörg Enderlein. Two-Focus Fluorescence Correlation Spectroscopy. PicoQuant GmbH , 1-7. 2007.

66. Tsien, R. Y. (1998) The Green Fluorescent Protein, *Annu. Rev. Biochem. 67*, 509-544.

67. Uemura, S., Iizuka, R., Ueno, T., Shimizu, Y., Taguchi, H., Ueda, T., Puglisi, J. D., and Funatsu, T. (2008) Single-Molecule Imaging of Full Protein Synthesis by Immobilized Ribosomes, *Nucleic Acids Res. 36*, e70.

68. Ugrinov, K. G. and Clark, P. L. (2010) Cotranslational Folding Increases GFP Folding Yield, *Biophysical Journal 98*, 1312-1320.

69. Volker Buschmann, Benedikt Krümer , Felix Koberling, Rainer Macdonald, and Steffen Rüttinger (2007) Quantitative FCS:Determination of the Confocal Volumeby FCS and Bead Scanning with the MicroTime 200, *http://photon-counting. com*.

70. Watson, H. C., Walker, N. P., Shaw, P. J., Bryant, T. N., Wendell, P. L., Fothergill, L. A., Perkins, R. E., Conroy, S. C., Dobson, M. J., Tuite, M. F., Kingsman, A. J., and Kingsman, S. M. (1982) Sequence and Structure of Yeast Phosphoglycerate Kinase, *EMBO J. 1*, 1635-1640.

71. Weiss, S. (1999) Fluorescence Spectroscopy of Single Biomolecules, *Science 283*, 1676-1683.

72. Wilhelm Burger and Mark J.Burge (2008) in *Digital Image Processing, an Algorithmeic Introduction using Java* (Wilhelm Burger and Mark J.Burge, Eds.) pp 343-366, Springer, New York.

73. Yu, J., Xiao, J., Ren, X., Lao, K., and Xie, X. S. (2006) Probing Gene Expression in Live Cells, One Protein Molecule at a Time, *Science 311*, 1600-1603.

74. Zhao, M., Jin, L., Chen, B., Ding, Y., Ma, H., and Chen, D. (2003) Afterpulsing and Its Correction in Fluorescence Correlation Spectroscopy Experiments, *Appl. Opt. 42*, 4031-4036.

75. Zimmer, M. (2002) Green Fluorescent Protein (GFP): Applications, Structure, and Related Photophysical Behavior, *Chem. Rev. 102*, 759-781.

4-Conclusion and outlook

Setting up the microscopes for single molecule measurements

Although simultaneous dual color imaging in the wide field microscope gave reasonable and reproducible results the handling was often difficult and time-consuming and the results left some space for improvements. After some experience with our set up I would introduce in future essentially two improvements. First I am planning to replace the wedged filters by a more straight forward approach which employs a combination of two angled mirrors, a conventional dichroic mirror, and two conventional emission filters. Such a setup is described in the literature (*7*) and a scheme is shown in Fig. 4.1.

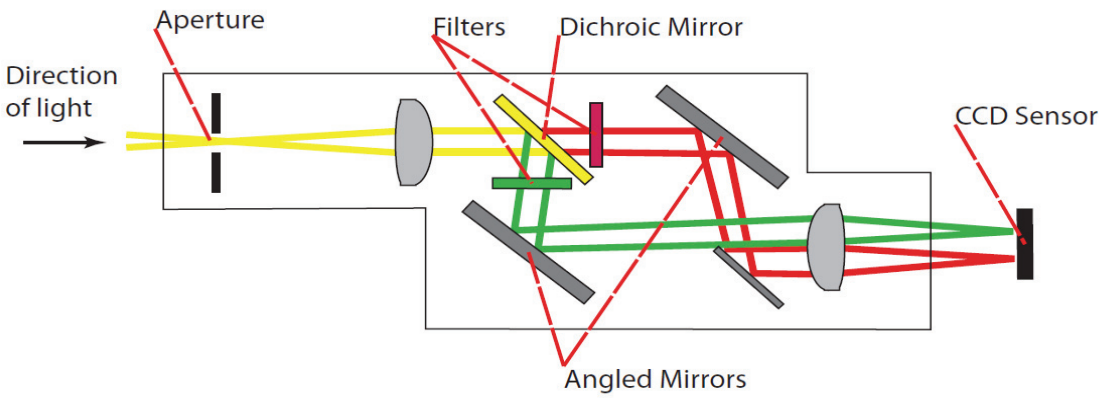

Figure 4-1: A schematic draw of the image spitting device as integrated in a Optosplit II device produced by Cairn Research Ltd., United Kingdom, taken from (3).

The advantages of this system with respect to the wedged filters is manifold. First, conventional optical elements used in this system are available at much lower costs as compared to custom made wedged filters (in particular if many different color combinations are required). Second the obtained images can be adjusted perfectly to the same size for both color channels which avoids later resizing and rescaling of the image channels. And last but not least a change from one color combination to another one is must faster and straightforward because not alignment steps are required since only the respective filters have to be exchanged (see Fig. 4-1).

The second important issue is related to the moderate signal to noise ratio which can be achieved with our conventional wide-field setup. Therefore in recent years more and

more fluorescence microscopes made use of total internal reflection fluorescence (TIRF). Although in our samples we are not dealing with background fluorescence from distances well apart from the surface (we use only surface tethered fluorescent biomolecules) which is classically suppressed in TIRF microscopy, we can also benefit from a much better signal to noise ratio using TIRF (for more details see (*2*)). TIRF microscopes can be realized in two different illumination modes (*6,10*): 1) Illumination using a prism, in this case we have illumination from the top like in transmission mode. 2) Illumination using the microscope objective itself, this is typically the epi-illumination method and will be the method of choice for our purpose. A schematic draw of an "off-axis" excitation using the objective based approach is shown in Figure 4-2.

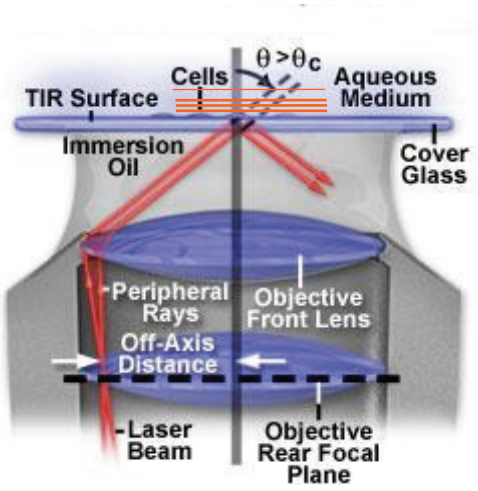

Figure 4-2: A TIRFM objective. When the excitation beam (red line) is hitting the surface with an angle larger than the critical angle the beam will be totally reflected without any transmission, and an evanescent wave (orange lines) is built up on the top of the reflecting surface.

Using this illumination mode we obtain very efficient excitation conditions caused by an evanescent wave which results finally in a much better putative signal to noise ratio for peaks from single surface immobilized fluorphores. In order to achieve TIRF illumination we have to use an objective with a sufficient larger N.A. (typically > 1.45) and the ability to move the beam along an axis perpendicular to the optical axis, in order

to switch between on-axis (classical wide-field imaging) and off-axis (TIRF illumination) excitation beams.

Monitoring protein synthesis and protein folding

In order to reach our final goal, namely the time-resolved analysis of co-translational folding of polypeptide chains, I performed valuable first steps in establishing an *in vitro* protein synthesis system, suitable for single molecule detection. The protein synthesis apparatus (the ribosomes) could be tethered to the surface by maintaining its functionality and the detection of individual ribosomes producing individual GFPs remaining attached to the ribosomes was possible. Even the direct incorporation of fluorescent dyes into a newly synthesized polypeptide chain was shown to be possible with our approach. However, to reach our final goal at least two major improvements and developments are required for further progress. (1) In most of our images we still have to fight for a reasonable high density of tethered ribosomes which in addition should also be active (in synthesizing polypeptide chains) to an extend as high as possible. To reach these conditions we first have to improve the surface blocking with PEG (to reduce unspecific binding to the surface) by improving our protocols (more stable chemical compounds, more elaborated silanization protocols). Progress in this respect would allow us to monitor a few hundred tethered well separated molecules in an area of about 80 x 80 μm^2 at the same time. In the presented results we typically reached only densities which were by a factor of ten lower. But a rather high density is essential, because under conditions we used only 10% of the tethered ribosome start to synthesize proteins. (2) With respect to the dye incorporation we obtained until today only rather qualitative results. In order to employ dye incorporation for FRET studies we need not only site-specifically labeled ribosomes (which is essentially the work of our molecular biologists) but also a reasonable high probability of correct dye incorporation. Therefore, in further studies we first have to prove unequivocally that the dyes are predominantly incorporated into the polypeptide chain (and not unspecifically attached to the surface of ribosomes, which until today we cannot rule out to 100 %). Only after these checks we can really start to monitor

fluorescence intensity changes in both color channels, in order to obtained information about distance changes according to FRET theory.

Observing proteins as single molecules encapsulated in surface-tethered polymeric nanocontainer

In this project we succeeded in encapsulating individual proteins into polymeric vesicles (polymerosmes), which were tethered to the surface. This approach enabled us to monitor single molecules for extended observation times (typically not possible with freely diffusing molecules). A further significant advantage of the employed vesicles is due to the fact that they are permeable to GndHCl, which allows for *in-situ* buffer exchange to switch between folding and unfolding conditions. Although we could somehow follow folding/unfolding transitions of encapsulated PGK (from analyzing fluorescence intensity changes caused by PET), we were not really able to obtain details about the proteins structure at different folding states. In order to reach this goal the use of FRET would be the method of choice. Recently a PGK mutant labeled with a FRET pair was established in our group (*11*), which can be used for studies with polymerosomes. To proceed with our studies we first have to repeat the same cross-checks for this double labeled PGK as I did already for our PET sample. The challenge of FRET with immobilized proteins (in our case due to the encapsulation within surface tethered nanocontainers) is to watch one and the same protein during multiple unfolding and refolding transitions. Such studies on single molecule level are expected to reveal valuable insights about folding pathways in particular for multi-domain proteins, typically characterized by a more complex energy landscape, which presumably exhibit several detectable intermediate states.

Native and unfolded states of multidomain proteins studied by FCS

In this project we have studied the structure of several multi-domain proteins (in addition to PGK we studied also the α-amylases BLA and TAKA) as a function of the chemical denaturant GndHCl. For this purpose we employed FCS to obtain information about the structural expansion of freely diffusing proteins by analyzing the auto-correlation of the observed fluorescence intensity fluctuations. In the time regime of

milliseconds we observed translational diffusion which was used to determine the hydrodynamic radii of the diffusing proteins. In addition for PGK I was able to detect a fast process (~100 ns) which was clearly related to a fluorescence quenching caused by PET. While characterizing the overall size of proteins by hydrodynamic radii obtained from FCS is already well established, the approach of using PET to measure structural parameters of proteins is rather new and methodical developments are currently performed by several groups (*5,9,12*). Complementary to FRET (which is sensitive for structural distances between 3 and 6 nm) PET is able to measure much smaller distances (typically $\leq$ 1 nm) between structural elements within proteins because the process requires van der Vaals contacts between the dye and the quencher. According to this, steady state intensities as well as PET rates can be employed to derive distances and distance changes, if a calibration was made in advance. However studies with GndHCl as a chemical denaturant are intrinsically difficult because the life time of the counter-complex (non-fluorescent dye-quencher complex) is directly depending on the GndHCl concentration (*4*), which makes interpretation of the PET rates in terms of structural distances not straightforward. Therefore alternative approaches to achieve unfolded states would be the most promising approach to continue my studies. In this respect using Urea (*1,8*) or extreme pH-values to induce unfolding should be considered for further PET studies. However, even for these approaches the effect of these denaturating conditions on counter-complex life times have to be analyzed.

References

1. Andrade, S. M. and Costa, S. M. B. (2011) Tetrakis (4-Sulfonatophenyl) Porphyrin Fluorescence as Reporter of Human Serum Albumin Structural Changes Induced by Guanidine Hydrochloride, *Journal of Photochemistry and Photobiology A: Chemistry 217*, 125-135.

2. Axelrod, D. (2001) Total Internal Reflection Fluorescence Microscopy in Cell Biology, *Traffic 2*, 764-774.

3. Catalog (2010) Optosplit II Instruction Manual, *Cairn Research Ltd*.

4. Doose, S., Neuweiler, H., and Sauer, M. (2005) A Close Look at Fluorescence Quenching of Organic Dyes by Tryptophan, *Chemphyschem 6*, 2277-2285.

5. Doose, S., Neuweiler, H., and Sauer, M. (2009) Fluorescence Quenching by Photoinduced Electron Transfer: A Reporter for Conformational Dynamics of Macromolecules, *Chemphyschem 10*, 1389-1398.

6. Herbert, S. (2005) Total Internal Reflection Fluorescence Microscopy: Technical Innovations and Novel Applications, *Current Opinion in Biotechnology 16*, 13-18.

7. Kinosita, K., Itoh, H., Ishiwata, S., Hirano, K., Nishizaka, T., and Hayakawa, T. (1991) Dual-View Microscopy with a Single Camera: Real-Time Imaging of Molecular Orientations and Calcium, *The Journal of Cell Biology 115*, 67-73.

8. Leggio, C., Galantini, L., Konarev, P. V., and Pavel, N. V. (2009) Urea-Induced Denaturation Process on Defatted Human Serum Albumin and in the Presence of Palmitic Acid, *J. Phys. Chem. B 113*, 12590-12602.

9. Neuweiler, H., Doose, S., and Sauer, M. (2005) A microscopic view of miniprotein folding: enhanced folding efficiency through formation of an intermediate, *Proc. Natl. Acad. Sci. U. S. A 102*, 16650-16655.

10. Reck-Peterson, S. L., Derr, N. D., and Stuurman, N. (2010) Imaging Single Molecules Using Total Internal Reflection Fluorescence Microscopy (TIRFM), *Cold Spring Harbor Protocols 2010*, doi: 10.110//pdp.top73

11. Tobias Rosenkranz (2011) Time-Resolved Single Molecule FRET Studies on Folding/Unfolding Transitions and on Functional Conformational Changes of Phosphoglycerate Kinase, *Thesis/ Dissertion* 101-104.

12. Vaiana, A. C., Neuweiler, H., Schulz, A., Wolfrum, J., Sauer, M., and Smith, J. C. (2003) Fluorescence Quenching of Dyes by Tryptophan:Interactions at Atomic Detail from Combination of Experiment and Computer Simulation, *Journal of the American Chemical Society 125*, 14564-14572.

5-Summary

In my thesis I aimed to study protein folding/unfolding transitions and protein synthesis using single molecule fluorescence techniques. For this purpose I employed confocal and wide-field fluorescence microscopes. For surface immobilized biomolecules I set up and calibrated an autofocus wide-field system for time-resolved simultaneous dual color imaging. In the case of freely diffusing proteins a confocal microscope with pulsed excitation was used for time-resolved anisotropy measurements and for fluorescence correlation spectroscopy (FCS). In the first project the synthesis of the green fluorescence protein (GFP) has been monitored while the protein was tethered to surface immobilized functional ribosomes. In time resolved studies we obtained characteristic maturation times of our GFP mutant which was rather fast (5 min) compared to most other GFP mutants. In further studies we aimed to analyze the folding process in more detail by incorporating fluorescent dyes (BODIPY-TMR) into the polypeptide chain using a cell-free transcription/translation system. First results were obtained which prove a partial integration of the dye into chain and gave valuable findings how to continue in order to establish a Förster resonance energy transfer (FRET) pair for folding studies. In the second part of this work we performed protein folding studies on single molecule level with phosphoglycerate kinase (PGK) encapsulated in polymeric vesicles as nano-containers. Some of the most interesting properties of polymeric vesicles are their remarkable stability against harsh environmental conditions and their permeability for chemical denaturants. We demonstrated in an application on protein folding, that surface-tethered polymerosomes are suitable to perform time-resolved single molecules studies with encapsulated proteins. A third project dealt with a structural and dynamical characterization of protein structures by employing FCS in order to obtain hydrodynamic radii of the protein. We studied a few multi-domain proteins under different concentration of a chemical denaturant (guanidine hydrochloride, GndHCl) and observed at low denaturant concentrations (≤ 1 M GndHCl) a slight compaction of the protein structures which was followed by a drastic expansion of the proteins in the unfolded state. For PGK we were also able to resolve structural parameters of the protein by analyzing a characteristic fast process which was caused by photo induced electron transfer (PET).

Zusammenfassung

In der vorliegenden Arbeit wurde das Ziel verfolgt, Protein Faltungs- und Entfaltungsübergänge mit einzelmolekülfluoreszenz-spektroskopischen Techniken zu studieren. Zu diesem Zweck habe ich konfokale und Weitfeld-Mikroskope eingesetzt. Zur Beobachtung von oberflächenimmobilisierten Biomolekülen habe ich ein Mikroskop-System mit Autofokusoption für zeitaufgelöste simultane zweifarben Bildaufnahme etabliert und kalibriert. Im Falle frei diffundierender Proteine wurde ein Konfokal-Mikroskop mit gepulster Anregung für zeitaufgelöste Anisotropieabfälle und für fluoreszenzkorrelationsspektroskopische (FCS) Messungen verwendet. Im ersten Projekt wurde die Synthese eines grünfluoreszierenden Proteins (GFP) verfolgt, während das GFP an einem immobilisierten funktionsfähigen Ribosom gebunden war. In zeitaufgelösten Studien wurde die charakteristische „Reifezeit“ unserer GFP-Mutante bestimmt, die mit etwa 5 Minuten deutlich kleiner war als die der meisten anderen GFP Mutanten. In weiteren Studien war es unser Ziel den Faltungsprozess detaillierter zu untersuchen, indem wir einen Fluorezenzfarbstoff direkt in die Polypeptidkette eingebaut haben. Erste Ergebnisse zeigten einen teilweisen Einbau des Farbstoffs in die Kette, welches eine vielversprechende Ausgangssituation für weitere Försterresonanz Energie-transfer (FRET) Faltungsstudien darstellt. In einem zweiten Projekt der Arbeit wurden Einzelmolekül-Proteinfaltungsstudien mit der Phosphoglycerat-Kinase (PGK) durch-geführte, wobei individuelle Proteine in Polymervesikel eingeschlossen wurden. Einige der wichtigsten Eigenschaften dieser Vesikel war deren bemerkenswerte Stabilität gegen raue Umgebungsbedingungen und deren Durchlässigkeit für chemische Denaturantien. Wir konnten in einer Anwendung zur Proteinfaltung zeigen, dass oberflächenimmobilisierte Polymervesikel geeignet sind, zeitaufgelöste Einzelmolekülstudien mit eingeschlossenen Proteinen durchzuführen. Ein drittes Projekt beschäftigte sich mit der Charakterisierung struktureller und dynamischer Proteineigenschaften, bei dem FCS Messungen zur Bestimmung hydrodynamischer Radien genutzt wurden. Hierbei haben wir einige Multidomänen Proteine bei verschiedenen Konzentrationen von Guanidinhydrochlorid (GndHCl; chemisches Denaturant) untersucht und fanden bei niedrigen Konzentrationen ($\leq$ 1 M GndHCl) ein leichte Kompaktierung der Proteine, während der voll entfaltete Zustand eine expandierte Struktur aufwies. Im Falle der PGK konnten wir darüber hinaus einen schnellen Prozess in der Autokorrelation nachweisen, der direkt mit einem photo-induzierten Elektrontransfer (PET) zusammenhängt.

Erklärung

Ich erkläre, dass ich die vorliegende Arbeit selbständig und ohne unerlaubte Hilfe verfasst habe. Die vorliegende Arbeit wurde weder in der jetzigen oder in ähnlicher Form bei einer anderen Institution eingereicht. Es wurden zuvor keinerlei Promotionsversuche unternommen.

Jülich, ...
Diaa Eldin Atta

Teile dieser Arbeit wurden zur Veröffentlichung eingereicht und angenommen.

Katranidis, A.; Atta, D.; Schlesinger, R.; Nierhaus, K. H.; Choli-Papadopoulou, T.; Gregor, I.; Gerrits, M.; Büldt, G.; Fitter, J., Fast Biosynthesis of GFP Molecules: A Single-Molecule Fluorescence Study, *Angew. Chem. Int. Ed Engl.* 48:1758-1761; 2009.

Rosenkranz, T.; Katranidis, A.; Atta, D.; Gregor, I.; Enderlein, J.; Grzelakowski, M.; Rigler, P.; Meier, W.; Fitter, J., Observing Proteins as Single Molecules Encapsulated in Surface-Tethered Polymeric Nanocontainers, *Chembiochem* 10:702-709; 2009.

Fitter, J.; Katranidis, A.; Rosenkranz, T.; Atta, D.; Schlesinger, R.; Büldt, G., Single molecule fluorescence spectroscopy: a tool for protein studies approaching cellular environmental conditions, *Soft Matter*, 7, 1254-1259, 2011.

Life is full of stones
do not stumble, but
collect it and make it a
ladder, climb it to the
success.
Dina Attia

Acknowledgment

I want express my deep thanks to the German government and the Research Centre Juelich, for the support and the Egyptian government represented by the Cultural Affairs and Missions Sector for the financial support.

It is not enough to say thank you for your father, this is my feeling towards **Prof. Dr. Georg Büldt**. It is really loss that he will leave the institute, his fruitful discussions and father behavior is very important in the scientific field. I thank him also because he allows me to perform my PhD work in his institute.

I am heartily thankful to my supervisor, **Dr. Jörg Fitter**, whose encouragement, guidance and support from the initial to the final level enabled me to develop an understanding of the subject.

I want to thank **Prof. Dr. Jan K.G.Dohnt** for his kind review of my thesis.

It is very important for me to thanks a lot **Dr. Ingo Gregor** for his valuable support in setting up some the wide-field microscope from the first glance, and his kindly and friendly co-operation.

I also want to thank my colleagues:

Alexandros Katranidis, for his support in the chemical and biochemical preparations.

Tobias Rosenkranz, for his help in the protein labeling and the fruitful discussions, also the kindly support in the administrative difficulties.

I could not forget the nice discussions and the support I got from the others like Prof. Dr. Valentin Gordliy, Dr. Jana Kriegsmann, Dr. Renu Batra-Safferling, Dr. Ramona Schlesinger, Dr. Tomas Gensch, and Matteo Gabba.

I also must thank my institute colleagues Axel Baumann, Andrii Ishchenko, Alex Volkov, Darya Kempe, Uday Kumar, Anna Cousin, Christian Baeken, Maria Simakova, Paraskevas Lamprou, and from ICS-6 Pallavi Thiagarajan, Amina Aladag, for the kind atmosphere. In addition I want to thank Yanbin Ma, for the nice time and discussions in the lunch time.

If this work and other work get a chance to be done this does not mean that it is only the researchers who did it, but there are other important people and co-workers which gave me the opportunity to do my work. So I want to thank:

Mr. Sascha Lehman, for his support with computers and software and for his help in those things which must be done in the workshop.

Mrs. Birgit Gehrman for her administrative work and her administrative support, she really makes the complicated bureaucratic things inside the research center very easy. Also Mrs. Roswitha Bley, she has done the same thing in the outer administrations, which is very complicated for the foreigners like me.

The technician team, Mrs. Ritter Illona, Mrs. Ramona Justinger, and Mrs. Nicole Müller for their laboratory support.

Furthermore I would like to acknowledge the support by Prof. W. Meier (University of Basel) for providing us polymers for the vesicle preparation and by Dr. M. Gerrits (RiNA GmbH, Berlin) for substantial contributions to the ribosome project.

I am sorry my dear reader for the long acknowledgement but really I am a lucky man who met a lot of persons which really supported me, and had a very strong impact on my scientific life.

For example

Prof. Dr. Muhamed Elmorsy, Prof. Dr. Mamoud Elkashan and **Prof. Dr. Samir Ushah Elkhamisy**, and **Prof. Dr. Medhat Ibrahim**. Also I want to thank my teachers in the school who built my knowledge bases like **Mr. Muhamed Elashry, Mr.Mohamed Farid, Mr. Milad Hanna, Mr. Gaudat Abd Elmaseeh, Mr. Mohamed Abd Elarahman, Mr. Zahier Saleh** and **Mr. Mohamed Kamal**.

Forgive me dear reader, but I could not finish this acknowledgment with out thank a lot from my deep heart my great father and the real angel my mother which with her support from the birth till now I could not do any thing. Finally I want to thank my sweetheart paramour **Rasha Ibrahim**, my wife for her past and coming patience and moral support.

Lastly, I offer my regards and blessings to all of those who supported me in any respect during the completion of this thesis.

aus dem Institut für komplexe Systeme 5
des Forschungszentrums Jülich

Gedruckt mit der Genehmigung der
Mathematisch-Naturwissenschaftlichen Fakultät der
Heinrich-Heine Universität Düsseldorf

Referent:
Koreferent:

Tag der mündlichen Prüfung: